DATA-DRIVEN DESIGN OF A METAMATERIAL UNIT CELL USING SPARSE GAUSSIAN PROCESSES

DELFT UNIVERSITY OF TECHNOLOGY

DATA-DRIVEN DESIGN OF A METAMATERIAL UNIT CELL USING SPARSE GAUSSIAN PROCESSES

by
Piotr Stanislaw GLOWACKI

Thesis

submitted in partial fulfilment of the requirements for the degree of

Master of Science

in the department of

Materials Science and Engineering

at the Faculty of Mechanical, Maritime and Materials Engineering
of Delft University of Technology
to be defended publicly on Friday 22 March 2019 at 13:00.

Thesis Supervisor,	
Dr. M.A. Bessa,	Faculty 3mE, TU Delft
Committee members:	
Dr. P. Dey,	Faculty 3mE, TU Delft
Dr. V. Popovich,	Faculty 3mE, TU Delft
Dr. M. Sluiter,	Faculty 3mE, TU Delft

Student number: 4618602
Date: March 12, 2019

ABSTRACT

Metamaterials are a new class of materials where the properties crucially depend on the design of the unit cell that is periodically repeated in space. In this study a new metamaterial unit cell concept has been proposed, inspired by a class of space structures known as deployable masts. The ability of these structures to contract to a fraction of their size made them suitable candidates for energy absorbing applications. One of the main design targets of energy absorbers is the ability to tune the material response to specific applications. Tunability of the mechanical response of the metamaterial concept requires deep understanding of the influence of design parameters. The prime focus of this study was to gain this understanding via data-driven insights.

Conventionally, the design of a new material is carried out by making educated guesses about the design parameters and subsequently performing expensive and time-consuming experiments. In this work computational simulations were utilized to create databases of mechanical responses. These databases are later used to model the relationship between the inputs and the output response. This generated the issue of how and what method to use to effectively determine this relationship. This work explored state-of-the-art machine learning methods to enhance a recently proposed data-driven framework with the goal of designing a new super-compressible metamaterial with large energy absorption. Importantly, the data-driven design process included the influence of manufacturing imperfections on the mechanical response of the metamaterial.

The study revealed that by tuning the design parameters, significantly different mechanical response of the structure was achievable. The proposed learning model has enabled mapping of the influence of design parameters in the design space, moreover the sensitivity to those parameters varied across the design space. The increased energy absorption has been attributed to the resistance to bending of the main load carrying components of the design. It was demonstrated that the number of those components and the elastic modulus were scaling factors for the quantities of interest. Based on the insights gained, a unit cell metamaterial design with significantly improved energy absorbing capability was proposed.

ACKNOWLEDGEMENTS

This thesis concludes my time as student at the Delft University of technology where I spent two and a half years fulfilling the requirements for my degree in Materials Science and Engineering. After one busy year, my thesis is ultimately complete, and I would like to express my gratitude to those without whom it would not be possible.

Firstly, I cannot thank enough my supervisor, Miguel Bessa. Without your guidance, immeasurable assistance at every step of the way and simply human friendship, this milestone in my career would not be possible. I cannot be grateful enough for taking under your wings a guy without any prior computational expertise, believing in him and reshaping his mindset and competencies. *Muito obrigado!*

I would also like to thank Marcel Sluiter for our conversations and triggering me to face my weakness and eventually embrace the world of Computational Material Science. Without it, I would have chosen a different thesis topic and a different career path. An enormous amount of gratitude goes to my parents, Piotr and Marta, who were always there for me when I needed them the most. Your undying support has allowed me to experience my studies in the most comfortable way throughout this adventure. Lastly, I would like to thank my friends and everyone else who had to bear my presence, during this time.

PREFACE

The way science has given us new discoveries has in principle not changed over centuries. Innovators create scientific breakthroughs based on years of experience within a given field, intelligence, intuition and often, luck. This process is often time and resource consuming, yet it is the main path towards scientific revelations. In some cases, after years of such tried and tested trial-and-error approach, the results are somewhat disappointing. However, in recent years data-driven approaches have opened avenues for new discoveries. Moreover, rapid advancement of these new tools makes ideas once unthinkable, possible. For example, in materials sciences, the advent of high precision and flexible additive manufacturing technologies along with ever increasing use of computational analysis methods creates new pathways for cutting-edge research. The former makes long standing dogmas refutable while the latter allows for relatively rapid and cost-efficient verification of new ideas. Moreover, the recent outburst of artificial intelligence techniques makes the computational approach even more effective as models that were once too complicated are now within grasp. This work is merely a trivial example of how this new approach to discovery of novel materials can be utilised. It is my sincere hope that this work may serve as an inspiration for other researchers to achieve feats far greater than obtaining a Master's degree diploma.

Piotr Stanislaw Glowacki
Delft, March 2019

CONTENTS

Abstract v

Acknowledgements vii

Preface ix

1 Introduction 1

2 Literature review 3
- 2.1 Inspiration from space structures: the deployable mast 3
  - 2.1.1 The Coilable Mast 6
  - 2.1.2 Local Coil Mode 8
- 2.2 Metamaterials. 9
  - 2.2.1 Instability-based metamaterials 10
  - 2.2.2 Bistable Snapping metamaterials 13
- 2.3 Energy Absorbers 17
- 2.4 Machine Learning. 26
  - 2.4.1 Gaussian Process Regression. 30
  - 2.4.2 Sparse Gaussian Process Regression 35
  - 2.4.3 Sparse Prior Approximations. 37
  - 2.4.4 Sparse Posterior Approximations 39

3 Data-driven framework 41
- 3.1 Proposed metamaterial concept 41
- 3.2 Design of Experiments 42
  - 3.2.1 Constant variables 43
  - 3.2.2 Continuous variables 44
- 3.3 Finite element analysis 45
  - 3.3.1 Geometric imperfections for RIKS analysis. 46
  - 3.3.2 Post-buckling analysis with arc-length method 51
- 3.4 Bayesian machine learning 53

4 Metamaterial analysis with data-driven framework 57
- 4.1 Best designs from the design of experiments 58
- 4.2 Design charts as contour plots 60
- 4.3 Sensitivity Analysis 64
- 4.4 Metamaterial tunability 67

5 Discussion 73
- 5.1 Data-driven framework 73
- 5.2 The influence of design parameters. 74
  - 5.2.1 Area of the longeron Cross Section 74

5.2.2 Ratio of Shear and Elastic Moduli 75
5.2.3 Second moment of area around X-axis 75
5.2.4 Second moment of area around Y-axis 76
5.2.5 Torsion constant 76
5.2.6 Height of the unit Cell 76
5.2.7 Ratio of Ring Diameters 77
5.2.8 Realistic cross-section 77

6 Conclusion and Recommendations 81
6.1 Conclusions. 81
6.2 Recommendations 82

References 83

A Estimation of Uncertainty for the quantities of interest 93

B Comparative investigation of Sparse Gaussian Processes 99
B.1 Regression 99
B.2 Classification 104

C Supplementary contour plots for machine learning 109

1

INTRODUCTION

THIS thesis contributes to the design of a new energy absorbing material by using machine learning to study the influence of the unit cell parameters on buckling and post-buckling of the structure. On the path to achieve this, we quantify the uncertainty of post-buckling response and compare the performance of recent sparse Gaussian processes – new Bayesian machine learning methods that are found herein to be well suited for mechanical metamaterial design.

The traditional approach to design new materials is based on finding (often) simple relationships between the mechanical properties of a given material and the chemical composition as well as microstructure morphology. However, along with rapid advancement of additive manufacturing, alternative possibilities have emerged for the design of novel materials. With high precision additive manufacturing, it is conceivable to design structures with purposely defined spatial orientation, like buildings but on several orders of magnitude smaller scale. The properties of these materials mostly depend on the architecture of the unit cell that is periodically repeated in space, rather than their chemical composition. These materials are broadly referred to as metamaterials.

Energy absorption is an important property that finds use in many engineering applications fields such as military, aerospace, automotive, and civil, to name just a few. A wealth of energy absorbing materials already exists. Yet increasing energy absorption of a material requires the improvement of two key competing properties: strength and deformation. Moreover, the exact requirements of materials in general, and energy absorbers in particular, depend on the structural applications where they are used. For example, in automotive crashworthiness, the optimal material may not necessarily be ultra-strong and highly deformable, since an impact on such a material could lead to high forces transferred onto the passengers upon impact. Thus, the target in materials design can be not only the optimization of contrasting properties, but also the ability to tune the material response to specific applications. In the case of periodic metamaterials, due to their design freedom, the geometry of their unit cell plays a critical role in their mechanical response. In this project, inspiration for the unit cell has been taken from a class of space structures referred to as the deployable mast. These structures are lightweight, able to resist significant loads and may be retracted to a fraction of their size in comparison to when they are employed. If the concept can be miniaturized, i.e. if it is scalable, then it could offer an ideal setting for data-driven design of this unit cell in order to optimize both strength and deformability to achieve unprecedented energy absorption via super-compressibility.

Despite the apparent simplicity of the unit cell, it would be significantly time-consuming to design it and optimize its response for such a demanding application by using a purely trial-and-error approach driven by experiments. Therefore, in this work, computational simulations using the finite element method have been employed to generate tens of thousands of different designs that were later investigated by artificial intelligence methods, to derive data-driven insights about the influence of the unit cell design parameters on the mechanical response of the metamaterial.

This thesis is organized as follows. Chapter 2 contains the literature review on prior work on buckling metamaterials, energy absorbing materials, the deployable mast structure and sparse gaussian processes. All the necessary information regarding the methods used to conduct this study can be found in Chapter 3, while the main results are presented in Chapter 4. An in-depth discussion of the aforementioned results is provided in Chapter 5. Conclusions and recommendations for future work concerning the design of the metamaterial unit cell are included in Chapter 6.

2

LITERATURE REVIEW

DATA-DRIVEN research requires to articulate knowledge from multiple fields. This literature review chapter begins with Section 2.1 describing the aerospace structure that served as inspiration for the data-driven design of a new metamaterial. Section 2.2 provides a broad overview of current state-of-art of metamaterials. The topic of energy absorbing materials and structures is presented in Section 2.3. Finally, selected topics in machine learning and gaussian process algorithms are briefly discussed in Section 2.4.

2.1. INSPIRATION FROM SPACE STRUCTURES: THE DEPLOYABLE MAST

Space structures have strict design requirements due to the limits imposed on cargo dimensions by current launchers, despite the ever-increasing efforts and considerable reduction in the cost per kilo of cargo sent into space. This constraint is problematic, as it sets a theoretical limit on the capability and configuration of apparatus we send into space, in particular the focal lengths and aperture diameters of telescopes [1]. The primary requirements of the deployable space structure are deployability, compactability and structural acceptability [2]. Many deployable concepts have already been created and investigated, and some have been used in aerospace missions. Deployable masts (booms) are notable solutions frequently used as critical structural components in satellites [2, 3].

Deployable masts are a class of structures that can be stowed into a small volume and expanded into long, slender, and stable booms: they can typically be packed to under 5% of their deployed length [5]. Masts are compacted in the launch vehicle and may be deployed in a sequential or synchronous way, by expanding promptly or gradually [2], when the satellite goes into orbit [6]. Deployable masts have the potential to offer an

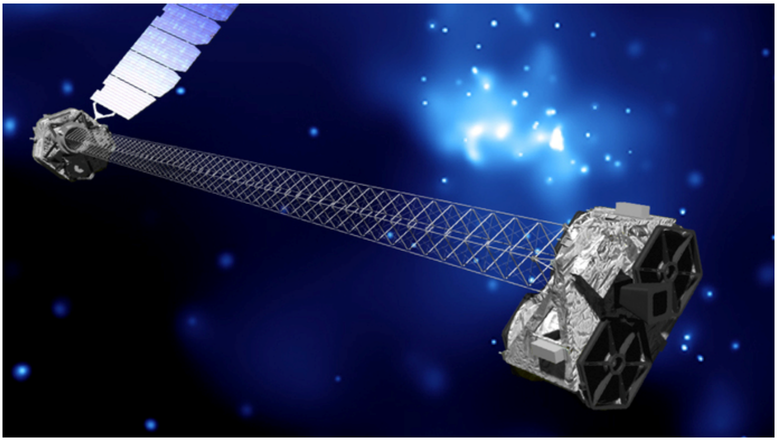

Figure 2.1: An example of a deployable structure [4].

ideal solution for telescopes of large apertures (>10 m diameter) and medium baselines (from 15 to 50 m) [1]. Consequently, the payload capability is not limited by dimensions of the launcher's fairing, but rather by the usable volume.

Apart from telescopes, applications of deployable mast are various and include, magnetic sensor's masts for scientific satellite, long range navigation antennas masts, telecommunication antennas, and energy absorbing structures [7–10]. provides a qualitative summary of the different types of deployable masts. As can be inferred from the table, there is a trade-off between obtaining a light and compact mast or a high precision and strong mast but with higher weight. One of the design concepts, the coilable mast, is particularly interesting because it seems to find a balance between the relevant properties, i.e. achieving good deploying accuracy and post deployment stability, significant flexibility in terms of dimensions, and reasonable load bearing capability

Table 2.1: Relative comparison of deployable mast technologies [1, 5, 10].

	Type of Deployable Mast					
Property	Inflatable	Telescopic	SMC	Articulate	Truss	Coilable
Mass	GOOD	BAD	GOOD	BAD	BAD	GOOD
Load Capacity	BAD	GOOD	BAD	GOOD	GOOD	MEDIUM
Accuracy	BAD	GOOD	BAD	GOOD	GOOD	MEDIUM
Stability	BAD	GOOD	BAD	GOOD	GOOD	MEDIUM
Packaging Ratio	GOOD	BAD	MEDIUM	BAD	MEDIUM	GOOD

Figure 2.2 shows approximate comparisons between the different designs, where truss and telescopic structures are characterized by a sharp increase in boom diameter with increasing length of the mast, while the coilable mast is believed to be the one that can span larger deployable lengths from 1 to 100 m.

Another important parameter is the bending stiffness, as shown in Figure 2.3. Truss

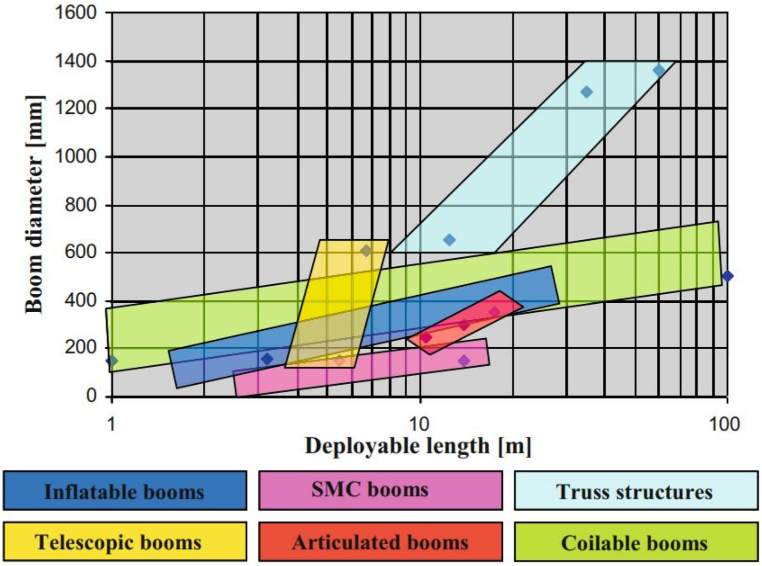

Figure 2.2: Mast diameter as a function of deployable length [1].

structures and articulated booms have the highest bending stiffness, whereas Shape Memory Composite and inflatable booms overlap with the coilable boom. According to the literature, coilable booms offer far wider range of properties than other technologies. Truss structures also have a relatively wide range of lengths at high stiffness, yet at the cost of increased mass.

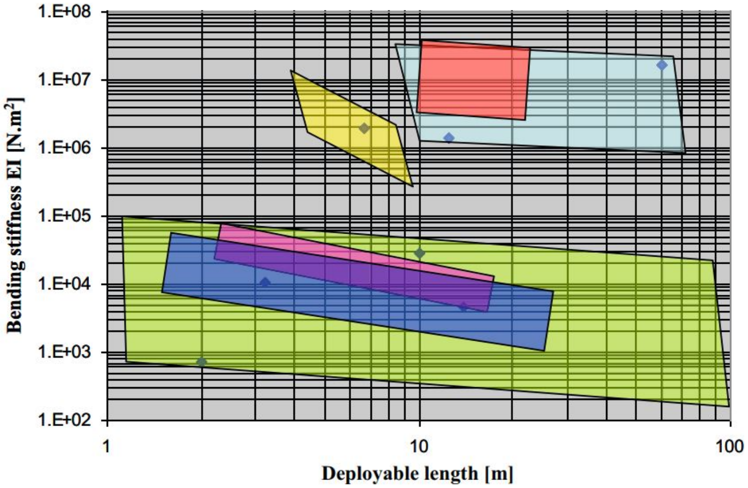

Figure 2.3: Bending stiffness as a function of deployable length [1].

The design flexibility, high packaging ratio and wide range of mechanical properties associated to the coilable mast make it an interesting design concept to explore and adapt when designing a new super-compressible material by a data-driven approach, as proposed herein.

2.1.1. THE COILABLE MAST

Coilable masts are conventional one-dimension deployable structures with high packaging ratio and strength-to-weight ratio, widely applied in spacecraft [11]. Typically, they are lattice trusses with equilateral triangular cross section, designed specifically for purely elastic folding [2, 3]. A coilable mast may be stowed to 2% of the deployment length [12, 13].

Concepts of coilable masts have been developed since the late 1980's, most notably the Astromast [15] and the Simplex Mast [14]. A Simplex Mast consists of at least three continuous longerons, radial spacers and supporting diagonal wires [14]. The longerons form the edges of a truss and the radial spacers are essentially battens hinged to the longerons [3]. According to approximate analytical predictions and extensive experimental investigation, the truss structure is divided into bays by the battens with the length of the bay being approximately 0.6 times the diameter of a deployed mast [3]. The diagonals increase the bending stiffness of the truss. A transition (transfer zone) zone is formed during deployment between the stowed section and the fully deployed section, this is shown schematically in Figure 2.4 [15].

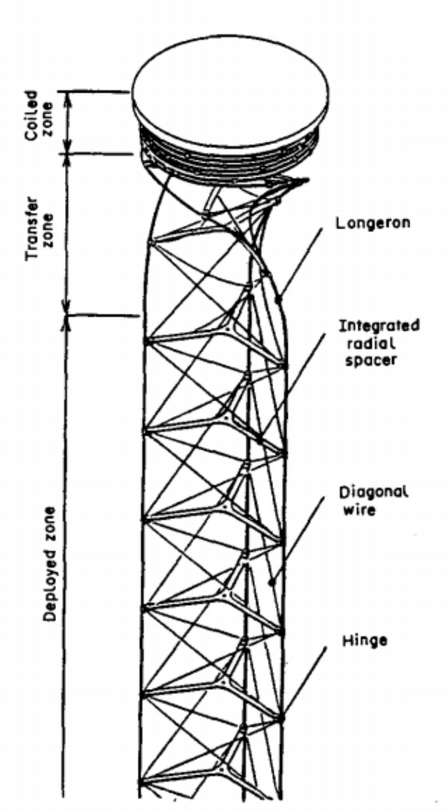

Figure 2.4: Schematic representation of coilable mast [14].

Stored elastic strain energy, triggers the deployment of the mast with a lanyard in tension as the controlling element [3, 13]. The lanyard applies force axially and torque to the top plate, once the mast starts coiling, the lanyard provides the necessary force to fully retract the mast. The stress changes considerably during a full deployment-retraction cycle, with abundant drop after the retraction begins [3, 14].

Despite varied iterations, the design principle is the same. Longerons are the primary load carrying elements, they determine the performance characteristics of the whole mast [13]. The battens buckle and thus tension the diagonals that are responsible for correct alignment of the longerons both radially and axially. It is possible to select different materials for the longerons, battens, and diagonals to manipulate the properties.

Longeron material determines the bending stiffness and bending strength of the mast as they are function of the Young's modulus, distance from mast center, longeron section and bay length. Diagonal material greatly influences the shear and torsional stiffness of the structure as they are function of the elastic modulus and angle within the bay. Moreover, shear and torsional strength are determined by the buckling strength of battens [13].

The design of the coilable mast has been modified over the years, with most notable iteration being the "Hingeless" mast. In this concept, the hinged joints of battens to longerons were removed and replaced by elastic deformation of the batten itself [14], presented in Figure 2.5. The design had several advantages [14]:

- Increased alignment due to fixed joints
- Simplified manufacturing process
- Reduced number of components by 75%
- Reduced mass by 66%
- Lower total cost

Yet, at the time the main problem of the new design was the appropriate batten geometry and material selection for the battens. As masts may undergo plasticity, strain hardening and fatigue [5], relevant selection criteria should consider fatigue properties, creep properties and the material should preferably be a tried space-material [14].

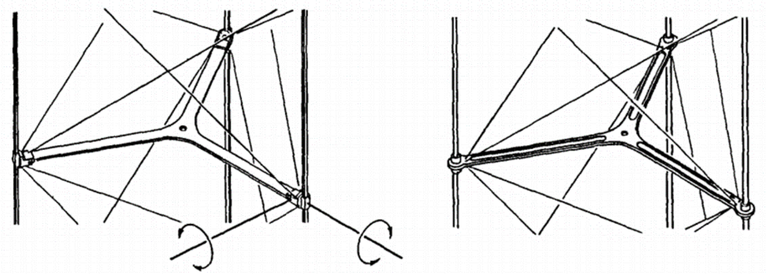

Figure 2.5: Left: Simple mast with hinges. Right: Hingeless mast with rigid joints [14].

Furthermore, one of the main problems of a coilable mast is that it generally has low base frequency and tends to vibrate under both external and internal force in space [12]. These oscillations are unfavorable as it may take a long time for the mast tip to stabilize and function properly after deployment. Additional mass at the tip of the mast has largest influence on this phenomenon. The bending and extensional frequencies tend to decrease at high rate with the increase of mass at the tip. Torsional stiffness is not affected as the additional mass does not change the moment of inertia along the Z axis of the mast [12].

The most characteristic feature of a coilable mast is the transition zone, where the mast is not fully deployed and not fully retracted. This behavior is possible owing to the local coil mode phenomenon.

2.1.2. LOCAL COIL MODE

Essentially, there are two possible deployment modes for a coilable mast: helix mode and the local coil mode, shown in Figure 2.6. The helix mode lacks the discrete separation into the deployed, transition and coiled zones. Instead the entire structure resembles a transition zone. The local coil mode is always preferred over the helix mode, as the mast has higher lateral load resistance during deployment and retraction [11, 14]. On the contrary, a mast in helix mode is characterized by a global instability and low resistance to side forces. As mentioned previously, the elastic strain energy of longerons and battens is the source of deployment forces [14]:

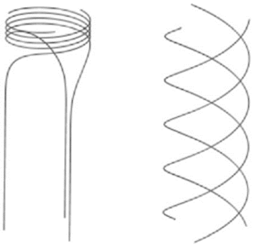

Figure 2.6: Left: Local coil mode. Right: Helix Mode [11].

$$P_D = \frac{6E_I I_I}{D^2} - \frac{3\pi^2 [GJ]_s}{4pD} \tag{2.1}$$

A good selection of values for batten to batten bay length and the stiffness ratio between longerons and battens gives the desired local coil mast appropriate fatigue and creep properties [14].

In order to obtain local coil mode, the mast must be deployed from a fixed bottom first with the longerons uncoiling subsequently from bottom to the top [11]. This ensures global deployment in the local coil mode, regardless of the final length of the mast. Therefore, a longeron boundary condition θ_{ini} affects the bottom deployment mode [11]. The angle θ_{ini} is presented in Figure 2.7. If we take into consideration only the longeron section from the bottom to the first batten, the longerons may be analyzed as twisted elastic rods constrained to a cylinder [11]. Based on the θ_{ini} and bottom deformation analysis, the bottom critical helical angle θ_{crit} may be obtained. If the bottom helical angle changing rate along the longeron curvilinear coordinate is zero, then the mast is in critical state and θ_{crit} value can be determined [11].

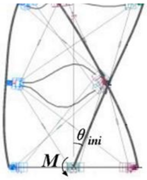

Figure 2.7: Initial bottom helical angle [11].

An experimentally determined condition of $\theta_{ini} < \theta_{crit}$ with a −13.7% margin could ensure bottom deployment in the local coil mode and thus a successful deployment of the entire coilable mast in local coil mode [11]. However, a transition zone with more bays, requires greater θ_{ini}. This is impractical, as the more bays are included into the transition zone, the more the deployment mode resembles the helix mode in 2.6. As stated previously, this leads to lowered stability and lateral bending stiffness of the mast.

2.2. METAMATERIALS

In traditional materials science, materials have been subdivided into three categories: metals, polymers and ceramics. This division is derived from similarity of properties within categories and stark differences between them [16]. As material properties are function of structure and the structure is largely dependent on material chemistry, the types of bonds between atoms determine material properties. Metallic materials are characterized by metallic bonding and are malleable and prone to corrosion. Thanks to ionic bonding in ceramics, they have high melting points, hardness and corrosion resistance yet poor toughness. Polymers are characterized by covalent bonds within the chains and intermolecular forces in between them, therefore they exhibit time-dependent deformation and are lightweight but have lower strength and poor high temperature performance [16]. Later, a fourth category of materials was added, composites. A composite material is formed by combining at least two different constituents with complementary properties with the goal of improving the overall behavior of the material [17].

Recently, a novel category of materials has been intensely researched. Metamaterials are carefully structured materials, often consisting of periodically arranged building blocks, that exhibit properties and functionalities that differ from and surpass those of their constituent materials rather than simply combining them [18]. By this definition, metamaterials bear resemblance in their purpose with composites, however they achieve their functionality by means of meticulous spatial morphology of the constituent phases. Over the last 20 years metamaterials that achieve extraordinary acoustic, thermal and optical properties were demonstrated [18–24].

Mechanical metamaterials are man-made materials, usually consisting of repeating unit cells which are engineered to achieve extreme mechanical properties, often beyond those found in most natural materials [25]. Motion, deformations, stresses and mechanical energy are of prime interest in this class of metamaterials [18]. They are characterized by a set of unusual or extraordinary properties such as negative Poisson ratio [20–22], negative incremental stiffness [26, 27] , negative compressibility [28, 29], bi-stability [30, 31], shape morphing [18, 20, 32], topological protection [18, 20], and nonlinear responses [18, 25], to name just a few.

The so called meta atoms, are the building blocks of metamaterials. Adjacent blocks act jointly to generate collective response [18]. The linchpin to the design of mechanical metamaterials are slender structural elements [18] such as beams, struts, rods and ties. They enable large deformations that lead to geometric nonlinearities, and are vulnerable to elastic instabilities, such as buckling and snapping. As the bending stiffness of slender elements scales with the third power of their thickness, powerful stiffness heterogeneities can be designed and fabricated using additive manufacturing techniques [18]. These heterogeneities are the reason for qualitative differences in properties between metamaterials and their constituent materials.

There are several classes of mechanical metamaterials:

1. Linear mechanical metamaterials [33, 34].
2. Mechanism-based metamaterials [31, 35, 36].
3. Instability-based metamaterials [19, 25, 37, 38].
4. Topological metamaterials [18, 20].

This division between metamaterials is fluid. Linear metamaterials are characterized by unusual parameters of rank-four elastic tensor C_{ijkl} . They consist of conventional elastic elements to create metamaterials with any form of elastic tensor that is not forbidden by thermodynamics [18]. Auxetics are an example of linear mechanical metamaterials. They are characterized by a negative value of Poisson ratio i.e. they contract in the transverse direction under compressive loading regimes. However despite linear response, research has focused on instability induced auxetics [19, 21, 22, 24, 30, 37–40].

Mechanisms are collections of rigid elements linked by flexible hinges that have a geometric design that allows for a zero-energy, free-body motion [18]. This family of metamaterials encompasses various Origami and Kirigami-based planar and spatial structures. They have the ability to change shape upon mechanical trigger and can find future applications for actuation purposes [20, 36, 41–43]. Just as in the previous case, mechanism-based metamaterials can possess auxetic behavior [21]. Topological metamaterials. These metamaterials display properties that are topologically protected. They are not affected by smooth deformations of the underlying geometry or by the presence of disorder [18, 20].

Lastly, instability-based metamaterials. In conventional bulk materials, instabilities are undesirable as they may lead to failure [38] or hinder functioning of product. In instability-based metamaterials, the instabilities are exploited to design advanced materials with innovative properties [25]. This type of metamaterials are the main focus of this work, so they will be reviewed in further detail next.

2.2.1. INSTABILITY-BASED METAMATERIALS

Elastic instabilities and large deformations allow for the achievement of strongly nonlinear relations between macroscopic stresses and strains, even if the material remains in the near-linear regime. Upon application of small forces, slender elements may respond with large displacements, which results in so-called geometric nonlinearities. Symmetric slender elements are prone to buckling instabilities that result in strong yet reversible nonlinearities under precisely set loading conditions [37, 38, 42, 44].

Conventional porous materials, such as metallic foams, are composed of a disordered array of beam-like elements. Their functioning depends on the microscopic geometry and deformation mechanism of the beam-like ligaments, which buckle under compression at relatively low strains and create irreversible deformations in the form of collapse bands that provide an efficient energy-absorbing mechanism [18]. As buckling in elastic architected cellular materials may trigger dramatic homogeneous and reversible pattern transformations , it is now possible to exploit this phenomenon to create improved energy absorbing structures [38]. An excellent example of architected cellular structures and periodic structures are ultralight micro and nano lattices [37, 45–49].

Micro lattices are ordered, periodical tubular structures with a minimum scale of approximately 100 nm, created via different additive manufacturing techniques [45]. Moreover, these structures have controlled hierarchy, each of the elements may be set independently to a largely different dimension of structural features, as presented in Figure 2.8.

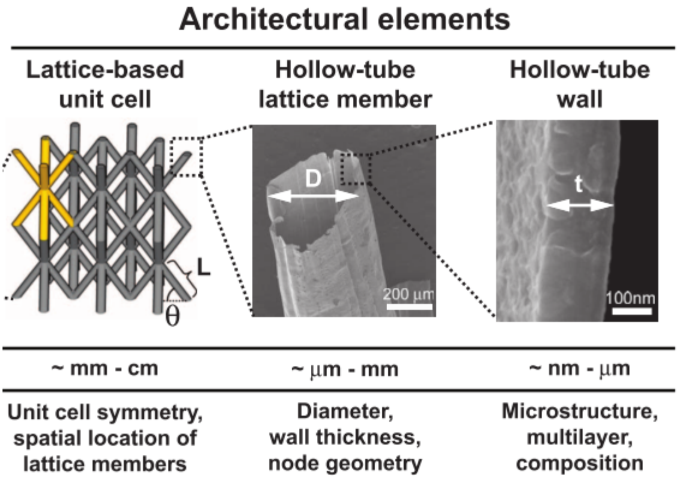

Figure 2.8: Architectural elements of microlattices [45].

These metallic microlattices experience 98% recovery from strains exceeding 50% for the first loading and unloading cycle. However, energy dissipation due to local buckling and node cracking is substantial after the first cycle, see Figure 2.9. Significant damage is made to the lattice in the first cycle, that results in a drop of mechanical properties and subsequent stabilization at the next cycles. The drop was observed to be larger for increased density and tube wall thickness [45].

The observation that scaling down improves the performance lead to emergence of nanolattices [46–48]. The concept was explored further by scaling the lattice down with technical ceramics replacing nickel as the parent material. As seen in Figure 2.10, a new unit cell was considered using Titanium Nitride as parent material with a grain size between 10 and 20 nm and the wall thickness of 75 nm. The result was very high local von Mises stress of 2.5 GPa in a single unit cell, a value close to the theoretical strength of the parent material [46, 47]. This highly unusual behavior for a ceramic material has been ex-

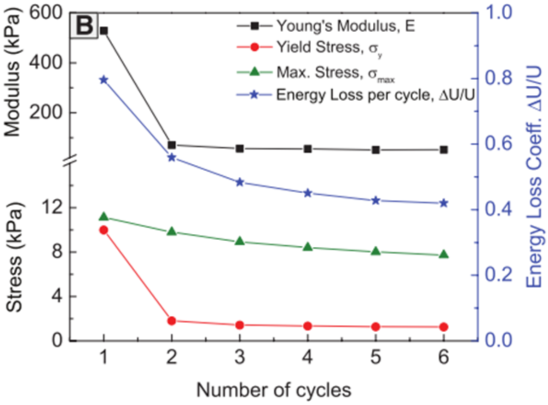

Figure 2.9: Mechanical properties of microlattice as function of number of cycles [45].

plained by a lower probability of finding flaws of critical size. At the length scales of the nano lattice, the critical flaw stress concentration magnitude may be comparable to the one found at grain boundary triple junctions [46, 47]. Moreover, similar cyclic tests have been performed on the nanolattice as on the micro lattice with noticeable performance improvements. The observed hyper elastic behavior was assigned to a purely structural response and not a material response [48].

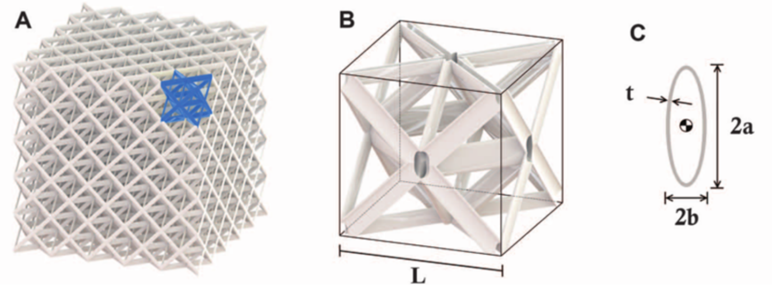

Figure 2.10: Design of nano lattice (A) Whole lattice with unit cell marked (B) Lattice parameter L (C) Hollow tube cross section dimensions [22].

Changing the parent material to alumina, did not change the nature of mechanical response of the lattice. The theoretically brittle metamaterial still showed almost full recoverability after 50% strain [24, 48]. Thickness to semi major axis ratio t/a was correlated with the deformation mode and recoverability [24, 48]. Thick walled structures with $t/a \leq 0.03$ failed catastrophically in a brittle way in the linear elastic regime [22], as expected for the conventional ceramic material. However, thin walled structures with $t/a \leq 0.02$ were characterized by ductile like behavior. After yielding, deformation was accommodated through wrinkling and local buckling of the tube walls [11, 22], as presented in Figure 2.11. Nano lattices with $0.02 \leq t/a \leq 0.03$ showed intermediate behavior in relation to the two extremes.

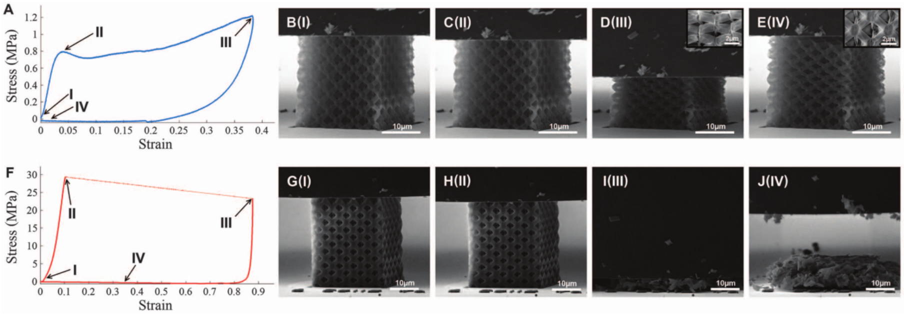

Figure 2.11: Mechanical response of nano lattices (A-E) Thin walled (F-J) Thick walled [22].

Three competing failure mechanisms exist for hollow-tube lattice structures: fracture of the tube wall, beam buckling of a truss member, and shell buckling of the tube wall. Thick walled structures were found to be failing by tube wall fracture, whereas thin walled structures deformed via the shell buckling of tube wall. Reducing the t/a ratio below a critical value, results in deformation mode transition to local shell buckling [11]. As the ratio is further reduced this mode is activated at lower stress, reducing the probability of failure [22].

The examples of micro- and nano-lattices demonstrate that instability-based metamaterials can lead to unusual and often counterintuitive mechanical responses. These responses arise from the combination of length scales chosen for the mechanical elements and their geometrical arrangement to achieve synchronized deformation. The importance of the length scales is evidenced by the change from brittle to ductile macroscopic failure of the material. Therefore, manipulating the characteristic dimensions of the unit cell of the metamaterial leads to significantly altered mechanical response and therefore architectural features of instability-based metamaterials play vital role in achieving the desired material properties [11, 19–23].

2.2.2. BISTABLE SNAPPING METAMATERIALS

Whereas the hollow lattices discussed above store the elastic energy and spring back after the load removal, there are instability based metamaterials that have more than one energetically stable configuration, These materials often explore a rapid and irreversible snap-through instability, allowing them to retain their deformed shape after unloading [18, 25, 50, 51]. Figure 2.12 illustrates the concept of a constrained beam [18, 51].

Constrained beam elements are specifically designed to enable large, local bistable deformations and have the ability of trapping in most of the energy inserted into the system during loading. The amount of trapped energy is simply the difference between the en-

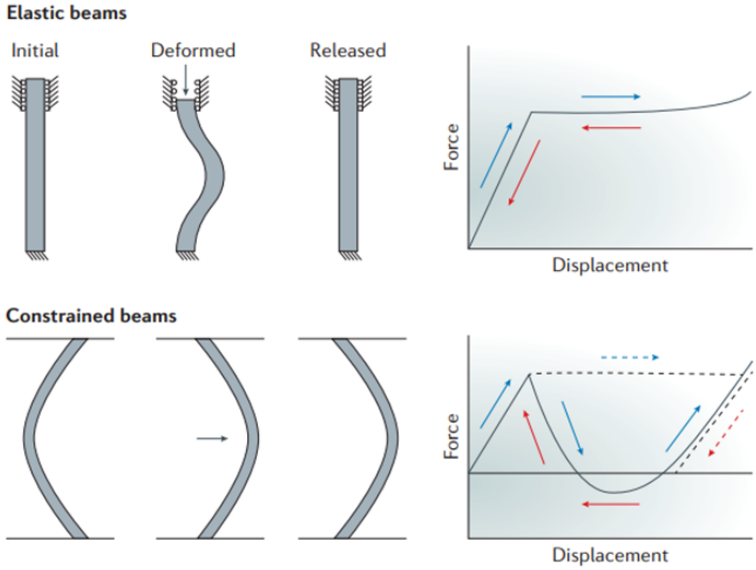

Figure 2.12: Comparison between elastic beams and constrained beams, dashed lines for force controlled bistability [18].

ergy absorbed during deformation and the energy required for the beam to snap back to prior configuration [50, 51]. Figure 2.13 presents an example of tilted constrained beam element used in architected materials that exhibits controlled trapping of elastic energy via bistable snapping. The mechanical response and thus the trapped energy may be tuned by modifying beam slenderness t/L and tilt angle θ [50, 51].

The stress strain curve in Figure 2.13 (b) clearly indicates that as the tilt angle increases, so does the amount of trapped energy. This is further illustrated by the energy maps. For low angle θ, no snapping occurs, and upon increasing the angle, snapping without bistability occurs, no energy is trapped. At nearly vertical angles, likewise no energy is trapped due to lack of snapping. The bistability range is narrowing down for decreasing beam slenderness. The highest energy trapping occurs for t/L high ratio and tilt angles between 50-60^o. The highest snap back energy occurs for the slenderest beams within 60-70^o range. Intuitively one would choose high energy trapping and low energy cost for snap back to maximize energy absorption, however in the case small geometric imperfections, this system may lose the ability to maintain the snapped configuration as the ability arises only from spatial configuration and is both substrate material as well as loading rate independent [51].

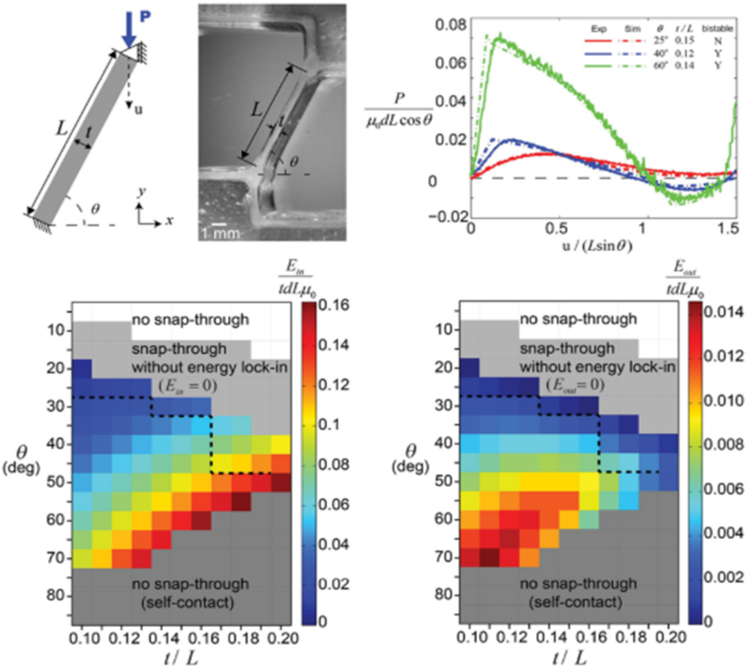

Figure 2.13: Mechanical response of a tilted and constrained elastic beam (a) Characteristic dimensions of the beam (b)Normalized force displacement curves for different tilt angles θ (c) Energy absorbed map (d) Energy cost for snapback map [51].

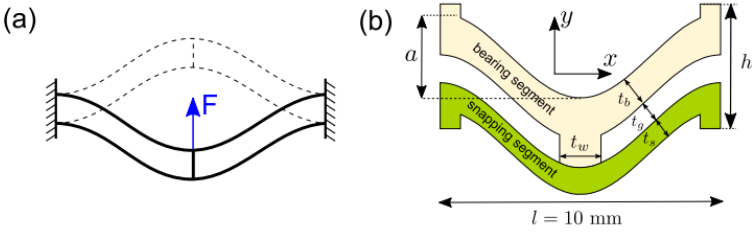

Figure 2.14: Building block of the snapping metamaterial (a) Two stable configurations of a constrained beam (b) Characteristic dimensions of the unit cell [3].

Whereas buckling metamaterial work in compressive regimes, harnessing snapping instability allows to extend the instability-based metamaterials to tensile regimes. As an example, a metamaterial built from periodically arranged snapping units with tunable tensile behavior, capable of large extension caused by sequential, layer-by-layer, snap-through instabilities [25, 50].

Similarly, to the hollow lattices, the snapping metamaterial also has a unit cell, based on the constrained beam, see Figure 2.14. The constrain conditions are released on both ends to create a periodic array of snapping unit cells [25]. At critical stress the lower (green) segment snaps through, and the material responds with a pattern switch from a wavy-shaped structure to a diamond-like arrangement [25]. By manipulating the amplitude a/l of the unit cell, the transformation may be continuous or discretized [25].

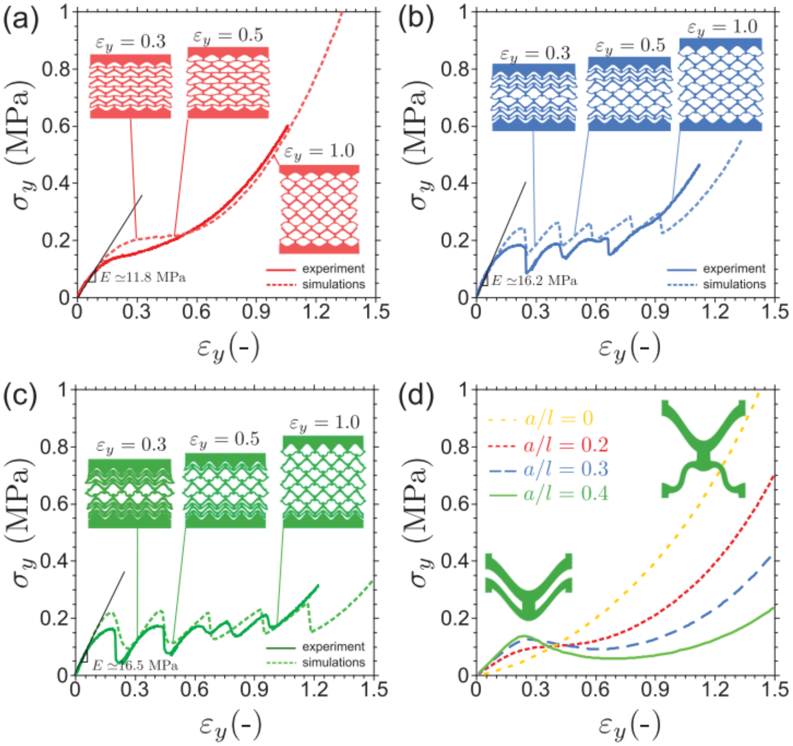

Figure 2.15: Stress strain curves for snapping metamaterial (a) a/l=0.2 (b) a/l=0.3 (c) a/l=0.4 (d) Response of a single unit cell for each amplitude [25].

The stress-strain curves obtained for different a/l amplitudes exhibit three regions, Figure 2.15 [25]:

1. Linear elastic bending in snapping segments up to a critical strain
2. Snapping strain regime, where a further stretching triggers elastic instabilities with negative slope - a negative incremental stiffness.
3. Stiffening regime, dominated by tensile stretching

For $a/l = 0$ the response is monotonic, and the snapping behavior vanishes. The higher the amplitude the more discontinuous the snapping is and for large amplitudes, the instabilities localize.

Many similarities may be observed between the discussed metamaterials. Just as in the case of hollow lattices, characteristic dimensions of material structure allow to manipulate its properties. Unique properties are derived from spatial morphology and elastic deformation modes. Moreover, significant strains coupled with bistability make them suitable candidates for energy absorption and deployable structures, to achieve controlled sequential displacement [25, 50, 51].

2.3. ENERGY ABSORBERS

An energy absorber is a system that converts, entirely or partially, the kinetic energy into a different form of energy (potential energy, heat). The converted energy is either irreversible, in the case of plastic deformation, or reversible like in the case of elastic strain energy in solids [52]. Additionally, it is desirable for energy absorbers to lower the intensity of an impulsive load by extending its duration [53]. Conventionally, energy absorbers are thin walled collapsible metallic structures that work in compression, that dissipate the most of the kinetic energy of an impact [52]. The conversion of the kinetic energy into plastic deformation depends, among other factors, on the magnitude and method of application of loads, transmission rates, deformation or displacement patterns and material properties [54]. Moreover, performance of these structures is highly dependent on properties such as: mode of collapse, strain hardening and strain rate effects [52].

Among these thin walled metallic structures an interesting case is the frustum. Frusta are truncated circular cones that exhibit more stable plastic behavior than cylinders when deformed axially [52]. The post-buckling behavior of frusta is characterized by square proportionality of buckling load increase with a unit increase of cone wall thickness and a decrease of post buckling load with increment of semi-apical angle [55]. One possible mode of deformation of frusta is the direct inversion, see Figure 2.16 [52].

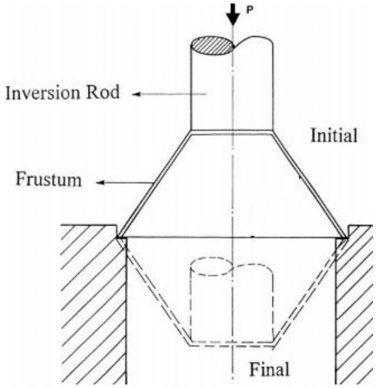

Figure 2.16: Direct inversion of frustum upon applied load [52].

The objective function with many energy absorbers is maximizing the energy absorption per unit volume or per unit mass. This calls for materials with high stiffness, preferably constant deformation stress as well as a maximum densification strain ε_D [53].

Generally, the energy absorbed per unit volume and per unit mass may be expressed by the following equations, respectively [53]:

$$U_V = \int_0^{\varepsilon_D} \sigma \, d\varepsilon \tag{2.2}$$

$$U_M = \int_0^{\varepsilon_D} \frac{\sigma}{\rho} d\varepsilon \tag{2.3}$$

Figure 2.17a shows the idealized energy absorber stress strain curve as well as the stress-strain curve for an actual generic energy absorber [53], in In reality the constant crushing stress “plateau” [56] is difficult to achieve, as most metals harden or soften past yield point.

Therefore, the goal of energy absorbing structures is then to maximize the absorbing efficiency defined as the ratio between the hatched and grey colored area U/Umax as presented in Figure 2.17b.

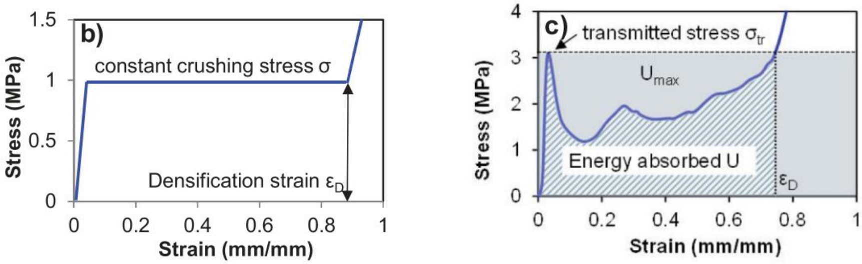

(a) Ideal response (b) Real response

Figure 2.17: Response of an energy absorbing material [53].

Typically the strength and energy absorption of conventional tubes, columns and frusta would be increased by thickening their walls [52, 56, 57]. However, this approach leads to a significant increase in weight comparing to the gain in energy absorption. A substantial increase in energy absorption has been reported in [57] by creating a grid of inner walls with the same thickness as the outer walls, although the weight increase is still considerable in these designs. For applications where minimizing weight is one of main design criterions an alternative filler material for tubes and columns has been proposed using foams [56, 57].

As reported in [56, 58, 59] low density metal filler leads to superior specific energy absorption of thin walled columns comparing to increasing wall thickness. The foam filler in these structures acts as an elastic cushion and causes a decrease of buckling length of sidewalls, which in turn raises the buckling load [57]. In a different study [59], frusta shaped thin-walled structures energy absorption capability with and without metallic foam filler were compared, see Figure 2.18.

The results demonstrated superior performance of foam-filled thin walled structures in comparison to structures without foam-filling [59]. In addition, the buckling load and energy absorption increase significantly as the foam density increases and the increase of semi-apical angle of frustum also contributes to higher energy absorption [59].

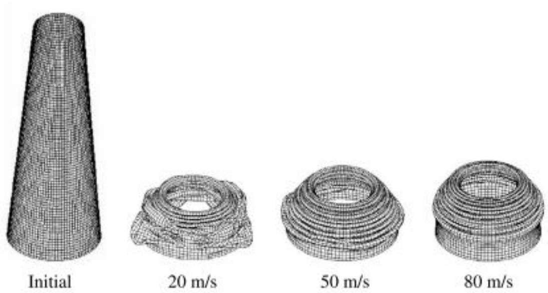

Empty

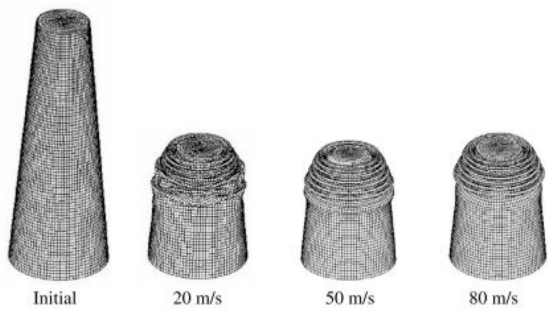

Foam-filled ($\rho_f = 0.534$ g/cm^3)

Figure 2.18: Effect of crushing velocity on empty and foam filled frusta [59].

Foams themselves are not a recent innovation [58, 60], yet their mechanical response makes this class of materials desirable for energy absorption. A typical compressive stress–strain curve, Figure 2.20, of a foam material consists of three regions: a linear-elastic region, a plateau region with deformation at almost constant stress, and a densification region where the cells crush together [57, 60]. The mechanical properties of foams depend, above all else, on the relative density, ρ/ρ_s, where ρ is the density of the foam and ρ_s of the solid of which the foam is made [58, 60]. The stiffness scales quadratically with the density $E \sim \rho^2$, therefore the range of moduli available by foaming spans a factor of 10^4 [60]. Thus, higher relative densities lead to higher stresses under compression, however they reduce the range of the plateau regime [58]. This is pictured in Figure 2.21 which shows stress strain curves of elastomeric foams for different relative densities [60].

Despite extensive research over the years, the energy absorbing properties are far from the ideal described in Figure 2.17. Manmade cellular foams described so far, except honeycomb structures, exhibit random architecture that results in isotropic mechanical response [45, 60]. Additive manufacturing methods have opened new research pathways to find materials with higher specific energy absorption via designing structures with ordered cellular architecture. Relevant metamaterial examples are discussed next.

Ultralight metallic microlattices, discussed for example in [45], are a promising way for-

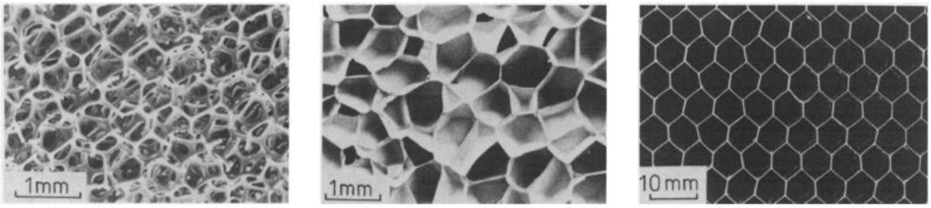

Figure 2.19: Examples of manmade foams [59].

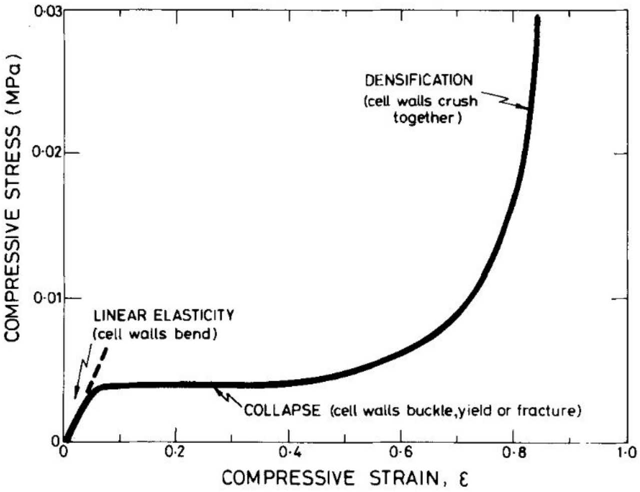

Figure 2.20: Stress strain curves for elastomeric foams with varied relative density [60].

ward in this field. These microlattice structures can be tuned for different mechanical responses depending on the chosen application. Figure 2.22 shows that despite the ordered structure the mechanical response of a microlattice depends highly on the density of the structure. Similarly to foams, structures with higher density exhibit higher strength but lack the plateau-like behavior. An important addition and advantage over foams is partial recoverability of the material after first deformation cycle and a stabilization of performance over several cycles. Kinetic energy is only partially dissipated, and the remainder is stored as elastic energy.

The idea of microlattices for energy absorption has been experimentally explored by different authors. Schaedler et al. [53] explored the use of hierarchical cellular architectures across different length scales to obtain different stress-strain responses. As depicted in Figure 2.23 to achieve a more plateau-like stress-strain response, vertical struts have been added to each unit cell of the lattice. This resulted in superior energy absorption per unit mass and increased absorption efficiency up to 70% [53]. This microlattice design can be compared to conventional energy absorbing materials by a dimensionless

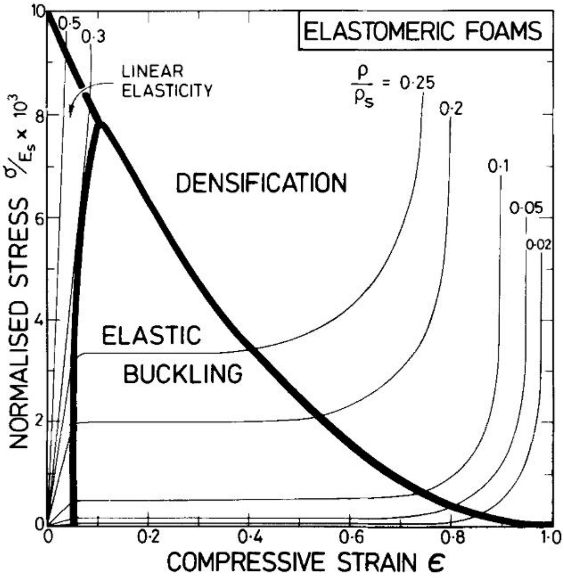

Figure 2.21: Stress strain curves for elastomeric foams with varied relative density [60].

normalized mass-based energy absorption,

$$U_{M,\,norm} = \frac{\rho_s \int_0^{\varepsilon_D} \sigma\, d\varepsilon}{\rho \sigma_y} \tag{2.4}$$

which is introduced in order to distinguish between the effect of architecture from substrate material properties [53]. This design outperforms typical foams due to organized spatial structure and serves as a compromise between the efficiency of precrushed honeycomb and the energy absorption of regular honeycomb.

Table 2.2: Comparison of energy absorbing materials under quasi-static load [53].

Material	ρ [kg.m^{-3}]	ρ/ρ_s [%]	ε_D [%]	η [%]	$U_{M,n}$
Microlattice	97	1.1	81	54	0.15
Al Foam	185	6.8	55	34	0.07
EPS Foam	66	6.2	69	37	0.12
Al Honeycomb	35	1.3	84	40	0.16
Precrushed Honeycomb	38	1.4	80	63	0.13

Most of the materials discussed up to this point were characterized by irreversible conversion of kinetic energy into heat, mainly via plastic deformation. However, the original microlattices discussed in [45] have approximately 50% recoverability via trapping of elastic strain energy. Novel metamaterials, that feature almost full recoverability [25, 31,

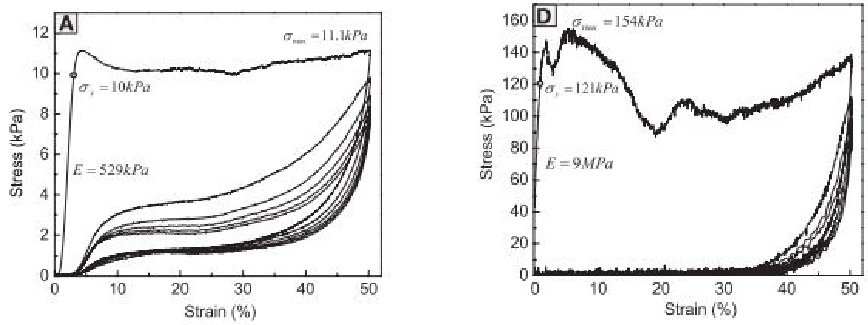

(a) Ideal response

(b) Real response

Figure 2.22: Stress stain response of a microlattice with density of (A) 14 mg/cm^3 (B) 43 mg/cm^3 [45].

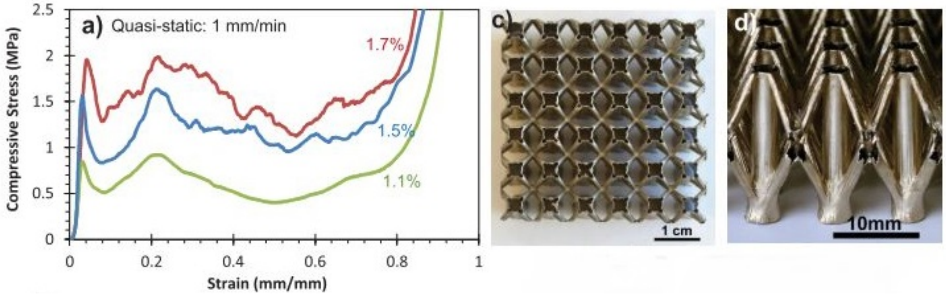

Figure 2.23: Stress strain response of microlattices with vertical posts and different relative densities [53].

51, 61], exploit the concept of bistable snapping of beams discussed previously in this work. Rather than dissipating the kinetic energy in the form of heat, novel architected metamaterials lock-in energy in elastic energy, thus loading process is completely reversible with energy absorption unaffected by the loading rate [49]. Moreover, just as microlattices these materials have tunable properties, hence being suitable for application-specific optimization.

Phase transforming cellular materials [31] are a further extension of the concept. Instead of two stable configurations, this class of materials consist of unit cells with multiple stable configurations. The base material of those metamaterials does not necessarily exhibit phase transformations at the atomic level, instead the unit cells comprise compliant bistable or metastable mechanisms [31]. Virtually any material may be used as substrate if it's yield strength is higher than the stress at any point of unit cell during phase transformation. The stress strain response of these metamaterials is characterized by a serrated plateau region, see Figure 2.24 [31]. The reason for serrated stress-strain behavior is most probably the chosen lengthscale of the unit cell, as presented in Fig-

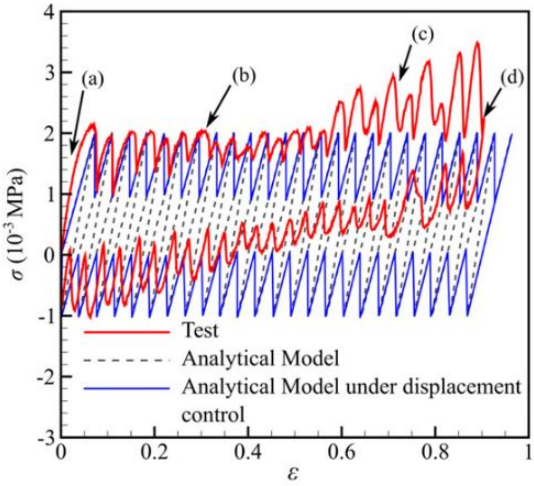

Figure 2.24: Stress strain curves of phase transforming metamaterial [31].

ure 2.25, reducing the size of unit cell would possibly result in a more continous curve, yet the advantage of this length scale it is facile to distinguish descrete snapping events responsible for energy absorption.

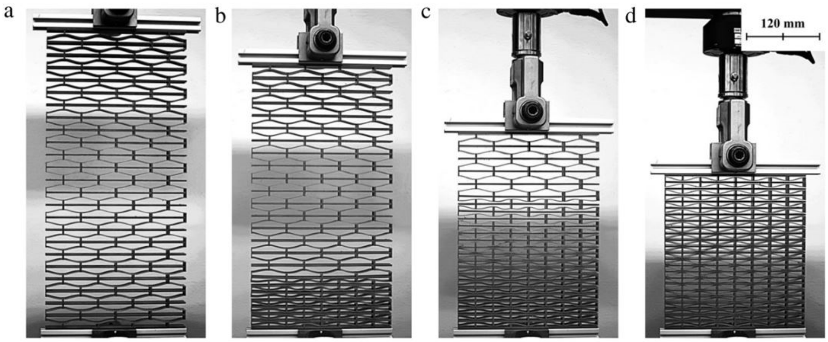

Figure 2.25: Corresponding deformation of phase transforming metamaterial at different strains [31].

Another example of exploiting bistable elastic beams are shape-reconfigurable materials, based on multistable structural unit cells encompassing living hinges [61]. In these cases the unit cell consist of multiple triangular frames in closed and open configurations, so that the bistable hinge mechanism is obtained for every frame. This is the basis for more complicated multi-stable structures with full recoverability. In order to increase the energy absorption capacity, an inclined beam with constant cross section has been replaced with a stepped beam consisting of a relatively thick and rigid section in the middle and two sections of equal length with smaller cross section on the two sides as presented in Figure 2.26. As parameter R approaches unity, the strain energy localizes at the hinges. Snap-through strength increases with R, however this makes hinge design critical and limits the available substrate materials [61], also fatigue considerations must be taken into account.

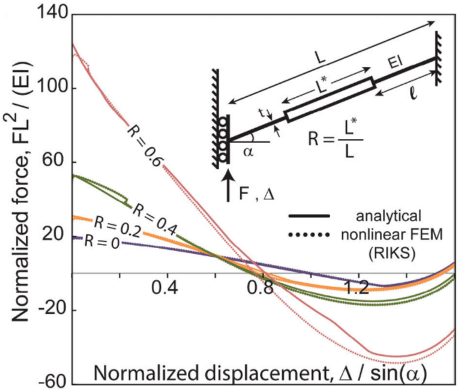

Figure 2.26: Load displacment response of incline guided beam with rigid middle section of different length ratios R [61].

The aspect ratio of hinges t/L plays a crucial role on the structural integrity and mechanical response of the shape-reconfigurable materials, as the strain at the hinges must be lower than the fracture or yield strain of a substrate material. Figure 2.27 depicts the energy density of a stack of unit cells until full densification of the metamaterial. Apart from maximizing parameter R, extending the total length of the beam L and lowering the critical thickness of the hinge lead to high energy absorption per unit volume.The aim is then to find extraordinary output performance from ordinary substrate materials.

It is instructive to compare different materials discussed in this work as well as conventional materials using an Ashby type plot of energy absorption per unit volume as function of compressive strength in Figure 2.28. The plot includes shape-reconfigurable metamaterials with different substrate materials as well as: energy trapping metamaterials [37], ultralight metallic microlattices [45], snapping mechanical metamaterials [25], hierarchical ceramic lattices [45], and phase transforming metamaterials [31].

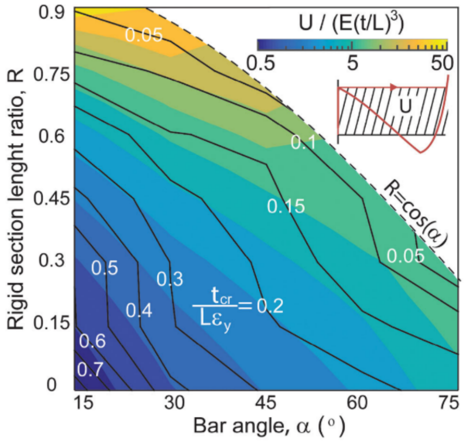

Figure 2.27: Logarithmic-scale contour plot of absorbed energy per unit for the 1D shape-reconfigurable metamaterial as a function of parameters R and α [61].

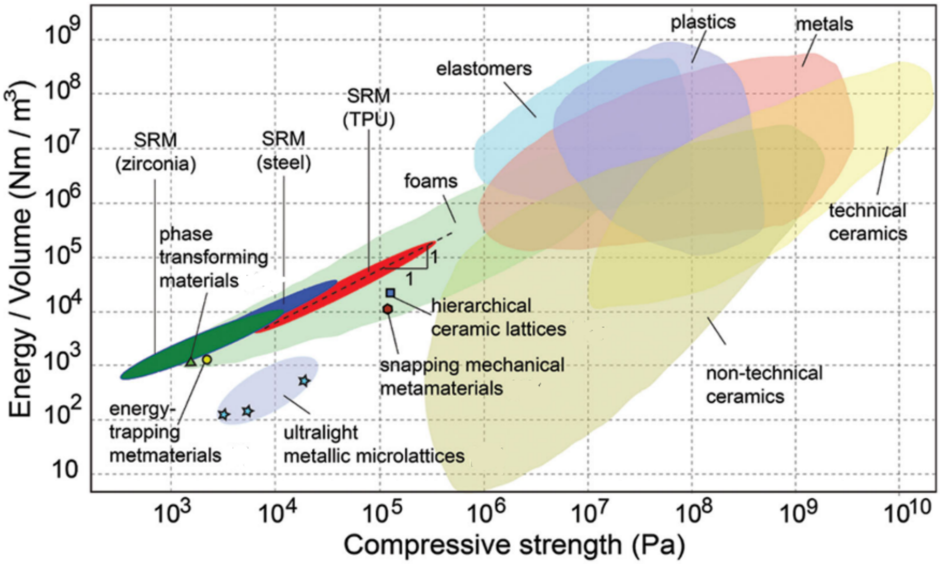

Figure 2.28: Ashby plot of Energy density as function of compressive strength [61].

Rather surprisingly, in this case, TPU based shape-reconfigurable metamaterials outperform metal and ceramic based, owing to the hinge strength limitations discussed. Overall there is still room in the design space for new or better metamaterial designs for energy absorption.

2.4. MACHINE LEARNING

Before focusing on Machine Learning we will first define Pattern Recognition. It is the study of how machines can observe the environment, learn to differentiate patterns of interest from their background, and make sound and reasonable decisions about the categories of the patterns [62, 63].

Possibly the best pattern recognizers that we know are humans, however it is difficult to understand how humans depict patterns [62]. Humans rely on their intelligence for pattern detection that is in turn critical to decision making. In the broadest sense we can define intelligence as a measure of an agent's ability to achieve goals in a wide range of environments [64]. This is one of the reasons that Pattern Recognition falls into the broad spectrum of Artificial Intelligence (AI) [63, 65, 66].

Computers are well capable of preforming iterative tasks, therefore they can be also trained to detect patterns, where pattern may be defined "as opposite of chaos, a vaguely defined entity that could be given a name" [62]. Having a pattern, its detection may be fundamentally separated into two types of tasks [62]:

- Supervised detection– input pattern is identified as a member of a predefined class
- Unsupervised detection– also called clustering, where the pattern is assigned to a previously unknown class.

This distinction will be discussed further in reference to Machine Learning, however it is important that this differentiation refers to prior knowledge of the class, in other words whether one knows what to look for or not. According to Vapnik [67], the problems of pattern recognition, regression estimation and density estimation are similar in nature. That is why most of definitions herein based on classification still hold for regression problems, with the distinction that in classification has a finite set of classes at disposal whereas in regression problems the set of classes is virtually infinite and consists of real numbers.

There exists a wide variety of applications for pattern detection systems, some are summarized in Table 2.3. The common denominator in the presented examples is that the available features need to be extracted and optimized via data-driven approaches rather than respective experts in their fields.

Table 2.3: Examples of pattern detection applications.

Field	Application	Input	Output
Bioinformatics [68]	Sequence analysis	DNA sequence	Known types of gene
Data Mining [65, 69]	Finding meaningful patterns/relations	Points in multi-dimensional space	Clusters/Predefined Values
Speech recognition [70–72]	Chat-bots	Soundwave	Spoken Words
Image analysis [73, 74]	Face recognition	Pixels	Personal Identity

The demand for automatic pattern detection systems has rapidly risen in recent years due to availability of data to analyze and interpret, at the same time computational speed is key [62, 65, 75, 76], that is why pattern detection approach must be tailored to the task at hand. There are four most commonly known approaches for pattern recognition [62]:

1. Template matching
2. Statistical Recognition
3. Structural Matching
4. Neural Networks

Often, these approaches intertwine and overlap in many aspects, sometimes leading to hybrid approaches arising from the technological advance of pattern detection techniques. Neural networks are perhaps the most well-known method as they are valid and commonly used to classify and regress extremely large datasets, in the field referred to as deep learning. Neural networks are out of the scope of this work and the reader is referred to excellent sources for further information [63, 67, 71, 77–79], as a starting point. For the purpose of this work, emphasis is put on the field of data mining using statistical recognition.

It is not uncommon to find terms data mining and machine learning used interchangeably in literature. All these terms befit the activity, yet their meaning is slightly different. Data Mining can be defined as the process of problem solving by analyzing and discovering patterns in data already present in databases [65, 69]. There are three conditions for data mining [65]:

(a) The process is automatic or semiautomatic.

(b) The patterns discovered need to be relevant (provide edge)

(c) The data is easily accessible and readily available in substantial quantities

Patterns that provide edge make it possible to make major predictions on new data and lead to insights that create value, they generate knowledge [69]. That is why Data Mining is a term that answers the question ‘What?’ we are doing with given data, whereas Machine Learning is the term to describe ‘How?’ one can perform Mining operations.

A crude definition of automated learning, more commonly referred to Machine Learning is that we want to program the computers to “learn” from the input (data) at their disposal [75]. A more concise definition of Machine Learning is provided by Mitchell [79]:

Remark 1 *A computer program is said to learn from experience E with respect to some class of tasks T and performance measure P, if its performance in tasks in T as measured by P, improves with experience E.*

One can observe that Machine Learning is inherently tied to performance rather than knowledge, things learn when they change their behavior in a way that makes them perform better in the future [65]. The crucial concept is that of ‘learning’. Generally, learning may be referred to many activities, including mindless actions. In the context of pattern detection, learning implies thinking and purpose, an intention [65]. Without the intent 'learning' may be referred to as 'training' and the latter is only one of the components of the Machine Learning framework. A successful learner ought to be capable to progress from individual examples to broader generalization, to perform inductive reasoning [75]. However, inductive inference does not imply Artificial Intelligence, as it misses a crucial component from the definition formulated by Mitchell [79], the experience. To fix this problem, prior knowledge must be incorporated, that biases the learning mechanism, the so-called inductive bias [75, 78, 79]. Now, if intelligence was previously defined as measure of adaptability, one can see that Machine Learning is an AI technique, as the performance improves with experience. In other words, Machine Learning allows for conversion of examples into knowledge in an intelligent way [66].

It is fair to pose a question, when to use Machine Learning, rather than simply design program to carry out a task? The limiting factor of conventional programs is their rigidity [66, 75], they are not intelligent as they are not able to adapt to changing circumstances. Most common tasks that are too convoluted for ordinary algorithms (not machine learning) include [75, 79]:

1. Tasks Performed by Humans – these include routine tasks such as include driving, speech recognition, facial recognition.
2. Tasks beyond Human Capabilities – these include analysis of very large and complicated datasets; the more data is generated the more difficult it is for human to analyze it.
3. Tasks with variable conditions – in the domains where algorithm must dynamically adapt to changing circumstances

Let us focus on the second task, as this is the domain of Data Mining using Machine Learning [79]. The most common data mining tasks involve a statistical approach. In this approach every pattern is represented in terms of d features or measurements and is viewed as a point in d-dimensional space. The challenge is to choose the features that that allow pattern vectors belonging to different categories to occupy compact and disjoint regions in a d-dimensional feature space [62]. One can identify an issue with a conventional approach when dealing with patterns in 2 dimensions or even in 3 dimensions, but it difficult to fathom determining patterns in a 100-dimensional space using conventional methods. Typically, decision boundaries are determined by the probability distributions of the patterns belonging to each class, which must either be specified or learned (respectively in supervised and unsupervised recognition), alternatively discriminant analysis path can be implemented where parametric form of decision boundary is specified, then the optimal decision boundary of specified form is determined based on classification of training pattern, using for instance the mean squared error criterion [62, 67, 79].

A typical Machine Learning workflow may be represented in the form of PDCA Deming cycle in Figure 2.29. Firstly, a dataset of interest is selected for preprocessing of the data. Generally, preprocessing consists of subprocesses such as labeling the data, normaliza-

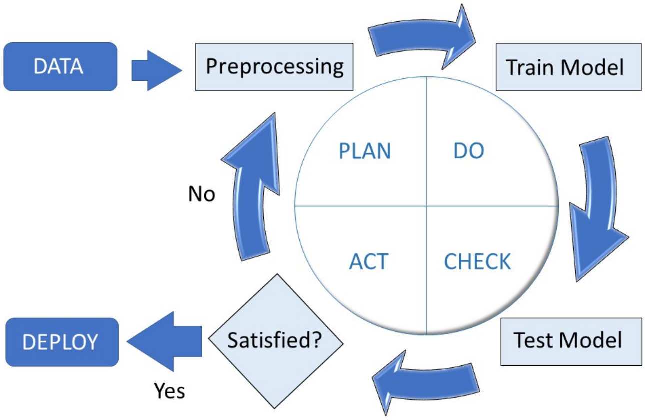

Figure 2.29: Simplified PDCA workflow for Machine Learning.

tion and various transformations [69, 75, 79]. In other words, preprocessing is a set of operations performed on data in order to separate pattern of interest from background and define a condensed representation of the pattern [62]. The data, so-called learners' input, after preprocessing and prior to training has the following structure [66, 75]:

- Input Set – an arbitrary set, X. This is the set of points/observations/attributes/instances that correspond to the values in the output set. Input points are represented by a d-dimensional vector of features. The input set is also referred to as instance space.
- Output Set – in the case of discretized outputs, y, also referred to as labels, it is typically a two-element set of $\{0,1\}$ or $\{-1,1\}$, whereas for continuous outputs it is an infinite set $\{-\inf, \inf\}$ of values.
- Training Set – a proportion of instances $T = ((X_1,\ y_n)...(X_1,\ y_n))$ is a finite sequence of pairs in $(X,\ y)$ that is, a sequence of labeled input instances, randomly chosen from the dataset.
- Test Set – typically a smaller residual proportion of instances $U = ((X_1,\ y_m)...\ (X1,\ y_m))$ from dataset, is a finite sequence of pairs in $(X,\ y)$ that is, a sequence of labeled input instances.

In this way if we combine the input set with output set or training set with test set, one ends up with the starting dataset. After postprocessing, the training set is passed for training, this is the 'learning' part of machine learning, however as discussed previously, this is merely training phase and the cycle is a learning process. The output of training is [75]:

- Prediction rule – is a function of form $h:\ X \rightarrow y$ also called a predictor, hypothesis, regressor or classifier. This hypothesis can be used to predict values of new instances, in other words $output = predictor(input)$, i.e. it provides a mapping $U = predictor(T)$.

Following the training, testing of the predictor is perform to determine the quality of the prediction rule. To perform testing, a performance measure must be established. A popular choice within the Machine Learning community for regression problems is the mean squared error function [69, 75]:

$$MSE = \frac{1}{k}\sum_{i=1}^{k}(Y_i - Y_i^p)^2 \tag{2.5}$$

where Y_i is an output point from the Test set and Y_i^p is the predicted output for the same test instance X. This gives a simple measure where the lower the MSE the better quality of the predictor. If one is content with the performance of the predictor, the model may be deployed for predictions on new input points. If one is not satisfied, the cycle is repeated starting with improving preprocessing of the data. There are numerous methods of improving the model, however for a given learning method, quality of the data is important for improving performance of the model [65].

Problems where both input set and output set are already predefined are known as Supervised Learning. If the desired output consists of one or more continuous variables, then it is a regression task. In this work, emphasis is put on a regression method, the Gaussian Process Regression.

2.4.1. GAUSSIAN PROCESS REGRESSION

There are two possible approaches to the problem of supervised learning. The first approach is to consider a restricted class of functions, whereas the second is to give a prior probability to every function, assuming higher probabilities are given to functions that are more likely [80, 81]. A Gaussian Process uses the second approach, as it is a generalization of a Gaussian probability distribution. It is a stochastic process that governs the properties of functions [80]. This second approach due to being a stochastic process, makes use of Bayesian theory [63].

If one was to consider a regression problem in one dimension, depicted in Figure 2.30 [80], that is the mapping of input x to output $f(x)$, the shaded area represents the probability distribution over functions [81]. To the left of the figure, several random functions are drawn at random from the prior distribution over functions that specified by a Gaussian process that promotes smooth functions, as the *prior* represents one's beliefs of expected functions before observing any datapoints. It is also assumed that the average value over sample functions is in fact zero [80]. It is possible to characterize the variability of sample functions at any value of x by computing the variance at that point. In Figure 2.30 it may be observed that the prior variance does not depend on the input x.

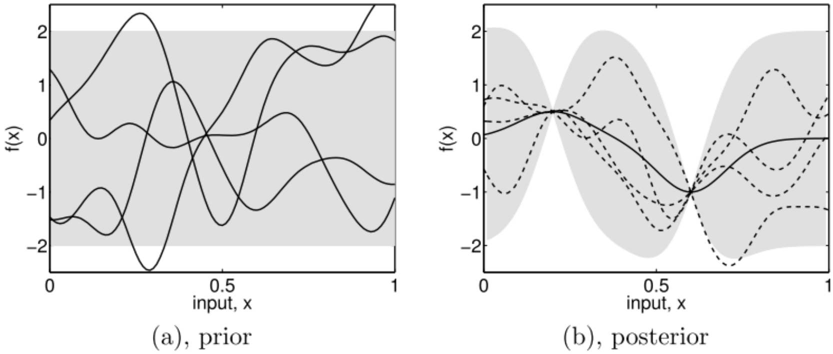

Figure 2.30: (a) Set of random function that fulfill the prior (b) Functions adapted to pass through the two added datapoints creating a posterior distribution [82].

Now looking to the right at Figure 2.30 (b), if one considers functions that pass exactly through two points, the dashed lines show functions consistent with the added points and the solid line is the mean value of these functions, as well as the contraction of the probability distribution at the data points [80]. Combining prior and the likelihood associated with the data points leads to a posterior distribution over functions [63, 66, 69, 80]. The functions in Figure 2.30 (a) are smooth and stationary, as induced by the covariance function of the gaussian process. The task of machine learning using gaussian processes is the problem of optimizing parameters of the covariance function.

To understand the importance of the covariance function it is imperative to introduce the *kernel*. Generally speaking, most of machine learning techniques are parametric, in that they learn so-called weights vector and the training data is made redundant for predictions [63]. The exception are algorithms, which utilize stored training instances for making predictions. These memory-based methods require a measurement of similarity between any two vectors in the input space and generally are rapid to train yet stagnant at making predictions [63, 81]. Some parametric models can be transformed into an equivalent 'dual representation', where the predictions are based on linear combinations of kernel function evaluated at training instances. Given a fixed nonlinear feature space mapping $\varphi(x)$, the kernel functions is defined [63]:

$$\kappa(x,x') = \varphi(x)^T \varphi(x') \tag{2.6}$$

A kernel is a symmetric function of its inputs so that $\kappa(x,x') = \kappa(x',x)$. There are many forms of kernel functions available. In order for a kernel function to be valid it must be symmetric and positive semidefinite, and a suitable form of similarity between x and x' is required [63]. Stationary kernels are a function of the difference between arguments, $\kappa(x,x') = \kappa(x-x')$ and are invariant to translations in the input space [63, 80]. Furthermore homogeneous or Radial Basis Kernels, are distance dependent, $\kappa(x,x') = ||\kappa(x-x')||$.

The ’dual representation’ may be shown by the example of linear regression. Expressing the sum of squares error in a linear regressor as [63]:

$$\mathscr{J}(w) = \frac{1}{2}\sum_{n=1}^{N}\{w^T\varphi(x_n) - t_n\}^2 + \frac{\lambda}{2}w^T w \tag{2.7}$$

Setting the gradient of $\mathscr{J}(w)$ to zero, the solution for w is a linear combination of vectors $\varphi(x_n)$ and the coefficients are functions of vector w:

$$\mathbf{w} = \boldsymbol{\varphi}^T\mathbf{a} \tag{2.8}$$

In the equation above $\boldsymbol{\varphi}$ is the design matrix with row n given by $\varphi(x_n)$ and the vector $a = (a_1, \ldots, a_N)^T$ as well as having [63]:

$$a_n = -\frac{1}{\lambda}\{w^T\varphi(x_n) - t_n\} \tag{2.9}$$

It is possible now to obtain the ’dual representation’ by substituting the parameter in place of the weights vector using the equation (3):

$$\mathscr{J}(w) = \frac{1}{2}\mathbf{a}^T\boldsymbol{\varphi}\boldsymbol{\varphi}^T\boldsymbol{\varphi}\boldsymbol{\varphi}^T\mathbf{a} - \mathbf{a}^T\boldsymbol{\varphi}\boldsymbol{\varphi}^T\mathbf{t} + \frac{1}{2}\mathbf{t}^T\mathbf{t} + \frac{\lambda}{2}\mathbf{a}^T\boldsymbol{\varphi}\boldsymbol{\varphi}^T\mathbf{a} \tag{2.10}$$

where $\mathbf{t} = (t_1, \ldots, t_N)^T$. If one was to define a symmetric $N \times N$ matrix of form $\mathbf{K} = \boldsymbol{\varphi}\boldsymbol{\varphi}^T$ with elements $K_{nm} = \kappa(x_n, x_m)$ then if κ is the covariance function, $\mathbf{K}$ is the covariance matrix. Now we may reformulate $\mathscr{J}$:

$$\mathscr{J}(w) = \frac{1}{2}\mathbf{a}^T\mathbf{K}\mathbf{K}\mathbf{a} - \mathbf{a}^T\mathbf{K}\mathbf{K}\mathbf{t} + \frac{1}{2}\mathbf{t}^T\mathbf{t} + \frac{\lambda}{2}\mathbf{a}^T\mathbf{K}\mathbf{K}\mathbf{a} \tag{2.11}$$

Establishing a zero gradient of $\mathscr{J}(\mathbf{a})$ one obtains $a = (K + \lambda\mathbf{I}_N)^{-1}\mathbf{t}$ and substituting back in the regression model, a prediction for the new input x is:

$$y(x) = \mathbf{w}^T\boldsymbol{\varphi}(x) = \mathbf{a}^T\boldsymbol{\varphi}(x) = \kappa(x)^T(\mathbf{K} + \lambda\mathbf{I}_N)^{-1}\mathbf{t} \tag{2.12}$$

In this case the least-squares problem is composed only of the covariance function κ, and a prediction at new input x is given by linear combination of output values from the training set [63]. Within the dual formulation the parameter vector **a** is determined via inversion of **K**, this is computationally expensive however it is completely expressed in terms of kernel function κ. This allows to operate directly on kernels and skip the introduction of feature vector $\boldsymbol{\varphi}(x)$, thus essentially allowing to use feature spaces of virtually infinite dimensionality [63, 80–82]. The duality may be also shown between probabilistic linear models for regression and the Gaussian Processes method [63]. A valid kernel corresponds to a scalar product in some attribute space, it is therefore fundamental to

Gaussian Process Regression. In the Gaussian process framework, the parametric model is discarded and a prior is defined over functions directly [63].

The linear regression task in the Bayesian framework may be summarized in the following way, assuming an independent constant gaussian noise variance component σ_n^2:

$$y(x) = \mathbf{w}^T \varphi(x) + \epsilon \tag{2.13}$$

where $\epsilon \sim \mathcal{N}(0, \sigma_n^2)$.

This gives rise to the probability density of the observations given parameters, also called likelihood:

$$p(\mathbf{y}|\boldsymbol{\varphi}, \mathbf{w}) = \mathcal{N}(\mathbf{w}^T \boldsymbol{\varphi}, \sigma_n^2 \mathbf{I}) \tag{2.14}$$

With the Bayes rule stating:

$$\text{posterior} = \frac{\text{likelihood} \times \text{prior}}{\text{marginal likelihood}} \Leftrightarrow p(\mathbf{w}|\mathbf{y}, \boldsymbol{\varphi}) = \frac{p(\mathbf{y}|\boldsymbol{\varphi}, \mathbf{w})\, p(\mathbf{w})}{p(\mathbf{y}|\boldsymbol{\varphi})} \tag{2.15}$$

To calculate the posterior, it is necessary to specify a gaussian prior in terms of mean and covariance matrix:

$$\mathbf{w} \sim \mathcal{N}(0, \mathbf{K}) \tag{2.16}$$

with the normalizing constant referred to as the marginal likelihood being independent of the weight vector w:

$$p(\mathbf{y}|\boldsymbol{\varphi}) = \int p(\mathbf{y}|\boldsymbol{\varphi}, \mathbf{w})\, p(\mathbf{w})\, d\mathbf{w} \tag{2.17}$$

The posterior then combines all the knowledge about the parameters and takes Gaussian form [80]:

$$p(\mathbf{y}|\boldsymbol{\varphi}) \sim \mathcal{N}\left(\frac{1}{\sigma_n^2} A^{-1} \boldsymbol{\varphi} \mathbf{y}, A^{-1}\right) \tag{2.18}$$

where $A = \sigma_n^{-2} \boldsymbol{\varphi} \boldsymbol{\varphi}^T + \mathbf{K}^{-1}$

For any given gaussian posterior, the mean of the posterior corresponds to the mode of the distribution, this property is referred to as the maximum a posteriori (MAP) estimate of weight vector w. In Bayesian framework the MAP plays no role, however in non-Bayesian setting the MAP point it the penalized maximum likelihood estimate of the weights [63].

Considering inference directly in the function-space, a Gaussian process is a collection of random variables, any finite number of which have a joint Gaussian distribution [63, 80, 81].

A gaussian process is completely specified in terms of expectations, by the mean and covariance function:

$$m(x) = \mathbb{E}\left[f(x)\right] \kappa(x,x') = \mathbb{E}\left[(f(x)-m(x))(f(x')-m(x'))\right] \tag{2.19}$$

Therefore the gaussian process takes the form [63, 80]:

$$f(x) \sim \mathscr{GP}\left(m(x), \kappa(x,x')\right) \tag{2.20}$$

One can see that if one was to assume the mean function to be zero, gaussian process is completely specified by the kernel. The marginalization property of gaussian processes means that the examination of larger set of points must result in the same distribution as in a smaller sub-set, a submatrix of the covariance matrix is consistent with the parent matrix.

The most common choice for the kernel is the Squared Exponential kernel also referred to as the Gaussian kernel [63].

$$\mathscr{SE} = \kappa(x,x') = \exp\left(-\frac{1}{2}|x-x'|^2\right) \tag{2.21}$$

This kernel is also very often referred to as the Radial Basis Function in literature [80]. The main property of this kernel is the infinite differentiability, thus the process is infinitely mean square differentiable [80]. The kernel may be controlled by normalizing the distance between points by a constant l to change the length scale of the process and by a positive constant σ_f before the exponent to modify the variance of the process. Considering the gaussian noise as defined previously one can rewrite the square exponential kernel in one dimension as:

$$\mathscr{SE} = \sigma_f^2 \exp\left(-\frac{1}{2l^2}|x-x'|^2\right) + \sigma_n^2 \tag{2.22}$$

These three parameters, namely the length scale, process variance and noise variance, can be varied and optimized, one may refer to them as the hyperparameters and the learning process in the framework of gaussian processes is about adapting the hyperparameters of the kernel to suit a given task.

The key predictive equation for gaussian process regression is the posterior process:

$$\mathbf{f}_*|X,y,X_* \sim \mathscr{N}(\mathbb{E}[f_*|X,y,X_*], \mathbf{K}(X_*,X_*) - \mathbf{K}(X_*,X_*)[\mathbf{K}(X,X)+\sigma_n^2\mathbf{I}]^{-1}\mathbf{K}(X,X_*) \tag{2.23}$$

The term $\mathbf{K}(X*, X*)$ is the prior covariance matrix. Having the prediction for the function $f(x)$ it is straightforward to compute the predictive distribution of the noise corrupted output by adding a diagonal noise matrix to the process variance [80].

The expression for log marginal likelihood is:

$$\log\left(p(y|X)\right) = -\frac{1}{2}\mathbf{y}^T(\mathbf{K}+\sigma_n^2\mathbf{I})^{-1}\mathbf{y} - \frac{1}{2}\log|\mathbf{K}+\sigma_n^2\mathbf{I}| - \frac{n}{2}\log(2\pi) \tag{2.24}$$

In non-Bayesian setting the model is trained by minimizing the loss function, such as the MSE introduced before. In Bayesian framework, there is no distinction between the likelihood used for training and the loss function, as the likelihood describes the deviation of noisy measurements from the noiseless function [80].

2.4.2. SPARSE GAUSSIAN PROCESS REGRESSION

While Gaussian Process framework has numerous advantages, uncertainty quantification being the major one, the serious drawback is that it suffers from cubic time complexity to training size $\mathcal{O}(n^3)$ [63, 80, 83–91]. This complexity arises from the necessity to calculate the determinant and inverse of the $n \times n$ covariance matrix $K_{nn} = \kappa(x, x')$ [80, 83, 90]. This essentially limits the applicability of GPs to datasets of size less than $\mathcal{O}(10^4)$ [83]. Recently however, much research has been devoted to solving this limitation by introducing the scalable GP that aims at improving the scalability of a full GP while retaining satisfactory prediction quality for large datasets [83].

Broadly speaking, the scalable GPs may be divided into Global approximations and Local approximations [83]. The difference lies in the approach taken, whereas the former approximate the covariance matrix through global refining, the latter take so-called divide-and-conquer approach to focus on local subsets of data [83]. As a result the global approximations ignore local deviations in favor of capturing global patterns and local approximations focus on local patterns risking local overfitting and discontinuous predictions. Due to software availability and the fact that global approximations work well with slow varying features with high spatial correlations [83], global approximations will be further considered.

As may be inferred from Figure 2.31, the global approximations may be categorized further down. Three main method categories arise [63, 80, 89]:

- Subset-of-Data – where a random subset of training data m, with $m << n$, is selected for actual training resulting in a smaller covariance matrix K_{mm}
- Sparse Kernels – where unimportant entries of the covariance matrix are replaced by zeros resulting in a sparse covariance matrix K_{nn} where most of entries are zeros.
- Sparse approximation – where a low rank representation is measured between m inducing points and n training points resulting in exact or modified Nystrom approximation of form $K_{nn} \approx K_{nm}K_{mm}K_{mn}$

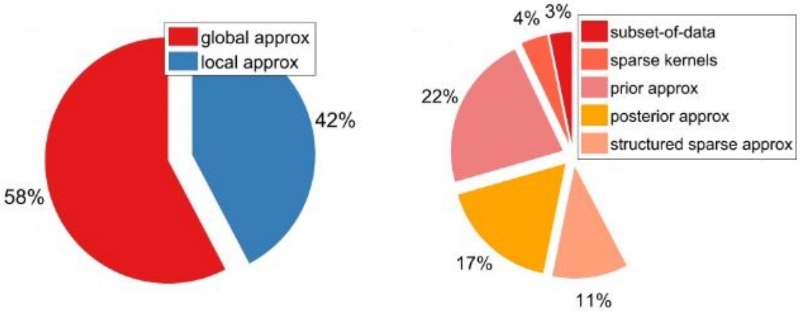

Figure 2.31: Left: Proportion of methods falling into global and local approximations. Right: Subdivision of global approximations [83].

The sparse approximations may be further subdivided into prior approximations where prior is modified but the inference is exact, and posterior approximations where the prior is exact but the posterior distribution is approximated [63, 85, 89]. The complexity for prior and posterior approximations is reduced to $\mathcal{O}(nm^2)$ [83–85, 90]. Very recently developed methods in which inducing points are organized into Kronecker structure achieve complexity of $\mathcal{O}(n)$ or approaches utilizing stochastic optimization with complexity of $\mathcal{O}(m^3)$ [83, 92].

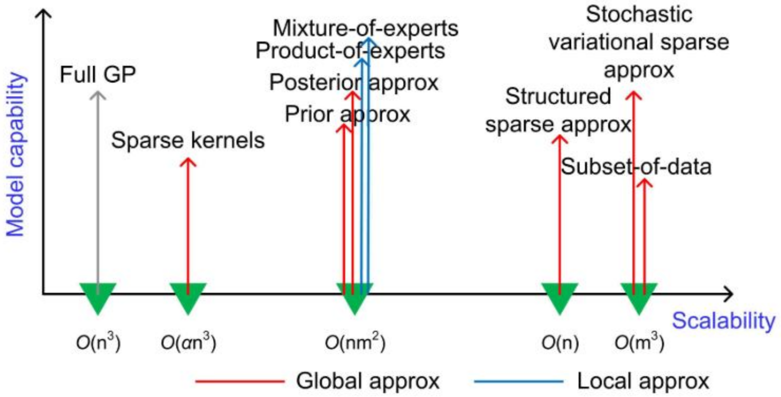

Figure 2.32: Comparison of scalability and capability of GP approximations and Full GP [83].

As one may observe in Figure 2.32 sparse kernels are a relatively poor scalable alternative as the minor complexity reduction results in lower model capability at prediction. Subset of data has the same scalability as stochastic variational sparse approximation but low model capability. Most of the scalable models are in the middle of axis with complexity

$\mathcal{O}(nm^2)$, this is also the complexity of local approximations. One can also observe that local approximations can achieve higher model capability, but as mentioned before this comes at a risk of overfitting the model. Further emphasis will be put on global prior and posterior approximations.

2.4.3. SPARSE PRIOR APPROXIMATIONS

All sparse approximations rely on the Nystrom approximation for the covariance matrix.

$$K_{nn} \approx Q_{nn} = K_{nn} K_{mm}^{-1} K_{mn}^{T} \tag{2.25}$$

Yet, this approach has a design flaw that it may result in negative prediction variances [80]. This is caused by two factors: it is not a generative probabilistic model as the approximation is applied only to training data and it can not guarantee positive semidefinite covariance matrix [83]. All of the prior approximations aim at modifying the Nystrom approximation into GP to produce unifying and principled generative probabilistic model [63, 83, 84, 90]. The sparsity is achieved by m inducing points that represent the entire training data. Now, introducing the set of inducing inputs as X_m and the corresponding inducing variables as f_m as well as function values of a gaussian process f for training cases and f^* for test cases [83, 89]. The inducing variables are assumed to be statistically sufficient for f and are always marginalized out of the predictive distribution, however the choice of the inducing inputs does affect quality of the model [83, 89]. In some algorithms inducing inputs are a subset of the training set whereas in other methods they are not [89]. Due to consistency of GPs we can recover $p(f,\ f^*)$ by integrating out f_m from the joint GP prior $p(f,\ f^*,\ f_m)$ [89]:

$$p(f, f^*) = \int p(f,\ f^*|f_m) p(f_m) df_m \tag{2.26}$$

where $p(f_m) = \mathcal{N}(0,\ K_{mm})$.

All prior approximations approximate the joint prior $p(f,\ f^*)$ but perform exact inference [83]. Quinonero-Candela and Rasmussen [83] provide an excellent review and comparison of sparse prior approximations, for the purpose of this work relevant fragments will be presented.

In sparse prior approximations, equation (22) is fundamental for all the methods. One approximates the joint prior assuming $f,\ f^*$ are conditionally independent given f_m.

$$p(f, f^*) \approx q(f, f^*) = \int p(f,\ f_m) q(f^*,\ f_m) p(f_m) df_m \tag{2.27}$$

The variable f_m is an inducing variable since the dependencies between f and f^* are induced only through f_m [89]. The proposed inference methods place additional assumptions on the inducing conditionals $q(f|f_m)$ and $q(f^*|f_m)$ of the integral [89]. Now the training and test conditionals are given as [83, 89]:

$$p(f, f_m) = \mathcal{N}\left(f|\mathbf{K}_{nm}\mathbf{K}_{mm}^{-1}f_m, \mathbf{Q}_{nn}\right) \tag{2.28}$$

$$p(f, f_m) = \mathcal{N}\left(f|\mathbf{k}_m^*\mathbf{K}_{mm}^{-1}f_m, \mathbf{Q}^{**}\right) \tag{2.29}$$

Essentially **Q** quantifies how much information does the inducing variable provide about f or f^* [89]. The log marginal likelihood is approximated as [83]:

$$\log\left(q(y)\right) = -\frac{n}{2}\log(2\pi) - \frac{1}{2}\log|\tilde{\mathbf{Q}}_{nn} + \mathbf{Q}_{nn} + \sigma_\epsilon^2\mathbf{I}_{nn}| - \frac{1}{2}\mathbf{y}^T\left(\tilde{\mathbf{Q}}_{nn}\mathbf{Q}_{nn} + \sigma_\epsilon^2\mathbf{I}_{nn}\right)^{-1}\mathbf{y} \tag{2.30}$$

Again, the two methods presented shortly will correspond to different approximations of the conditionals in equations (22) and (23) [80, 83, 89].

The Deterministic Training Conditional (DTC) also called Projected Latent Variables [81] or Projected Process Approximation [80] imposes a deterministic training conditional but retains the exact test conditional:

$$q_{DTC}(\mathbf{f}|\mathbf{f}_m) = \mathcal{N}\left(\mathbf{f}|\mathbf{K}_{nm}\mathbf{K}_{mm}^{-1}\mathbf{f}_m, 0\right) \tag{2.31}$$

$$q_{DTC}(\mathbf{f}|\mathbf{f}_m) = p(\mathbf{f}^*|\mathbf{f}_m) \tag{2.32}$$

Due to inconsistent conditionals the DTC approximation is not an exact GP. The method relies on likelihood approximation [80]:

$$p(y|f) \approx q(y|f_m) = \mathcal{N}(\mathbf{K}_n m\mathbf{K}_m^{-1} m f_m,\ \sigma_\epsilon^2\mathbf{I}) \tag{2.33}$$

The DTC was an important step but it is a rather crude estimation and does not perform well due to the strict assumption $\mathbf{Q}_{nn} = 0$ that arises if one compares equations (23) and (26) [89].

The second relevant sparse prior approximation is the Fully Independent Training Conditional (FITC) [83, 85], originally referred to as the Sparse Gaussian Process using Pseudo Inputs (SGPP) [90, 93]. FITC imposes a fully independence assumption to remove the dependency among $\{f_i\}_{i=1}^n$ such that given $\mathbf{V}_{nn} = \mathbf{K}_{nn} - \mathbf{Q}_{nn}$ [84, 90]:

$$q_{FITC}(\mathbf{f}|\mathbf{f}_m) = \Pi_{i=1}^n p(f_i|f_m) = \mathcal{N}\left(\mathbf{f}|\mathbf{K}_{nm}\mathbf{K}_{mm}^{-1}\mathbf{f}_m, diag[\mathbf{V}_{nn}]\right) \tag{2.34}$$

$$q_{FITC}(\mathbf{f}|\mathbf{f}_m) = p(\mathbf{f}^*|\mathbf{f}_m) \tag{2.35}$$

One can see that the same test conditional is used as in the DTC approximation. FITC approximation does not impose a deterministic relation between f and f_m. It proposes an approximation to the training conditional distribution of f given f_m as a further independence assumption [84]. The main difference between FITC and DTC is that it replaces the approximate covariances of DTC by exact ones on the diagonal. The computational complexity is exactly the same as for DTC approximation [84, 90]. The FITC approximation proposes a more sophisticated likelihood approximation with enhanced covariance [83]:

$$p(y|\mathbf{f}) \approx q(y|\mathbf{f}_m) = \mathcal{N}\left(\mathbf{K}_{nm}\mathbf{K}_{mm}^{-1}\mathbf{f}_m, diag[\mathbf{V}_{nn}] + \sigma_\epsilon^2\mathbf{I}\right) \tag{2.36}$$

FITC may be viewed as a standard GP with a non-stationary covariance function parametrized by inducing inputs [83]. The covariance component $diag[\mathbf{V}_{nn}]$ represents the posterior variances of latent variables $\mathbf{f}$ given the inducing variables $\mathbf{f}_m$. These varying variances, which are zeros at inducing points, enable FITC to capture noise heteroscedasticity (variable noise component per input point) [84, 90]. This property comes at a cost of producing severe underestimation of noise variance and sacrificing the accuracy of prediction mean [83]. Another drawback is that FITC is relatively expensive to train as the optimization over inducing inputs introduces $m \times d$ parameters and makes inference a computationally intractable task due to the high dimensional space [90]. The heteroscedasticity of FITC implies that it attempts to achieve a desirable predictive accuracy at low computing cost, rather than truthfully recovering the regular GP with increasing m [83]. Learning inducing points via the optimization of log marginal likelihood may produce poor predictions just as in the case of DTC approximation [83]. Most of the issues of the sparse prior approximations are addressed by the sparse posterior approximations.

2.4.4. SPARSE POSTERIOR APPROXIMATIONS

Just as in the case of prior approximations, posterior approximations rely on the Nystrom relation. The basis for posterior approximations is the Variational Free Energy (VFE) approximation formulated by Titsias [83–85, 88]. It utilizes variational inference to approximate the true posterior distribution [84]. The fundamental assumption behind this approximation is that the inducing inputs are defined as variational parameters which are selected by minimizing the so-called *Kullback-Leibler* (KL) divergence between the exact GP posterior and the inferred variational GP distribution over latent function values [88]. This addressed some of the drawbacks of the prior approximations as VFE formulation avoids overfitting and rigorously approximates the exact GP model by minimizing the distance between the sparse GP and conventional GP [83, 85, 88].

The whole idea of VFE approximation is to directly approximate the posterior distribution $p(f, f_m|y)$ with a variational distribution $q(f, f_m|y)$ [88]. Then the goal is to reduce the difference between these two distributions using the KL divergence [85–88].

$$\mathbb{KL}\left(q(\mathbf{f},\mathbf{f}_m\ \mathbf{y})\right)||p\left(\mathbf{f}\mathbf{f}_m|\mathbf{y})\right) = \left\langle \log\frac{p(\mathbf{y},\mathbf{f},\mathbf{f}_m)}{q(\mathbf{f},\mathbf{f}^*,\mathbf{y})}\right\rangle q(\mathbf{f},\mathbf{f}^*|\mathbf{y}) + \log\left(p(\mathbf{y})\right) = -F_q + \log\left(p(\mathbf{y})\right) \tag{2.37}$$

In this equation quantity F_q is the so-called Evidence Lower Bound (ELBO), also referred to as the Variational Free Energy [88]. ELBO is the crucial component that allows for joint optimization of variational parameters and model hyperparameters [88]. Since $\log\left(p(\mathbf{y})\right) = const$, minimization of KL divergence is equal to maximization of ELBO. This guides the approximation to match the true posterior distribution $p(\mathbf{f}\mathbf{f}_m|\mathbf{y})$ and the marginal likelihood $p(\mathbf{y})$. The variational distribution $q(\mathbf{f}\mathbf{f}_m|\mathbf{y})$ may be broken down to [88]:

$$q(\mathbf{f},\mathbf{f}_m|\mathbf{y}) = p(\mathbf{f},\mathbf{f}_m)q(\mathbf{f}_m,\mathbf{y}) \tag{2.38}$$

The inducing points in $q(\mathbf{f}_m,\mathbf{y})$ are treated as variational parameters, not as model parameters [85]. In order to obtain a tight ELBO the variational calculus allows us to find an optimal $q^*(\mathbf{f}_m,\mathbf{y})$ to remove the dependency of variational free energy on $q(\mathbf{f}_m,\mathbf{y})$ [85, 87, 88]:

$$F_q \leq F_{VFE} = \log\left(q_{DTC}(y)\right) - \frac{1}{2\sigma_\epsilon}Tr[\mathbf{V}_{nn}] \tag{2.39}$$

In this equation F_{VFE} is the collapsed F_q therefore VFE is often referred to as collapsed posterior sparse approximation in GP literature [83, 84, 88]. Yet again VFE may be referred to as variational DTC [85]. One may also notice that the only difference between the DTC approximation and VFE is the trace term $\frac{1}{2\sigma_\epsilon}Tr[\mathbf{V}_[nn]]$, that represents the total variance of predicting $\mathbf{f}$ given $\mathbf{f}_m$ [83, 84, 88]. Reduction of the trace term simultaneously maximizes F_q, in the extreme case when the trace term is zero $\mathbf{f} = \mathbf{f}_m$ and the full GP is recovered [85]. Therefore, the VFE approximation can only match the full GP and will never lead to overfitting compared to a full GP, as the trace term acts as regularizer [85]. Additionally, the trace term provides a suitable inducing set and always improves the ELBO estimation with increasing m [86]. Predictions obtained by VFE are smoother than predictions of a full GP model [88]. The VFE model approximates well the covariance structure of a full GP [84]. In comparison to the prior FITC approximation the VFE overestimates the noise variance while FITC underestimates it [83, 84]. When the ELBO is maximized, the hyperparameters of the model are regularized [88].

Due to KL mechanism in the variational formulation, the VFE always improves with additional inducing points whereas FITC may deteriorate as in the latter an inducing input may be in a nonoptimal location causing lower approximation quality. Both models are prone to unexpected behavior when inducing points are placed on top of each other [83]. Moreover the VFE approximation has a tendency to under-fit, although this is not a flaw of the model but rather of the optimization routine [83].

3

DATA-DRIVEN FRAMEWORK

UNDERSTANDING the influence of the various design parameters on the performance of the metamaterial is a nontrivial task, given the high dimensionality of the design space. Furthermore, the metamaterial undergoes buckling and post-buckling which are imperfection-sensitive phenomena. In order to tackle these issues, this work extends the data-driven framework proposed by Bessa et al. [76, 94] by investigating new machine learning methods that are capable of uncertainty quantification within high-dimensional spaces and large databases. In this work special emphasis is given to a new Bayesian machine learning method called Sparse Gaussian Processes, which enables predicting the response of the metamaterial for a large number of input design parameters while taking into account the imperfection-sensitivity of the properties of interest. The general framework consists of the steps outlined in Figure 3.1 and is discussed subsequently within the context of the proposed design.

3.1. PROPOSED METAMATERIAL CONCEPT

The considered unit cell design consists of two concentric rings joined by at least 3 longerons via barrel hinges, with D_1 and D_2 being respectively the bottom diameter and the top diameter of a given unit cell design. For the purpose of this study, the unit cell of the metamaterial is specified by the following set of material properties and geometric parameters:

1. The cross-section area of the longeron A
2. The Shear Modulus G
3. The Young's Modulus E
4. Second moment of inertia around x axis of the longeron cross section I_x.
5. Second moment of inertia around y axis of the longeron cross section I_y.

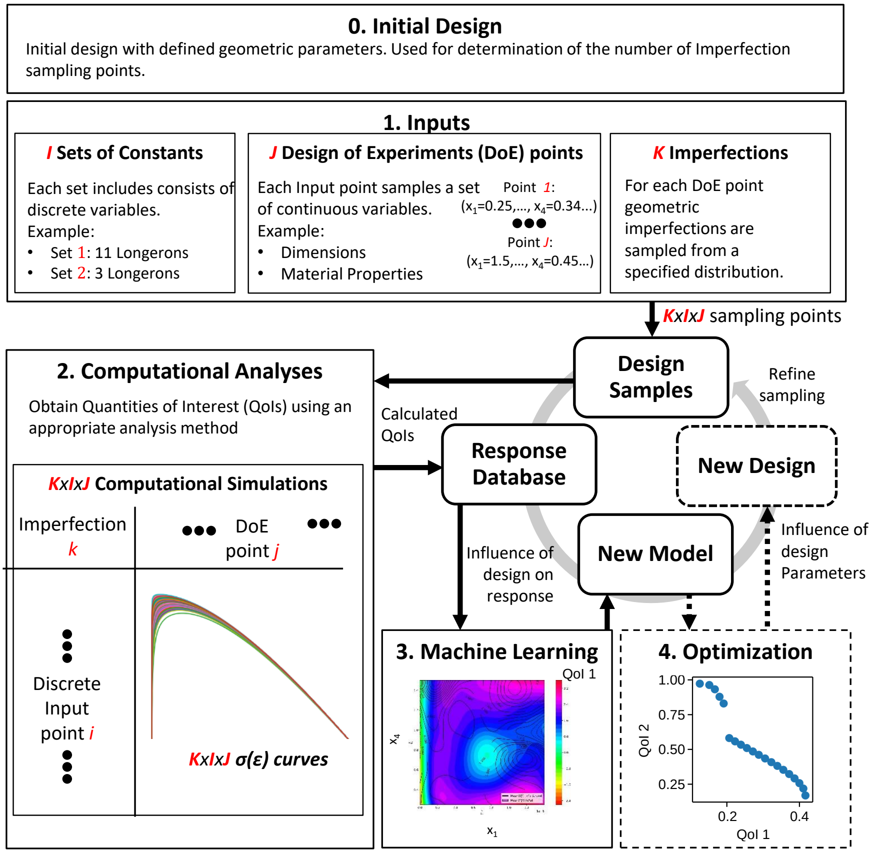

Figure 3.1: Schematic of data-driven framework (adapted from [94]).

6. The torsion constant of the longeron cross-section J_τ
7. Pitch (also referred to as Height) of the design P
8. The ratio of ring diameters D_R defined as: $D_R = \frac{D_1 - D_2}{D_1}$

The orientation of the longeron cross section, with some of the possible realistic cross sections and their characteristic dimensions is presented in Figure 3.2.

3.2. DESIGN OF EXPERIMENTS

This part of the framework has been modified to emphasize the role of modelling of imperfections in imperfection-sensitive applications. Due to ease of measurement and verification on experimental models, as well as dissimilarity between the first two buckling eigenvalues (second eigenvalue approximately twice the first), this work focuses on creating imperfections based on the first buckling mode of the structure when subjected

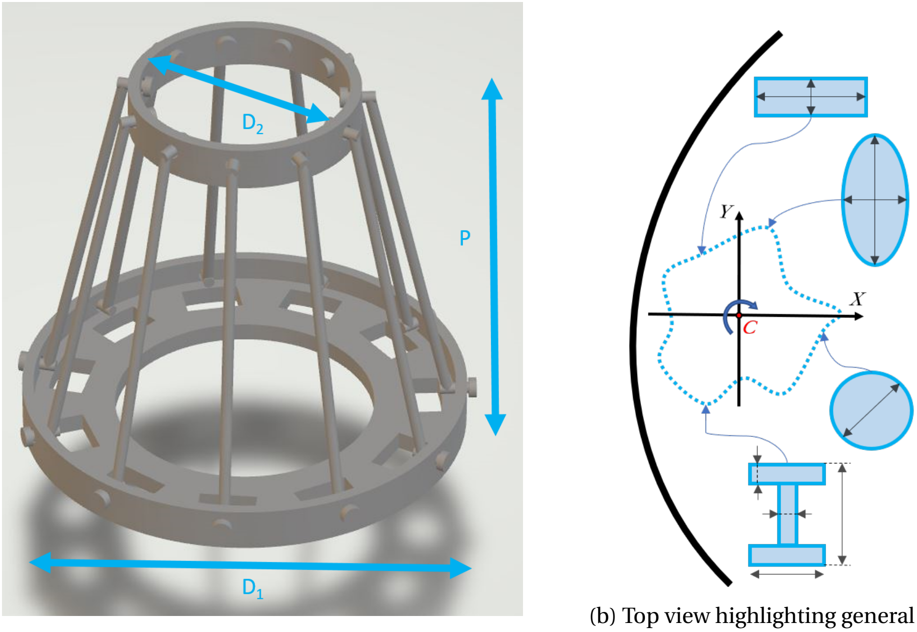

(a) Metamaterial concept.

(b) Top view highlighting general cross-section of longerons.

Figure 3.2: Metamaterial concept, highlighting the generality of the longerons' cross-section.

to a uniaxial compression load. All the Design Samples were generated using an in-house code implemented in MATLAB® [95].

3.2.1. CONSTANT VARIABLES

In the beginning, the Design of Experiments (DoE) [76, 94, 96] is carried out to sample the design space without prior awareness of the link between input variables and the output Quantities of Interest (QoI). The input space for of the metamaterial design is comprised of constants and continuous variables.

Throughout this work, a single set of constant parameters was used. These constants were:

1. The number of longerons set to 3;
2. The Young's modulus value $E = 1826$ MPa;
3. The bottom diameter of the design $D_1 = 100$ mm.

The number of longerons is constant due to the superposition principle in elasticity. As the longerons are the main load carrying component, increasing their number leads to a proportional increase of the resistant load of the structure. Recall that this is valid because the simulations do not model self-contact of longerons. However, if the number of longerons is large this assumption is not true after considerable deformation of the metamaterial.

The modulus of elasticity also remains unchanged in the DoE, since the goal is to analyze a recoverable energy absorber with linear elastic behavior of the base material. Therefore, the elastic constants act as linear scaling factors of the local deformation, not adding information to the mechanical response. The value of the base diameter D_1 is also kept constant because every geometric dimension of the structure is defined relative to D_1.

3.2.2. CONTINUOUS VARIABLES

For the set of constant parameters, a specified number of DoE points J was generated. The bounds of the DoE were selected for validation purposes to incorporate the bounds of a pre-existing response database, created exclusively for the circular longeron cross section. The bounds for the seven continuous variables are presented in Table 3.1.

Table 3.1: Bounds of continuous input variables for every point.

Variable	A [mm^4]	G/E	I_x [mm^4]	I_y [mm^4]	J_τ [mm^4]	P [mm]	D_R
Lower Bound	0.1171	0.335	0.011	0.011	0.0014	25	0.0
Upper Bound	40.96	0.45	140	140	676.7	150	0.8

Similarly to the diameter ratio D_R , the parameters describing the longeron cross-section and the height of the design were normalized by the bottom diameter $D_1 = 100$ mm. This normalization allows the response database to be applicable to an arbitrary longeron cross section. Ultimately, the bounds for DoE points J are presented in Table 3.2. These bounds have been used for generating all the databases and experiments in this work.

Table 3.2: Normalized bounds for Design of Experiments points J.

Variable	A/D_1^4	G/E	I_x/D_1^4	I_y/D_1^4	J_τ/D_1^4	P/D_1	D_R
Lower Bound	1.17E-5	0.335	1.128E-11	1.128E-11	1.353E-11	0.25	0.0
Upper Bound	4.1E-03	0.45	1.4E-6	1.4E-6	7.77E-6	1.5	0.8

Once the design variables and their bounds are established, the design space needs to be sampled accordingly [96]. Without the assumption of any preceding knowledge of the problem to be solved or between input and output information, space-filling designs that treat distinctive regions of input space commensurately are particularly suitable [96]. In accordance with past investigations [76, 94] the Sobol [97] sequence is used also in this work, as it offers a fair balance between regularity and randomness as well as eases the Machine Learning process later [96]. The effect of using the Sobol sequence for sampling on three arbitrary design variables is presented in Figure 3.3. The core advantage of using this technique is that even with low number of sampling points the input space is well characterized, increasing the number of following sampling points leads to higher quality of input space characterization. This effect is especially desirable if one is to characterize a high dimensional input space using a relatively low number of DoE sampling points [76, 98]. Using this approach, unique DoE points were created, each corresponding to a different unit cell design.

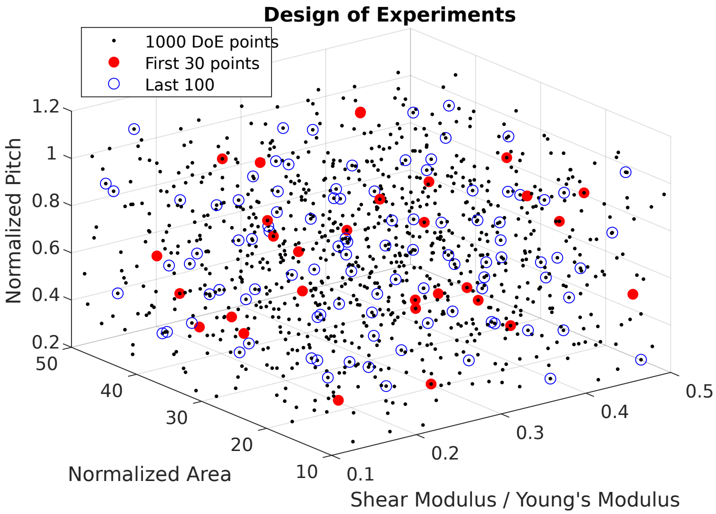

Figure 3.3: Illustration of the Sobol sequence sampling scheme used in the Design of Experiments.

3.3. FINITE ELEMENT ANALYSIS

In this work a similar approach to Bessa et al. [94] has been adopted for the computational analyses. Each metamaterial design (each design of experiments point) needs to be simulated with the finite element method to predict the quantities of interest (buckling load and energy absorption). In order to predict buckling and postbuckling of these structures, the finite element analyses need to be conducted in two steps:

1. Linear buckling analysis of a given design in the undeformed state: providing an estimate of the buckling loads and modes – eigenvalues and eigenmodes, respectively. If the behavior prior to buckling is nonlinear, then the predicted buckling load is just an approximation.

2. Implicit static simulation using the arc-length method: from the results of the linear buckling simulations, one or more buckling modes can be used to create geometric imperfections in order to resolve the bifurcation of the response according to the arc length method (RIKS analysis) [99].

As previously mentioned, the deformation process of the proposed metamaterial is unstable (buckling), implying that the response is imperfection sensitive. Geometric imperfections depend on the manufacturing process and are laborious to characterize.

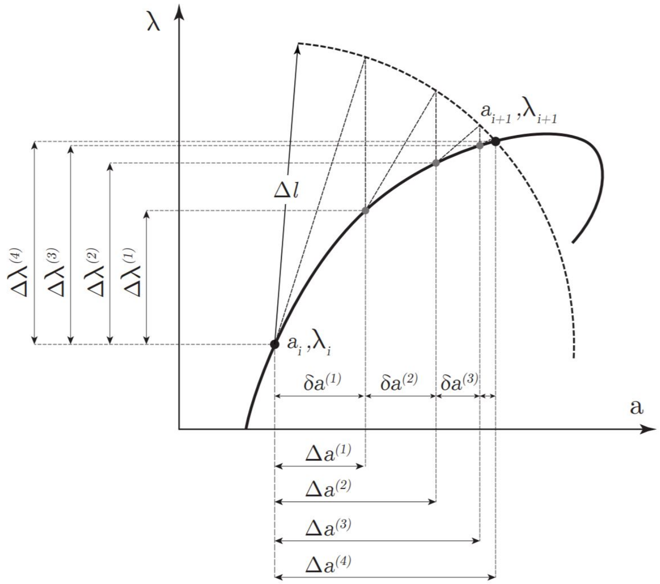

Figure 3.4: A schematic of RIKS analysis iterations, where a is the normalized displacement and λ is the load increment. The increment is defined by the radius of the circle Δl, and the next point is the point of intersection between the path and the circle [100].

Here, we followed the well-established procedure [94, 99, 101] of creating geometric imperfections based on the first buckling mode, so that the RIKS analysis can then be conducted to obtain the complete mechanical response of the metamaterial.

3.3.1. GEOMETRIC IMPERFECTIONS FOR RIKS ANALYSIS

Buckling and post-buckling of a structure depend on the presence of geometric imperfections [94, 99, 101]. These imperfections are often stochastic (material defects, geometric defects, variations in boundary conditions, etc.) and their impact on the structure response is unknown *a priori*. Therefore, quantifying the uncertainty caused by the imperfections on the quantities of interest is critically important for the analysis and design of the metamaterial.

In addition, each design has different imperfection sensitivity. Hence, uncertainty quantification is required for the whole design space [94]. As mentioned, geometric imperfections can be mod-

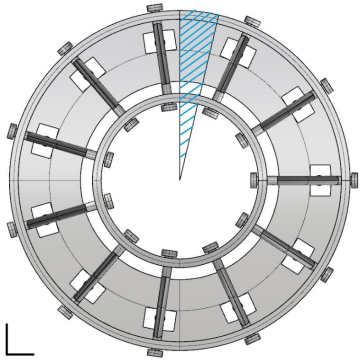

Figure 3.5: Top view of the design with schematic illustration of mode 1 buckling imperfection as angle θ.

eled by using the first buckling mode multiplied by a chosen amplitude to perturb the initial (undeformed) geometry of the design prototypes. Preliminary experimental work conducted by Houlder and Bessa (MS thesis, to appear 2019), identified that the most significant geometric imperfection coincided with the first buckling mode. This is explained by the hole-pin tolerance of the longeron hinges connecting them to the bottom and top bases, leading to a clear deviation of the undeformed geometry from perfectly vertical longerons – see Figure 3.5. Therefore, only the first buckling mode was selected for seeding these imperfections.

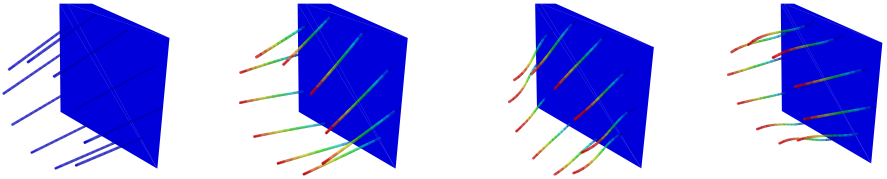
(a) Undeformed. (b) Buckling mode 1. (c) Buckling mode 2. (d) Buckling mode 3.

Figure 3.6: Undeformed metamaterial and first three buckling modes.

Unsurprisingly, different physical realizations of the *same* idealized design will deviate differently from this idealization due to the stochastic nature of the manufacturing process and the environmental conditions. Therefore, the amplitude of the first buckling mode is not deterministic; it follows a statistical distribution. Accurate determination of this distribution involves a large number of experiments for *each* design, which is not practical to do. Instead, Houlder and Bessa selected a nearly optimal design for a prototype with circular cross-section longerons and inspected the amplitude of these deviations – see Table 3.3 and Figure 3.7 that specify that design. Figure 3.7 explains this elementary design where the parameters A, I_x, I_y, and J_τ, can be replaced by a single parameter – the longeron's diameter d.

Table 3.3: Dimensions of the metamaterial unit cell used to characterize the imperfection amplitude.

Height P	Bottom Diameter D_1	Top Diameter D_2	Number of Longerons	Diameter Ratio D_R	Longeron Diameter d
66.0 mm	100.0 mm	80.0 mm	10	0.2	1.68 mm

As seen in Figure 3.5, the amplitudes of the first buckling mode were measured by determining the rotation angle around the Z axis when the structure is at rest, as compared to when the bases are perfectly aligned (idealized geometry). Fourteen prototypes were measured in total, and the results were used to determine the statistical distribution of imperfections. Details about the experimental work fall outside the scope of this thesis (see Houlder, MS thesis, to appear in 2019). The arithmetic mean of the measured rotation angle was 2.0° with the standard deviation of 1.2°. However, we determined that

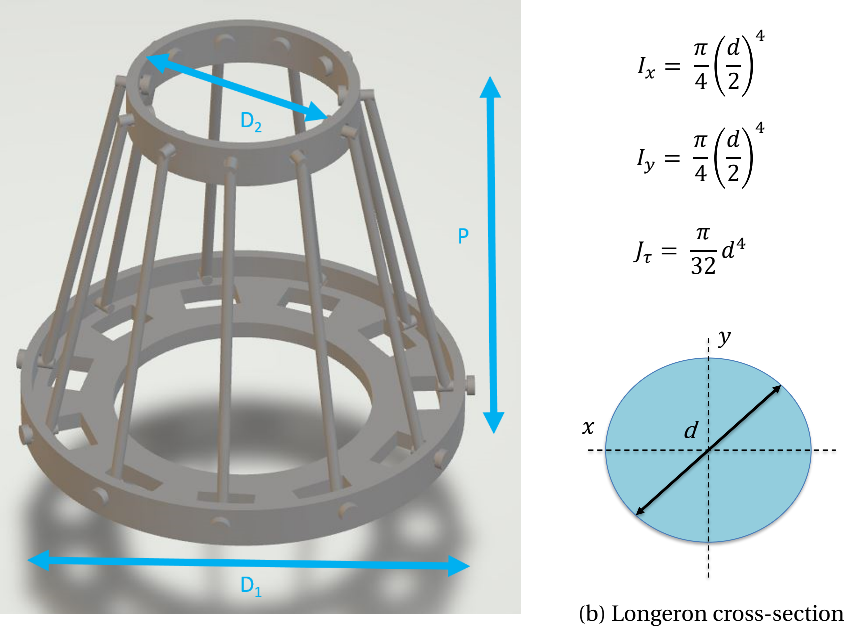

(a) Metamaterial with circular longerons.

(b) Longeron cross-section for this design.

Figure 3.7: Metamaterial design used for characterizing imperfection sensitivity. Table 3.3 shows the geometric parameters of this design.

a conservative approach of doubling the mean value of the distribution, i.e. an average rotation angle of 4.0°, would improve correlation with experimental results. Effectively, we determined the equivalent amplitude for the first buckling mode that simulates the influence of all other imperfections observed experimentally.

The number of experimental measurements conducted by Houlder and Bessa is not enough to determine accurately the statistical distribution of the imperfection amplitude (angle of rotation). Therefore, a reasonable assumption is needed. The distribution was assumed to be Lognormal, since it is expected that the real distribution is skewed, i.e. the angles measured should be closer to 0° (ideal geometry) than to large values (> 10°) which creates a long tail to the right of the distribution. The assumed distribution type and respective statistical moments[1] were used to generate samples for each design via UQLab™ [102], as this module was integrated in the data-driven framework. Latin Hypercube Sampling method [103, 104] was applied to generate near-random sample from the imperfection amplitude distribution.

In addition, note that each design was assumed to have the same distribution for the imperfection amplitude. Despite the imperfection amplitude being sampled from the same distribution, the actual imperfect geometries are not necessarily the same because the first buckling mode is not the same for every design. In summary, lognormally dis-

---

[1] In this context statistical moments refer to the mean and the standard deviation of the statistical distribution.

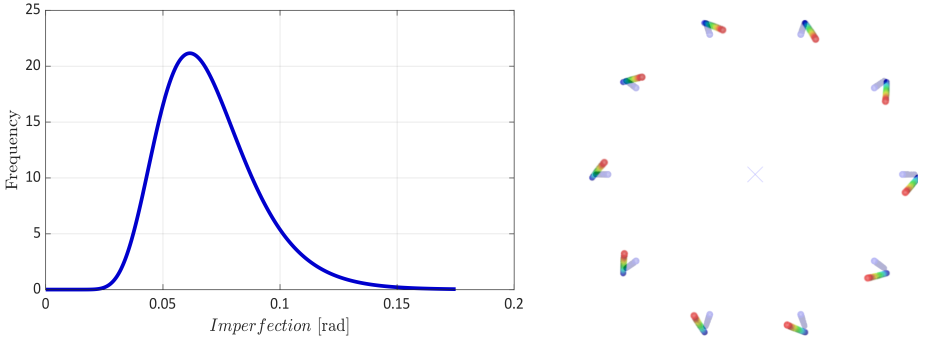

(a) Assumed lognormal distribution of imperfections for each design. Mean amplitude is 4.0° (0.07 rad).

(b) Example with 4.0° imperfection amplitude.

Figure 3.8: Imperfect geometry of the metamaterial is obtained from (a) Lognormal distribution for the amplitude of the 1st buckling mode; and (b) an example for an amplitude of 4.0°

tributed mode-1 imperfections with mean of 4.0° and standard deviation of 1.2°, Figure 3.8, were assumed for every DoE point of the seven-dimensional space.

IMPERFECTION SENSITIVITY OF A SINGLE DESIGN

Looking at Figure 3.9, as expected all the force-displacement curves resemble the same behavior. The fitted probability density functions are presented in Figure 3.10. The difference between the maximal and the minimal QoI of a single design is on the order of 25%. Under closer inspection, while the probability density function for buckling values may be described as uniform, the probability density function for energy is non-uniform, with a pronounced lack of values for the bin representing values between 31.6-31.8. Anomalous behavior is also visible for values 32.4-32.8. The second kink seems to be a result of how boundaries between the bins are established. The first kink is confirmed by generating and analyzing force strain curves for a design with different geometry and material constants. It is also visible at half the sampling points and twice the number of sampling points. This may indicate that there exists a dual distribution for the energy.

Table 3.4: Chi-squared and KS test results for the fitted distributions.

	Critical buckling load		Energy Absorbed	
Distribution	χ^2	KS	χ^2	KS
JohnsonSu	1.85480	0.99976	41.2826	0.03165
Loggamma	2.67262	0.99841	41.2241	0.02523
Gumbel L	31.3269	0.52345	38.3714	0.06026
Normal	119.000	0.00895	272.863	0.00002

The χ^2 and KS test metrics are summarized in Table 3.4. The presumption of dual distri-

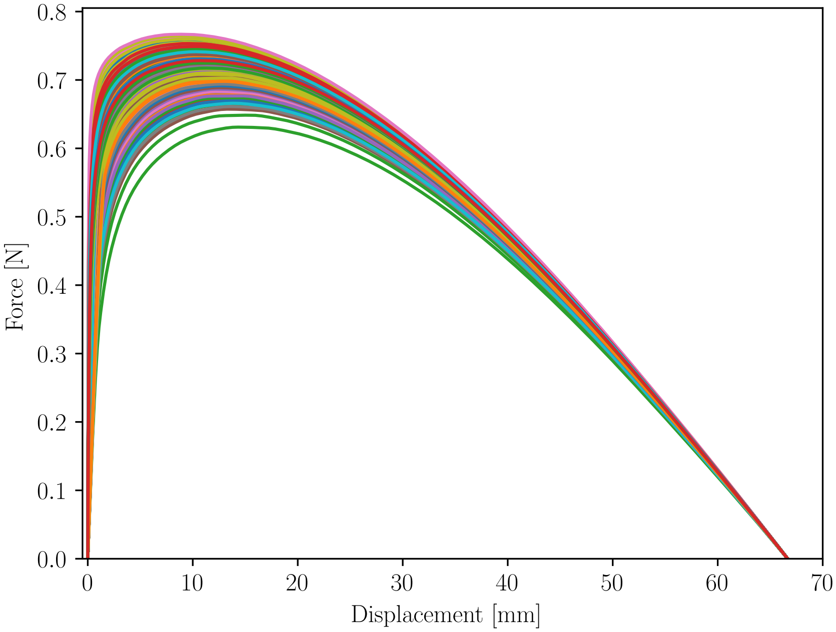

Figure 3.9: Every imperfect force-displacement response for the design in Table 3.3 considering 1024 realizations with different imperfections.

bution is reflected in the low KS test values for $E_{absorbed}$. Only the Gumbel distribution passes the statistical significance threshold of 0.05. This may confirm the energy values are non-uniformly distributed, but the χ^2 values indicate that one may approximate energy values with a single distribution. The values of KS for critical buckling are significantly higher than the 0.05 threshold, except for the normal distribution. The KS values for JohnsonSu and Loggamma distributions are close to unity, which means that the shape of true probability distribution function (PDF) is well captured by these distributions. The Gumbel distribution has a 15-fold higher χ^2 value, with KS being approximately 50% lower. The normal distribution has a significantly higher chi-squared result, with the KS metric being below the statistical significance threshold. This is confirmed by examining Figure 3.10, where the bell-shape of normal distribution is a worse fit than the remaining three distributions.

The final values for the mean and standard deviation of $E_{absorbed}$ were similar for each of the considered distributions with the value of approximately 32.27 ± 0.8 [Nmm]. Further information and plots are available in Appendix A.

The loggamma distribution seems to be a reasonable choice for both QoIs as indicated by the histograms and the metrics. However, as the standard deviation is relatively low

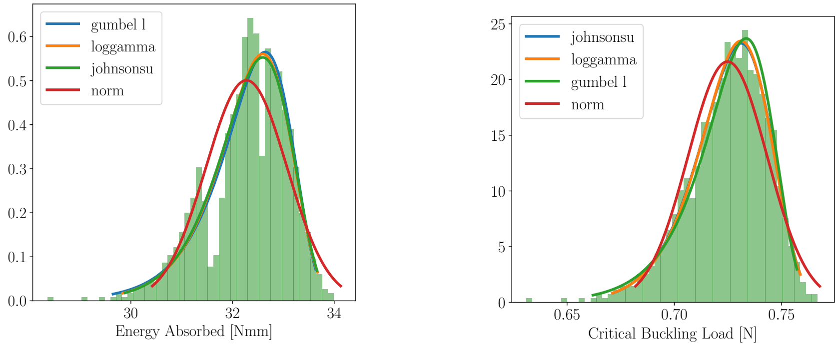

(a) $E_{absorbed}$

(b) $P_{critical}$

Figure 3.10: Histograms with overlaid fitted probability density functions for both quantities of interest. Bell curve presented for comparison.

in comparison to the mean value, it is not unreasonable to assume the Gaussian distribution for imperfections. Moreover, Bayesian Machine Learning assuming a Gaussian Distribution involves a significantly less computational resources when assuming a normal distribution because any other distribution would require the use of Monte Carlo sampling (dramatically decreasing computational efficiency).

3.3.2. POST-BUCKLING ANALYSIS WITH ARC-LENGTH METHOD

The arc-length method is used to track structural responses with negative stiffness, i.e. capturing snap-back and snap-through instabilities [100]. This method surpasses the convergence issues observed when using the Newton's method to solve the finite element equations. As described above, the first buckling mode is augmented by an amplitude obtained from sampling the chosen imperfection distribution. Then, the idealized geometry of the metamaterial is perturbed according to this mode in order to start the post-buckling analysis with an undeformed configuration that will not diverge at the bifurcation point due to the presence of the geometric imperfection. This allows to characterization the complete response of the metamaterial design.

A schematic representation of the arc-length method (commonly referred as RIKS analysis) is presented in 3.4. The original Riks paper [99] and a review by Nikolaos [100]. provide an excellent source of further information on the method. Our finite element analysis has, however, a few important simplifications to keep in mind:

- The friction for the barrel hinges that connect longerons with support rings is neglected by the simulations. This effect can be minimized by reducing roughness between the barrel and the pin. In real life experiments it was observed that this friction may cause jamming of the pins, particularly at fast applied loads, that lead to sudden peak force and higher critical buckling load;

- Defining a generalized section in terms of A, I_x, I_y, and J, implied performing the cross-section integration before the analysis rather than during. Therefore, the force-displacement vectors that allowed to calculate the global strain were readily available, however the local strains and stresses across the cross-section of the longerons (along the length of P) were unavailable.
- Since machine learning requires large datasets to create accurate models and the number of Abaqus licenses available was limited, self-contact between the longerons was not modeled due to the significant computational time that would be added per simulation (each data point would require too much time to generate a large enough database, as discussed next in the machine learning section). It is intuitive that increasing the number of longerons in the design leads to higher buckling loads, however this comes at a cost of decreasing the total compressive displacement allowed by the design, as the longerons may overlap. This is important for energy absorption considerations as most probably designs with highest buckling loads will not coincide with the designs with highest energy absorption due to a shorter coiling path.

Self-contact is an important influencing factor in finding the best design when the number of longerons is sufficiently high. However, the impact of this effect was mitigated by fixing the number of longerons and the value of D_1. Priority has been given to the applicability of the database to any cross section as long as it is closed and the shear center lies on the axis of symmetry for a given cross section [105, 106]. The results of simulations are stored in a database that is later used to extract QoIs.

The procedure for calculating $E_{absorbed}$ as the area under the stress stress-strain curve of the metamaterial is as follows:

(a) For each considered output point append the vectors of forces and displacements from RIKS analysis;

(b) Convert force and displacement vectors to effective stress-strain vectors considering the pitch of the design and D_1;

(c) Reject the stress-strain curves that fail to reach 80% strain, as they represent simulations with incomplete deformation of the metamaterial;

(d) Using a Piecewise Cubic Hermite Interpolating Polynomial (PCHIP) [107] interpolator, interpolate the output vectors of stress and strain to obtain a continuous response of the metamaterial;

(e) Generate a new vector of 10000 evenly spaced strain values between 0.0 and 1.0;

(f) Use the interpolator object on the newly generated vector from point (c) to obtain a vector of stress values of same length;

(g) Apply Simpsons rule [108] to calculate the area under the newly generated stress-strain curve;

(h) Append $E_{absorbed}$ and $P_{critical}$ for every design to a single list for all designs.

Note that the height reduction of the structure due to the introduced geometric imperfection is considered negligible.

3.4. BAYESIAN MACHINE LEARNING

The design of an unstable metamaterial with a large number of parameters poses significant challenges to the machine learning process because it requires large databases and uncertainty quantification. Currently, as revised in Chapter 2, few methods satisfy these requirements. Therefore, a detailed comparative study of recently proposed sparse Gaussian Processes is reported in Appendix B. This comparison was conducted for both regression and classification, including well-established machine learning algorithms to provide a benchmark – artificial neural networks and support vector machines, respectively.

The comparative study revealed that the SGPR algorithm led to more accurate results for regression, whereas the SVGP algorithm was a better classifier even when compared to conventional GPs or SVC for same dataset size, see Figure 3.12. This was explained by differing approximations of the non-gaussian posterior in the presented algorithms.

As expected the quality of the machine learning models increased with the amount of available data. It was clear that the neural network algorithm achieved lower mean square error as compared to GP algorithms, see Figure 3.11. This may be related to the selection of the $Matern52$ kernel for the gaussian processes. Moreover, note that standard neural networks do not provide the confidence intervals for the mean function and the difference between sparse GP and neural networks indicated over-fitting issue for the latter.

In summary, the metamaterial analysis through machine learning is provided by the SGPR method for regression and SVGP for classification of design space. A detailed comparison of these and other machine learning models is included in Appendix B.

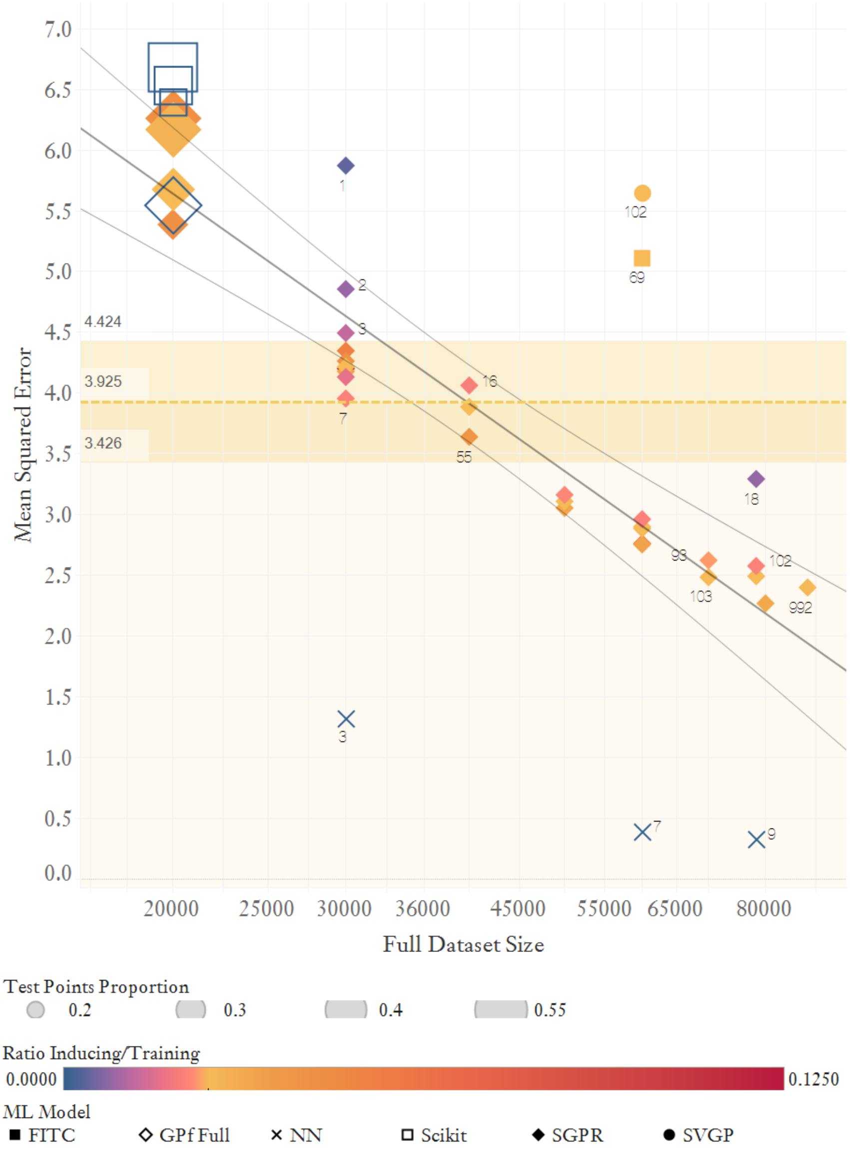

Figure 3.11: Mean squared error of regression as function of dataset size. The dashed yellow line indicates the average MSE with 95% confidence intervals for all runs, the grey line for the logarithmic trendline, numbers above labels indicate the time to train the model in minutes.

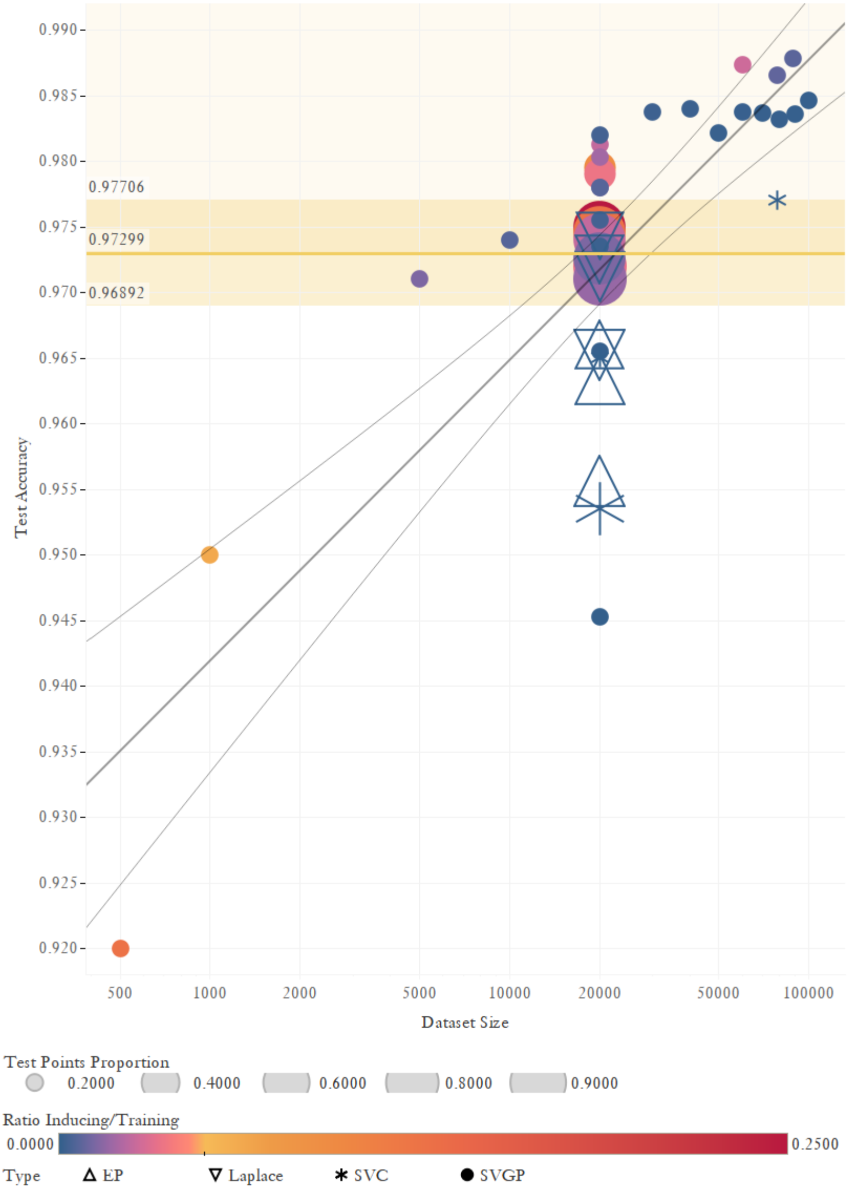

Figure 3.12: Classification Test accuracy as function of dataset size, yellow line represents the average accuracy with 95% confidence intervals for all runs, grey line for logarithmic trendline.

4

METAMATERIAL ANALYSIS WITH DATA-DRIVEN FRAMEWORK

CHAPTER 3 carefully justifies the choices for the design of experiments, finite element simulations, and Bayesian machine learning methods suggested for analyzing the metamaterial concept with the data-driven framework. The current chapter focuses on the analysis using this framework, enabled by machine learning and sensitivity analysis. Section 4.1 introduces the best designs as determined from the DoE sequence. The influence of design parameters was mapped using the machine learning model in section 4.2. Results of global sensitivity analysis based on the machine learning model are presented in section 4.3. Verification of the trends and insights derived in this chapter is provided in 4.4.

First, a database spanning the design space was used to classify metamaterials into two classes: coilable and non-coilable. Then, the machine learning regression process is performed only on coilable designs, since the remaining ones are of no interest to this work. The same sub-set of points is used to perform regression for both the critical buckling load and energy absorbed. In this case, results of the RIKS analysis are necessary to obtain stress-strain curves that are used to calculate the energy absorbed. Once the machine learning regression model is obtained, a sensitivity analysis is conducted to gain insight on the influence of the design parameters on the quantities of interest. Each metamaterial design was perturbed according to the first buckling mode to create an imperfect geometry simulating manufacturing imperfections, as previously discussed. The imperfection amplitude is extracted from Lognormal distribution with mean of 4^o and standard deviation of 1.2^o using a pseudo-random number generator. The first 40 000 points in the sequence were simulated only using the linear buckling analysis to speed up computations. The response database was used to train a SVGP classifier with 800 inducing points and accuracy of 0.98, that was used to exclude non-coilable designs from the entire DoE sequence. The author acknowledges that by doing this we no longer have a complete Sobol sequence, i.e. the classified sequence no longer corresponds to the space-filling order of the initial DoE sequence. This has implications when conducting the sensitivity analysis, as it was required to sample points from the model rather than directly from the simulation results. However, due to the need of using computational resources efficiently, it would be wasteful to conduct simulations for points that will not lead to coilable designs.

Following this procedure, the first 115 000 points from the classified DoE were simulated using both linear buckling analysis and the RIKS analysis. Subsequently, the process outlined in Section XX was implemented to obtain the values for $P_{critical}$ and $E_{absorbed}$. After applying the procedure for calculating area under stress strain curves, 59991 points were available to train the models.

Two separate machine learning models were created, one for the $P_{critical}$ and one for the $E_{absorbed}$. In each case the input points for the model were scaled using the same standard scaler, and subsequently split into train and test set, 80% of the points were used for training and 20% for testing. Subsequently, the models were trained using the SGPR algorithm with Matern 5-2 kernel and ARD, 1200 inducing points were enough to achieve high quality predictors.

The regression models of critical buckling load $P_{critical}$ and energy absorption $E_{absorbed}$ were then used along with the classification model to create projections of design space, contour maps, that allowed to visualize the influence of design parameters on the quantities of interest.

4.1. BEST DESIGNS FROM THE DESIGN OF EXPERIMENTS

As nearly 60000 points were simulated from the DoE sequence, it was possible determine designs close to optima directly from the response database. The stress-strain curves of designs with maximum $P_{critical}$ and $E_{absorbed}$, obtained directly from the simulations are presented in Figure 4.1. The top stress-strain curve for $P_{critical}$ had, as reported by static buckling analysis, critical buckling load of 88 kPa and energy absorption value of 14 kJ/m^3. The energy absorption has been calculated in this case assuming the tensile stresses to be zero. One can also observe a discrepancy between $P_{critical}$ value and the peak of the stress-strain curve generated by RIKS analysis. This difference is relatively substantial yet consistent for designs that had high reported $P_{critical}$ value (> 80 kPa). Throughout this work, the values as reported by static buckling analysis are assumed. The design for $E_{absorbed}$ achieved critical buckling load of 33 kPa and energy absorption of 54 kJ/m^3. The corresponding design parameters for stress-strain curves depicted in Figure 4.1 are presented in Table 4.1.

Analyzing the design parameters in Table 4.1, the values G/E are comparable which implies a low Poisson ratio for both designs. The difference in area and height is noticeable but not drastic, shorter designs tend to buckle in a more stable way, as the longeron becomes longer the first two eigenvalues become closer and bending may be triggered. The values of I_x and I_y are at the top range values for respectively $P_{critical}$ and $E_{absorbed}$, which suggests that these parameters are crucial in achieving optimal values of quanti-

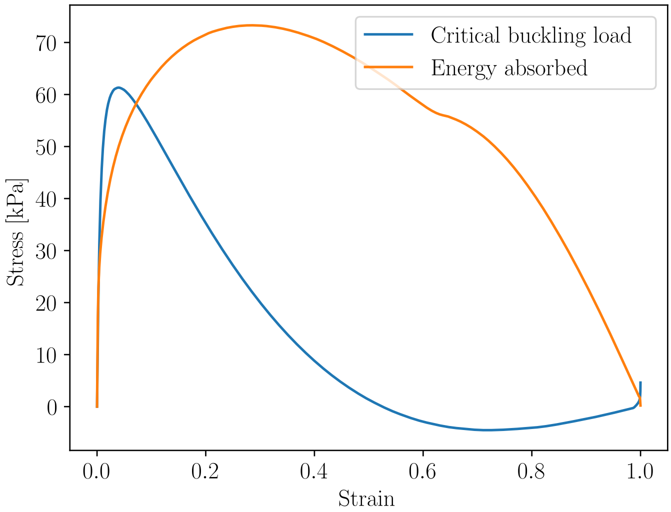

Figure 4.1: Comparison of the stress-strain curves for highest energy absorbed and critical buckling load obtained from the simulations.

Table 4.1: Corresponding design parameters for the curves presented in Figure 4.1.

Dataset	A [mm^2]	G/E	I_x [mm^4]	I_y [mm^4]	J_τ [mm^4]	P [mm]	D_R
$\max(P_{critical})$	26.0	0.439	137.1	91.0	647.7	47	0.14
$\max(E_{absorbed})$	38.0	0.430	119.1	139.3	58.2	70	0.78

ties of interest. Significant differences exist for values of J_τ and D_R. This result indicates that to obtain optimal buckling loads high torsion constant and low D_R is necessary. Conversely, to attain top energy absorption capabilities, relatively low torsion constant as well as a significantly smaller value of D_2 relative to D_1 is required.

The onset of tensile stresses visible for the best $P_{critical}$ design in Figure 4.1 is presented in Figure 4.2. This may suggest the discussed bi-stable behavior, with certain amount of force required for snap-through. For similar designs where the value of I_y and I_x were within the same order of magnitude the region with low tensile stresses disappeared. This region may be a numerical artifact and experimental validation is required. Note that these tensile stresses are negligibly small and that they are observed for a few designs with extreme input parameters.

As a sliding contact and self-contact between the longerons and the base was not implemented due to computational expense and convergence issues, some simulations show kinks in the stress-strain curves which correspond to a second contact event of the longerons with the base. These events have been marked by arrows in Figure 4.3,

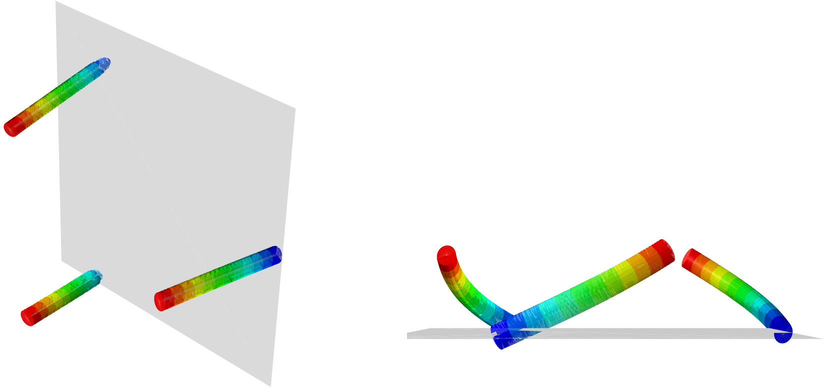

(a) Undeformed design. (b) Deformed design at 0.6 global strain.

Figure 4.2: The best design for critical buckling $P_{critical}$ of all DoE points analyzed.

and they were also observed experimentally, as seen in Houlder's dissertation (to appear, 2019).

Note that by declaring a generalized cross-section for the longerons it was not possible to predict the local strains across the cross-section of the longerons (only the average strains are available). In addition, using a general cross-section enforces performing the section integration before the computational analysis rather than during. Having access to the local strains and stresses in the longerons would allow to determine whether the structure undergoes plasticity or even fracture, i.e. if the local deformation exceeds the elastic regime. This would be crucial for the final optimization of the design, since it limits the possible designs significantly due to failure by exceeding yield strength of the substrate material. Yet, this was a sensible compromise made to gain insight into other parameters of the structure. Thus, the manufacturability of the presented designs shall depend on the choice of substrate material.

The results of simulations show that it is possible to significantly modify the mechanical response of the design by tuning certain parameters. However, we want to know how this response changes and which parameters are most critical for the unit cell design. This warrants further analysis and creation of machine learning models to gain more insight from the available data.

4.2. DESIGN CHARTS AS CONTOUR PLOTS

After creating the machine learning model, projecting the design space becomes possible and we can create contour maps that help when visualizing high-dimensional spaces. In this work we simplified this visualization by simple 2D projections onto two varying features while keeping the remaining constant. It was generally found that the machine learning models achieved higher performance by training on coilable designs alone. As an example, a SGPR model for $P_{critical}$ with ratio of inducing to training points of

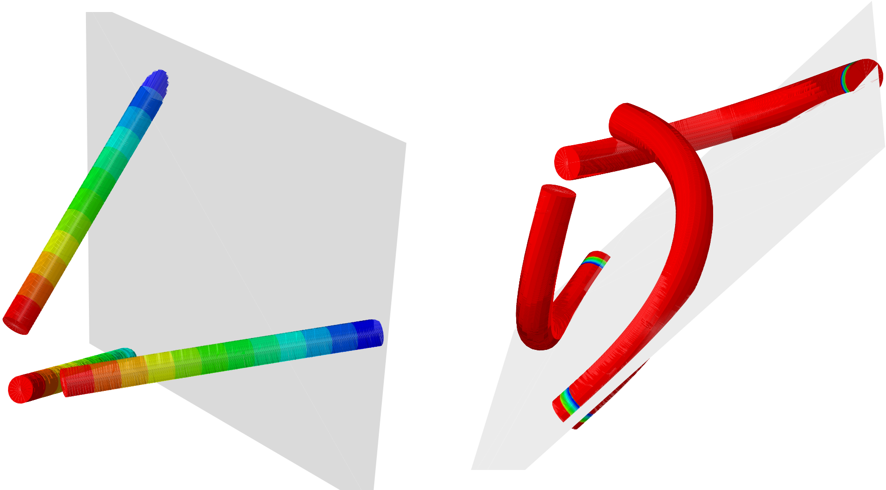

(a) Undeformed design.

(b) Deformed design when 2nd contact happens.

Figure 4.3: The best design for energy absorbed $E_{absorbed}$ of all DoE points analyzed.

0.025 trained on a 60000 point dataset achieved a $\mathscr{R}^2 = 0.999$ when trained only on coilable designs, whereas for all the designs and same model parameters the $\mathscr{R}^2$ was 0.992. This showed that exclusion of non-coilable designs resulted in a more consistent dataset.

A good performance of the classifier on the seven-dimensional space was confirmed, as out of 103001 points generated via simulations, 1269 points were misclassified. This corresponds to the accuracy close to that reported by the classifier of 0.987 and ultimately validates the performance of the classification model.

Together with the criterion of only considering metamaterial designs for which the simulations achieved above 80% global deformation, which excluded incomplete simulations, the final $\mathscr{R}^2$ values for regression of $P_{critical}$ and $E_{absorbed}$ were respectively 1.00 and 0.992. The length scales of SGPR models, as determined by kernel ARD, for every design parameter are presented in Table 4.2. The standard deviation of the mean was heteroscedastic in nature, i.e. it varied in space, and it did not exceed 2 kPa for the stresses and 3 kJ/m^3 for the energy.

Table 4.2: ARD regression model length scale for each of the design parameters.

QoI	A/D_1	G/E	I_x/D_1	I_y/D_1	J_τ/D_1	P/D_1	D_R
$P_{critical}$	37.0	34.0	2.4	127	2.7	4.2	3.6
$E_{absorbed}$	27.0	15.0	2.8	7.4	2.5	3.8	6.6

For both quantities of interest the ARD regression model indicates that the parameters

A/D_1 and G/E are less important than others, as seen by a large value for the length scale – see Table 4.2. This result suggests that the correlation of these two features and the quantities of interest is limited in comparison to other design parameters. This was confirmed by comparing projections of the design space with low and high values of these two features, the magnitude and distribution of the quantities of interest changed insignificantly. Moreover, the length scale of 127 obtained for the case of the critical buckling load, $P_{critical}$, suggests that it is invariant to I_y/D_1. The remaining design parameters had relatively similar length scales for both quantities of interest, $P_{critical}$ and $E_{absorbed}$, suggesting that they are significantly important to the behavior of the metamaterial. This is confirmed by observing Figures 4.4, 4.5 and 4.6.

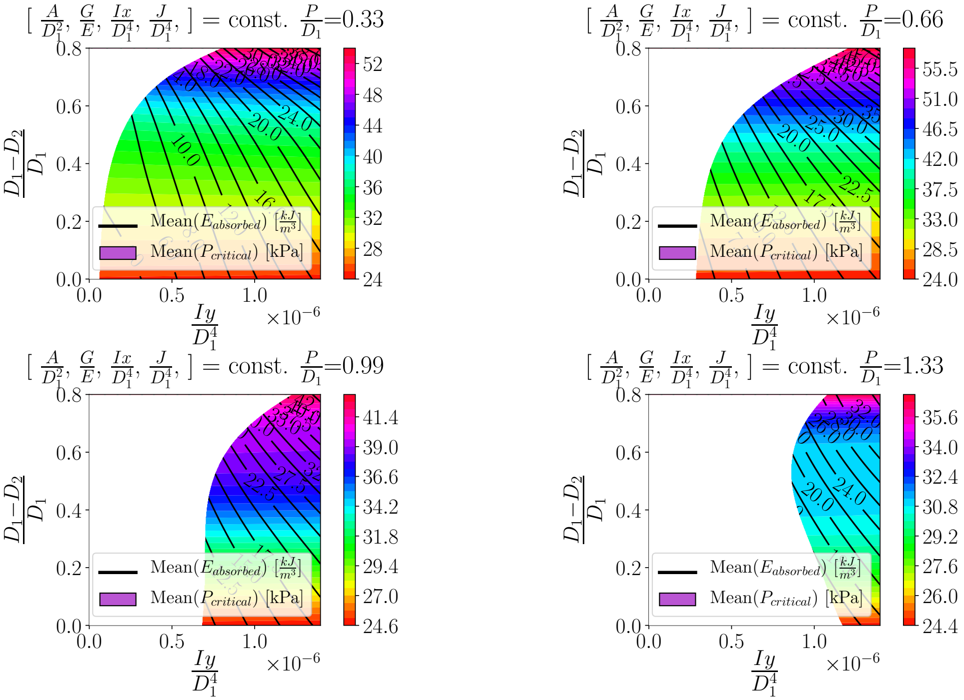

Figure 4.4: Mean quantities of interest as function of I_y , D_R and P. The normalized parameters A=0.001, G/E=0.36, $I_x = 7.5\times10^{-7}$, and $J_\tau = 2.5\times10^{-6}$ remain constant.

Looking at Figure 4.4, one may observe a strong correlation of both $P_{critical}$ and $E_{absorbed}$ with increasing I_y and D_R. Whereas $P_{critical}$ seems to be largely invariant to I_y ,as one does not witness a significant change in values along the horizontal axis, $E_{absorbed}$ values grow at approximately 45^o angle, to reach top values in the upper right corner. This shows strong correlation to both I_y and D_R . Comparing the four subplots, the highest values for both quantities of interest are achieved for subplot with P/D_1 value of 0.66. Additionally, as height of the structure grows, less area of the plot is classified as coilable. This is intuitive to understand, as the metamaterial height increases the bending stiffness decreases which starts favoring a bending deformation mode instead of a coilable one. This is translated by an approximation of the first and second buckling eigenvalues as the height increases (first eigenmode is the coilable one and second is in bending, until this is reversed and the first becomes in bending, hence classifying these designs as non-coilable).

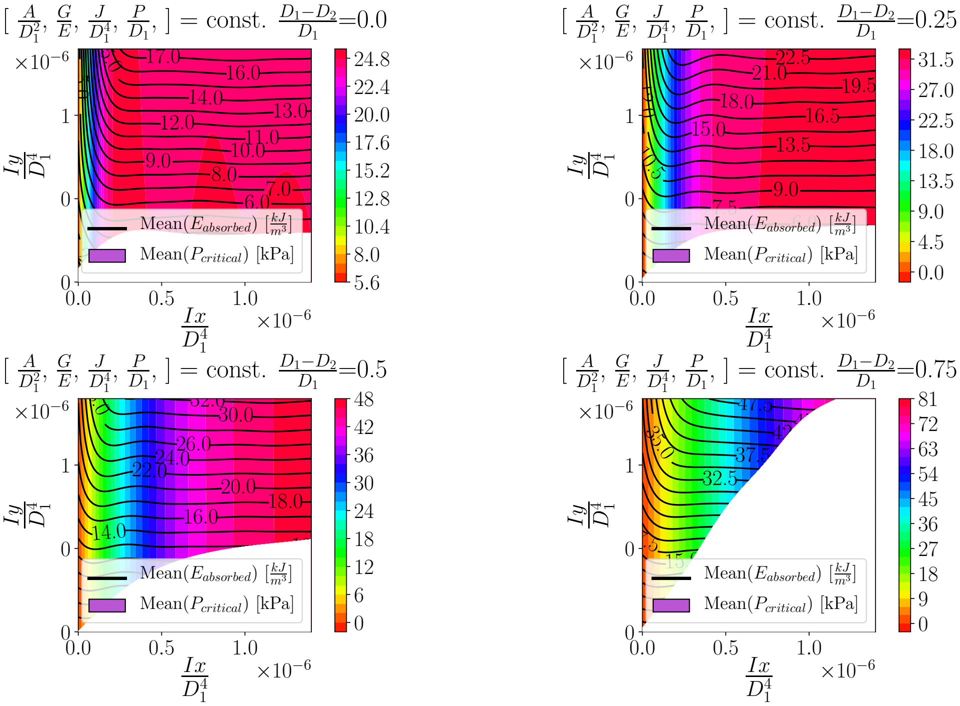

Figure 4.5: Mean quantities of interest as function of I_x, I_y, and D_R. The A=0.001, G/E=0.36, $J_\tau = 2.5 \times 10^{-6}$ and P=0.66 remain constant.

The influence of second moments of area is presented in Figure 4.5. The primary remark is that the contour lines of $P_{critical}$ and $E_{absorbed}$ are virtually perpendicular to one another. The values of $E_{absorbed}$ are largely independent of I_x above 2.5×10^{-7} . For the subplot wit D_R =0.0 one can see a sharp increase in critical load values at $I_x = 2 \times 10^{-7}$ followed by a large plateau. This pronounced change becomes more gradual as the D_R value is increased, and the plateau area becomes smaller and both quantities of interest become larger. This shows that it is possible to tune the mechanical response to achieve relatively low $P_{critical}$ and high $E_{absorbed}$, or vice versa, solely by manipulating the values of second moments of area. However, for high D_R values, the second moments of area need to be similar to make the structure coilable.

The last Figure 4.6 presents the dependence of $P_{critical}$ and $E_{absorbed}$ on the torsion constant. The critical buckling values were largely invariant to changes in I_y, however they were strongly tied with the values of J_τ. On the contrary, $E_{absorbed}$ were firmly correlated with I_y and only minorly varied with the change of torsion constant. Highest values of

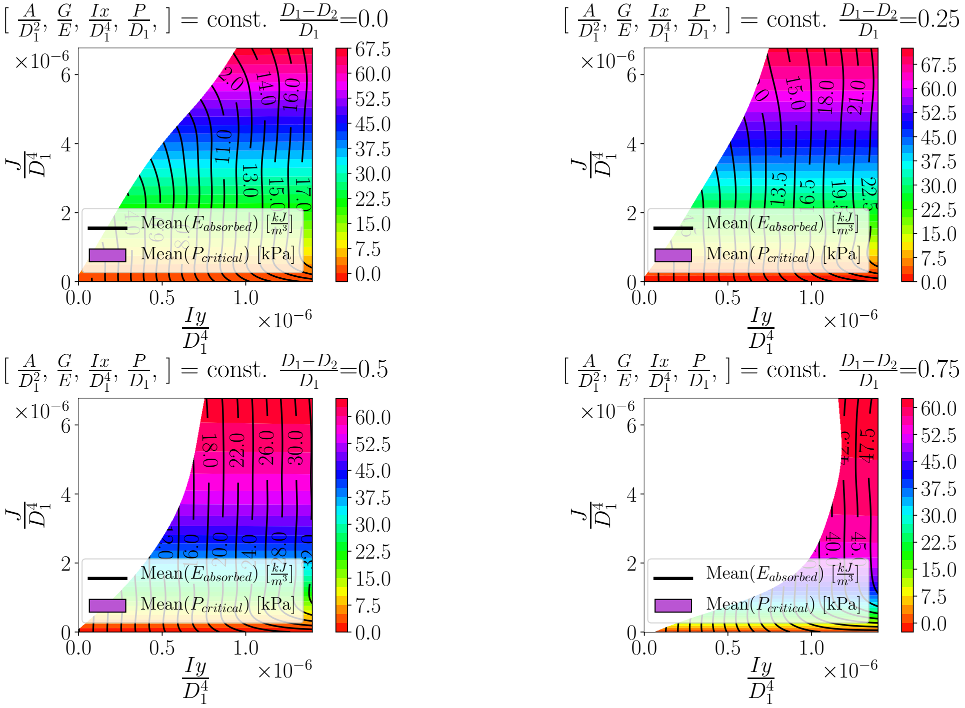

Figure 4.6: Mean quantities of interest as function of I_y , J_τ and D_R. The A=0.001, G/E=0.36, $I_x = 7.5\times10^{-7}$, and P=0.66 remain constant.

both quantities of interest are achieved for large D_R values, yet again these designs are predominantly classified as non-coilable.

4.3. SENSITIVITY ANALYSIS

Sensitivity analysis is the study of how the outputs of a model vary according to variations of the model inputs [109, 110]. Assuming that the input features or factors are independent of each other, the input/output scatter plots are a simple way of visualizing sensitivity, as they can provide a depiction of the relative importance of the factors. The influence of factors is then crudely measured by performing simple linear regression for the points in each of the scatter plots, a horizontal line is a symptom of a non influential factor, whereas higher slope values are associated with more influential factors [110]. Scatter plots for both $P_{critical}$ and $E_{absorbed}$ are presented respectively in Figure 4.7 and Figure 4.8.

The sensitivity analysis performed herein serves dual purpose. The Factor Prioritization is used to identify a factor which, when fixed to its true value, leads to the greatest reduction in the variance of the output [110]. Therefore, it allows to detect and rank those factors which need to be better measured in order to reduce the output variance and

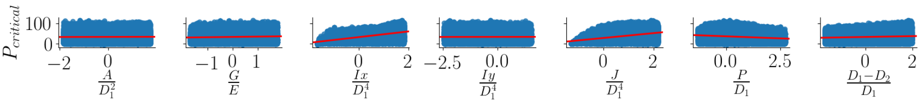

Figure 4.7: Scatterplots of critical buckling load as function of design parameters.

which factor is most deserving of further analysis [110]. Factor prioritization is indicated by the by the so-called first order sensitivity index S1 , and is a measure of the main effect.

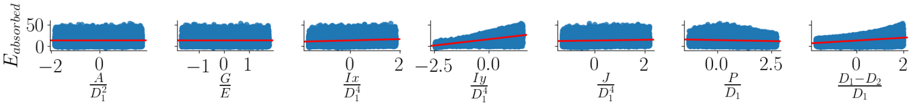

Figure 4.8: Scatterplots of energy absorbed as function of design parameters.

The second purpose is Factor Fixing. It is used to identify factors which, left free to vary over their range of uncertainty, make no significant contribution to the variance of the output [110]. The identified factors can then be set to any given value within their range of variation without influencing the output variance. Factor prioritization is indicated by the by the so-called total order sensitivity index ST. A value of zero implies that a given input is noninfluential and can be fixed anywhere in its distribution without affecting the variance of the output. For further information on calculation of sensitivity indices the reader is referred to Saltelli et al. [110].

In this work we performed variance-based Sobol global sensitivity analysis [109, 110] using the SAlib library in Python [111]. The author is aware that it shall be best practice to use the Sobol sequence of DoE and the output values generated directly from the simulations, however due to criteria for coilability and 80% strain, the DoE sequence becomes discontinuous. Thus, it was necessary to perform new quasi-random sample from the bounds of the DoE of 32000 points and subsequently utilize the machine learning models to generate new output values that determine the sensitivity indices. Consequently, the sensitivity analysis contains input points without the criteria, yet the model used to evaluate those inputs does consider strain and coilability criteria. This might be a source of discrepancy for the determined sensitivity indexes, but the analysis is consistent with the observations of various projections of the space, as discussed next. Therefore, the sensitivity analysis provides valuable insights. The bar plot in Figure 4.9 presents the first and total sensitivity indices of every factor for both quantities of interest.

The results of sensitivity analysis largely confirm the observations made for the contour plots in the preceding section. The torsion constant J_τ and I_x are the most influential factors for the value of the critical buckling load, whereas I_y and D_R are the most important for energy absorption. As the longerons become thicker in the radial direction the I_x grows cubically, significantly increasing the resistance to bending along the circumfer-

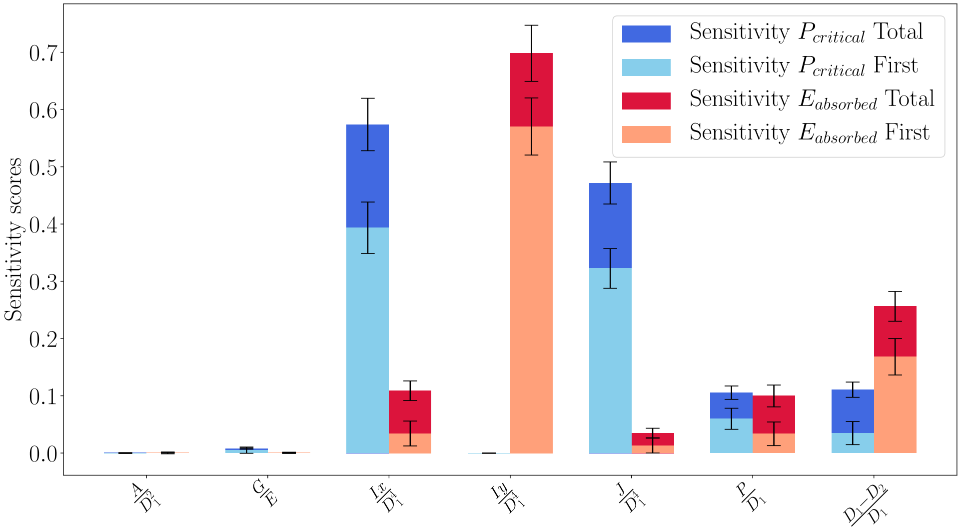

Figure 4.9: Global sensitivity indices for $P_{critical}$ and $E_{absorbed}$.

ence of the base of the design. The torsion constant has similar effect as it increases the resistance to twisting around the center of mass of a given longeron cross section.

The total order sensitivity indices for these design parameters show that higher order sensitivity is also present. This means that higher order correlations between the input parameters influence the outputs, in some cases. For example, the first order sensitivity for D_R is relatively small, however the total index is larger which implies coupled interactions between $J_\tau - D_R$ or $I_x - D_R$. The height of the design P has similar sensitivity as D_R, yet the proportion is inverted with first order sensitivity higher than the total sensitivity, which shows that this parameter has a more direct effect on values of $P_{critical}$. This is confirmed by the scatter plot, as the slope of P/D_1 is greater than in the case of D_R. We also note that the critical buckling load manifests inverse proportionality to P/D_1, i.e. as the longerons become longer the force required for buckling is smaller. The influence of the G/E parameter is small for $P_{critical}$ and negligible for $E_{absorbed}$. Similarly to J_τ the shear modulus affects torsion, however the torsion constant may vary across greater range in comparison to G, which is limited by the Poisson ratio, thus the effect of torsion constant is more pronounced. The impact of cross-sectional area of the longeron A is negligible for both quantities of interest. This is explained by the fact that the second moments of area fully define the bending and torsional behavior, not the cross-sectional area.

Consistently with the contour plots, the sensitivity analysis showed that I_y has the largest influence on the amount of energy absorbed, and that I_x is irrelevant to this quantity of interest. The D_R gives second highest sensitivity for $E_{absorbed}$, which is a result consistent with conventional energy absorbing materials, where frusta shaped structures have higher energy absorbtion as compared to cylindrical shape. Low sensitivity to J_τ and

G/E showed that the resistance to torque applied to the longerons has little effect on the $E_{absorbed}$.

4.4. METAMATERIAL TUNABILITY

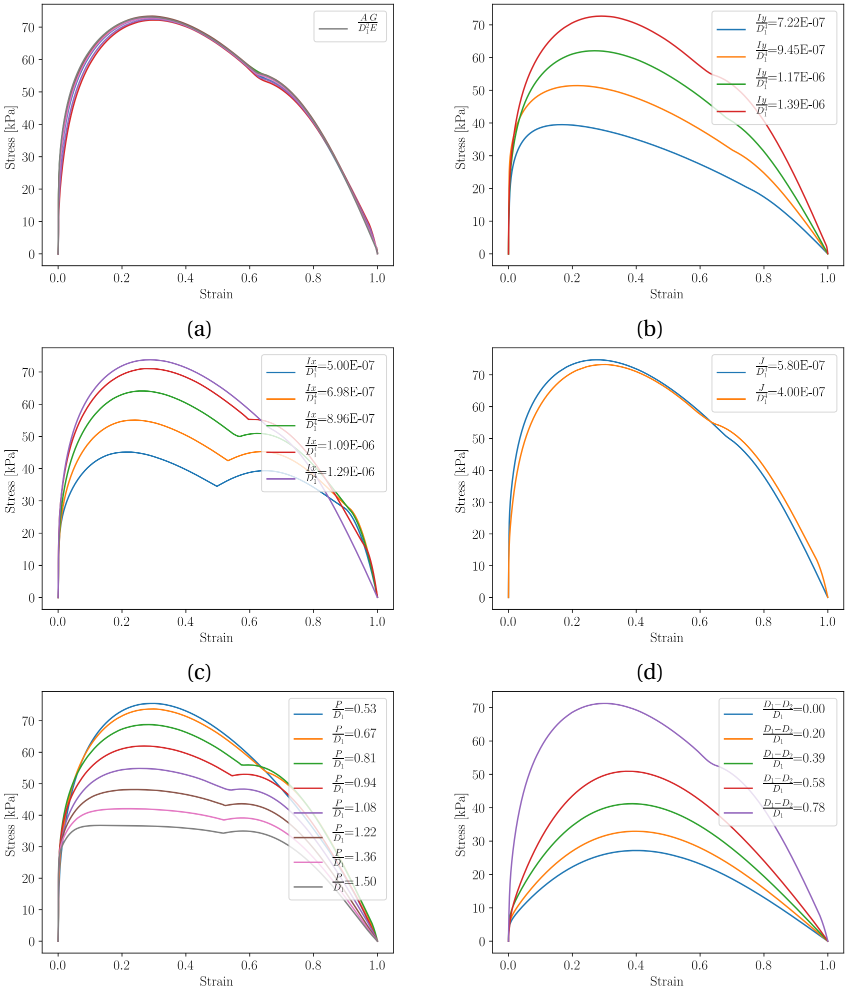

(a) (b)

(c) (d)

(e) (f)

Figure 4.10: Tunability of stress strain response of the best energy absorption design by changing different design parameters.

The information obtained from the contour plots and the results of sensitivity analysis provide significant insight into the mechanics of the proposed metamaterial. The contour plots can be used as design charts to study the influence of the input parameters, while the sensitivity analysis helps in reducing the design space to the most important parameters. Therefore, the data-driven framework enables the tunability of the metamaterial for different applications.

Focusing again on the optimal designs among all the DoE points sampled, we can now vary the input parameters around this region of the design space and reveal their impact on the quantities of interest. Thus, the base for this analysis are the stress strain curves presented in Figure 4.1 with the design parameters from Table 4.1. The effect of design parameters for the design that reached maximum energy absorbed for the dataset is presented in Figure 4.10.

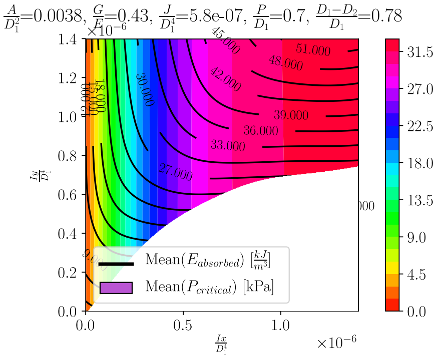

Figure 4.11: Contour plot of I_y as a function of I_x for the design with best energy absorbed.

The figure confirms that the influences of imperfection amplitude, longeron's cross sectional area and ratio of moduli are negligible. Confronting previous results with the stress-strain curves presented in Figure 4.10, some local deviations should be reported when comparing the global sensitivity of the metamaterial to the local sensitivity around this design (optimal DoE point). For this design, relatively low values of J_τ are necessary for the structure to be coilable, as only two simulations finished successfully (Figure 4.10 d), which is further demonstrated by the contour plot in Figure 4.11. As the height of the unit cell decreases, the $E_{absorbed}$ increases until saturation at P/D_1 of approximately 0.5, which confirms the trend for this parameter depicted in the scatter plot of the preceding section. As concluded from the previously presented contour plots, the value of D_R has a significant influence on the area under the stress-strain curve, with the possibility that the bounds of the DoE are a limiting factor.

The only visible discrepancy between the plots presented in Figure 4.10 and the previous analysis is the influence of the second moments of area. It was expected based on the global sensitivity analysis that I_x would have a small influence on the energy absorbed; however, for this particular design there is local sensitivity to this parameter, as one can see that the impact of both moments of inertia is comparable. Despite the drawbacks previously mentioned of the sensitivity analysis conducted herein, note that the reported sensitivity of I_x was comparable to that of P/D_1. Globally both parameters are relevant, although I_y was reported as more important for the energy absorbed – see Figure 4.9. Nevertheless, in the region close to the design analyzed herein, i.e. the optimal DoE point, the value of $E_{absorbed}$ is influenced similarly by both second moment of inertias, Figure 4.11. Comparing this plot with Figure 4.5, the local trend has clearly changed to more pronounced impact of I_x. Moreover, despite locally increased sensitivity to I_x for the $E_{absorbed}$, the critical buckling values remain invariant to I_y values, just as presented in the global sensitivity analysis. These results show that the developed classification and regression models show good agreement with the simulations and insofar the energy absorption is concerned, the tunability of mechanical response is then confirmed.

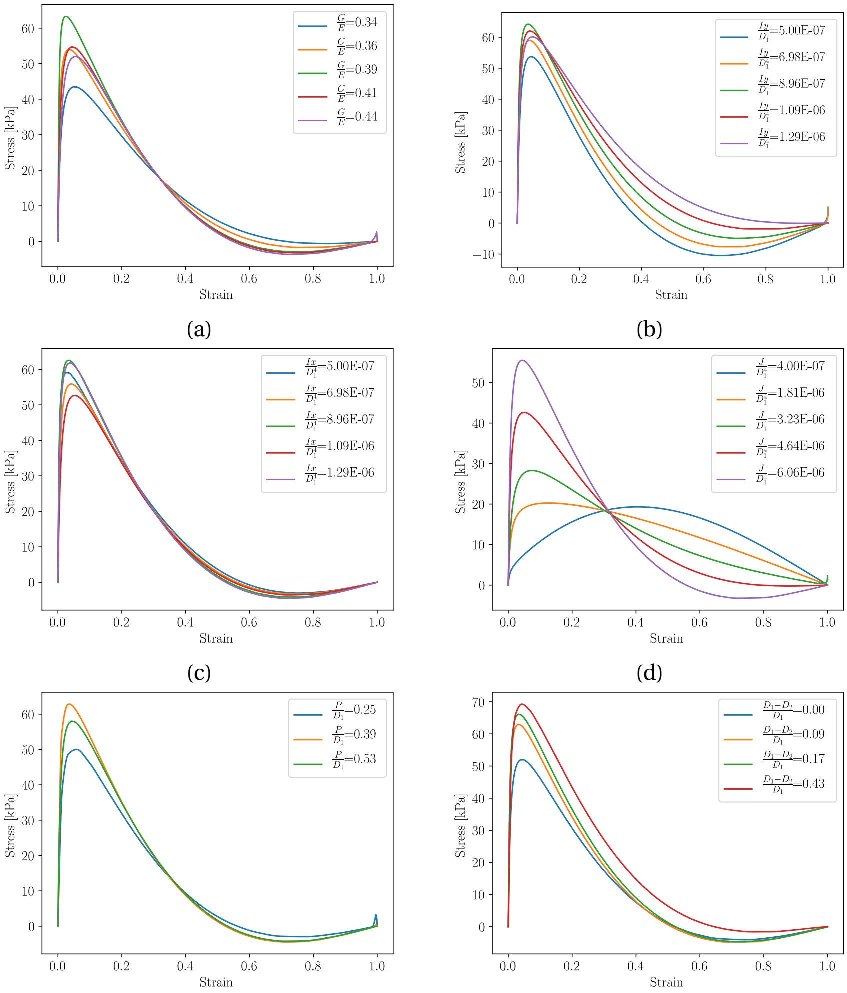

(a) (b)

(c) (d)

(e) (f)

Figure 4.12: Tunability of stress strain response of the design with best critical buckling load.

Identical procedure has been applied to the design with best critical buckling load. Analyzing Figure 4.12 one can conclude that the value of torsion constant has locally the highest influence for this design. This is confirmed by Figure 4.13 where the highest values of $P_{critical}$ are condensed to a narrow range of torsion constant values, whereas to reach the same result $I_x = 5 \times 10^{-7}$ suffices. The model also correctly predicts low values of energy absorption for the whole range of J_τ and I_x as well as low gradient for changes in $E_{absorbed}$. This may be explained by area compensation in Figure 4.12. As the value of J_τ is reduced, the area under the curve below 35% strain becomes smaller, yet simultaneously the area above that strain level becomes larger, thus the change in $E_{absorbed}$ is not drastic.

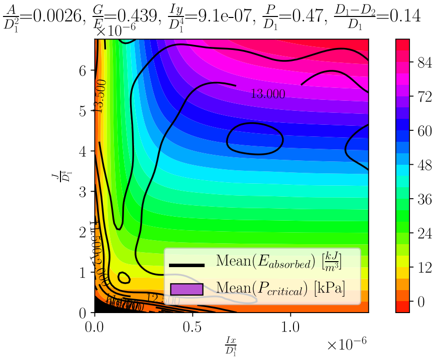

Figure 4.13: Contour plot of J_τ as a function of I_x for the design with best critical buckling load.

The remaining design parameters have similar influence on the mechanical response of the structure. Both moments of area affect $P_{critical}$ for this design. We also note a rather narrow range of P/D_1 and D_R values where the structure is coilable. This may be explained by increased probability of mixed buckling modes at higher P/D_1, and the possibility of coupled effects between large D_R and extreme torsion constant values. We also observe that a small tensile region is persistently visible in the simulations, with J_τ and I_y having the largest influence on this region. It is suspected that this may be a numerical artifact due to high values of torsion constant. Lastly, the influence of G/E ratio is comparable to that of I_x, this is consistent with the sensitivity analysis since the sensitivity index for $P_{critical}$ was nonzero. This deviation is captured by the model as presented in Figure 4.14. We see a slight difference for the extreme values of the ratio and consistently higher critical buckling values predicted by the model than depicted by the stress strain curve. This follows directly from the fact that the RIKS simulations were obtained for imperfect geometries, but the critical buckling load is obtained for idealized geometries. Therefore, $E_{absorbed}$ is obtained from the results of RIKS analysis, while the $P_{critical}$ is obtained by linear buckling analysis.

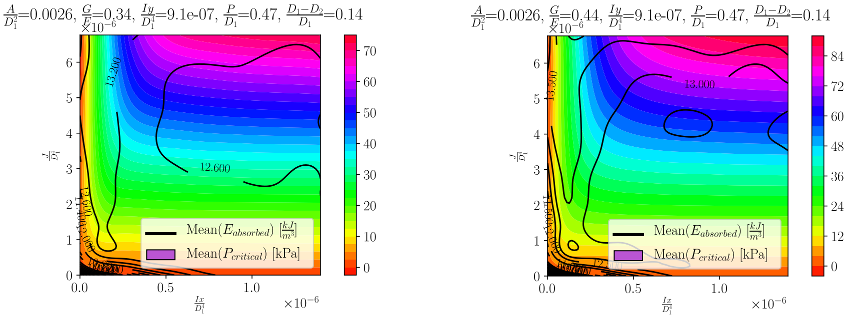

(a) (b)

Figure 4.14: Influence of the ratio of shear and elastic moduli on best designs.

Overall, the study of the presented stress-strain curves has proved the insights gained from the machine learning model and sensitivity analysis. Moreover it has justified the need to generate global models for the entire design space as local sensitivities were shown to deviate from the global trends.

5

DISCUSSION

In this thesis a novel concept of an energy absorbing metamaterial has been proposed. A universal Data-driven framework was utilized to gain better understanding of the mechanical response of the proposed concept. Within this framework, a multitude of possible designs was generated to understand the mechanical response of the concept design, based on critical buckling load and energy absorption as metrics. The framework has allowed to seed realistic design imperfections and to analyze their influence on the design. A machine learning model was developed to map the impact of design parameters on the buckling and post-buckling response. To the best of authors knowledge at the time of writing, it is the first time sparse gaussian processes had been selected for this task. Based on the findings of this work, an improved design of the metamaterial design with a realistic cross section has been recommended.

5.1. DATA-DRIVEN FRAMEWORK

The considered data-driven framework is applicable to a host of materials engineering issues. At the heart of the framework are the finite element simulations, as they define the problem to be solved and generate the quantities of interest. For the purposes of this work, quantity of simulations was crucial, therefore possible improvements to the finite element model were sacrificed at the benefit of computational time. As discussed, self-contact between longerons and slippage had not been considered. Similarly, the lack of friction in longeron hinges is not realistic. By assuming a generalized cross section, it was not possible to determine the local strains in the longerons, therefore it was not possible to determine if the structure remained in the elastic regime or if permanent deformation did occur. However, the simplified simulations were sufficient to gain deep insight on the mechanical response of the structure and added complexity of the finite element model would unnecessarily increase the computational time.

Despite the simplistic simulations, realistic imperfections based on experimental findings were included. As the seeded imperfections corresponded to the first eigenmode of buckling of design. The introduction of imperfections lowered the critical buckling load and yet the energy absorption showed low sensitivity to seeded imperfections. It was determined that to dutifully characterize the uncertainty due to imperfections, many simulations per DoE point would need to be generated, this was deemed computationally prohibitive in the considered high dimensional space. Thus, each simulation was corrupted by a single imperfection. However, as it proved difficult to determine critical buckling load form stress strain curves that increased in stress in the post-buckling regime. That is why idealized values of critical buckling load determined from linear bifurcation analysis were used to train machine learning models.

Although formal optimization routine was not conducted in this work, the extensive amount of generated simulations has allowed to find designs with quantities of interest close to optimum within the bounds of the DoE. These designs showed significant differences in design parameters. The best design for critical buckling indicated significant tensile stresses beyond 0.5 strain. Same design simulated using significantly finer mesh size retained the tensile region. Experimental work is required to confirm this behavior as it may indicate energy trapping via snap-through instability for some combinations of design parameters.

Machine learning models for the quantities of interest were generated via sparse gaussian processes. The considered neural networks model showed lower mean squared error on the dataset and considerably lower time to train, however due to generality of the framework, uncertainty quantification and the possibility of performing optimization routine that would require second order derivatives, the sparse gaussian process was selected. The model allowed to investigate the sensitivity of quantities of interest to design parameters.

Creating visualizations of high dimensional spaces is not a trivial issue and numerous projections were necessary to gain understanding of the impact of design parameters. To complement the design chart, sensitivity analysis and additional simulations were conducted. This allowed to draw conclusions on the influence of design parameters.

5.2. THE INFLUENCE OF DESIGN PARAMETERS

It was determined that the design parameters that had largest influence on E absorbed were the second moment of area around the Y-axis of the longeron I y and the ratio of ring diameters D R. Critical buckling load of the unit cell was shown to vary the most for second moment of area around the X-axis of the longeron I x and the values of torsion constant J_τ.

5.2.1. AREA OF THE LONGERON CROSS SECTION

The analysis carried out has shown that the cross-sectional area of the longeron does not effect the quantities of interest, rather it were the second moments of area largely determine the mechanical response of the unit cell. This may be explained by the assumed

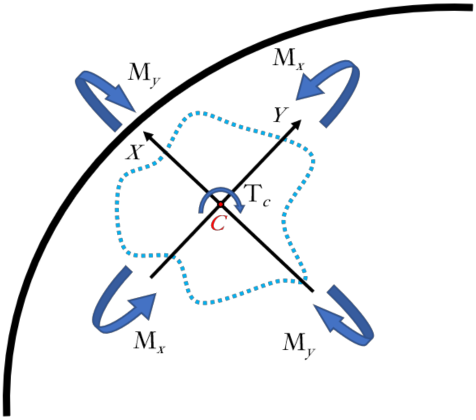

Figure 5.1: Schematic of longeron with general cross-section (top view)

independence of unit cell parameters and the fact that it is possible to obtain the same set of second moments of area for different area values depending on the shape of the cross section.

5.2.2. RATIO OF SHEAR AND ELASTIC MODULI

The ratio of G/E was shown to have no influence on the energy absorption and globally speaking marginal influence on the critical buckling values, with increased sensitivity for the best design. This is explained by the concepts of torsional rigidity GJ and bending stiffness EI. In the model we have assumed the $E = const$ and the shear modulus to vary within the physical bounds defined by the Poisson Ratio. Thus, the parameter varied within relatively tight bounds. This meant that shear modulus had a low contribution to torsional rigidity of the longeron compared to the torsion constant J_τ, which varied within a large span of values. Despite that high values of G were favored for best designs, with the differences more pronounced for the design with best critical buckling load. The elastic modulus contributes to the bending stiffness and amplifies the effect of second moments of area. Therefore we may conclude that G and E are scaling factors for respectively torsional and bending stiffness and amplify the effect of J_τ and I.

5.2.3. SECOND MOMENT OF AREA AROUND X-AXIS

Generally, as the dimension of the beam cross section perpendicular to the X-axis grows, the second moment of area around that axis increases cubically. This significantly raises the bending stiffness of the longeron around that axis. Thus, the resistance to the applied bending moment M_x increases , as shown in Figure 5.1, and larger force is required for buckling. As all the considered designs buckle according to first eigenmode ie .global rotation of the design, the resistance to bending in direction tangent to the ring becomes critical and the bending resistance in the radial direction plays no significant role for critical buckling. In terms of energy absorption, for the same longeron deflection as resistance to the bending moment increases, the elastics strain energy will increase as well. However, as the ends of the longeron are hinged this effect is globally smaller than for I_y.

5.2.4. SECOND MOMENT OF AREA AROUND Y-AXIS

For reasons postulated above and in chapter 4, I_y has only marginal global impact on critical buckling values. However as discussed in chapter 2.2 and 2.3 the energy absorption is largely governed by the thickness of the beam, or more precisely the slenderness ratio. In the case of the proposed design it is largely true and as the thickness of the longeron increases in the X-direction, the resistance to bending moment M_y increases and consequently the energy absorption. Second order effects of I_y with other parameters are significant, most notably with the ratio of ring diameters D_R.

5.2.5. TORSION CONSTANT

The longerons twist along their length during retraction of the unit cell. The torsional stiffness of the longeron has a significant impact on the critical buckling load. The higher the resistance to applied torque Tc in figure, the higher critical buckling load. As discussed, torsional rigidity is largely determined by J_τ rather than shear modulus as the latter is limited by the Poisson ratio. It was observed that globally the impact of this parameter was low for the values of energy absorption, yet direct simulations have shown that the shape of stress-strain curves varies significantly with this parameter. It is possible that the lack of area under the curve at low values may be compensated by increased area far into post-buckling regime. Thus, the total area under the curve remained largely unchanged. It was also observed that the best design for energy absorption was simulated only within a narrow range of J_τ values. This suggests that pronounced warpage of the cross section is necessary to obtain high energy absorption in combination with high I_y and D_R. Likewise, for a constant torque the work done to twist the longeron increases together with the rotational displacement.

5.2.6. HEIGHT OF THE UNIT CELL

The height of the unit cell coupled with the ratio of ring diameters determines the length of the longeron. In many previous studies the slenderness of a beam-like element determined the mechanical response. The critical buckling is inversely quadratically proportional to the length of the longeron whereas the energy absorption is directly proportional. This would suggest that we could easy tune the design by varying the pitch. However, it was observed that P/D was the only parameter that showed clear peak value. It was determined from the contour maps that for null D_R the quantities of interest were a weak function of unit cell height, yet as D_R increased to the opposite boundary of the DoE, the range of optimal height values became narrower and peaked at approx. $P/D = 0.5$ It was also observed in chapter 4.4 that as P/D is increased, the stiffening in post-buckling regime is surpressed leading to lower energy absorption.

5.2.7. RATIO OF RING DIAMETERS

It was shown by the analysis that both quantities of interest increase with D_R , yet the effect was more pronounced for energy absorption than for critical buckling load. This can be explained by the increased length of the longeron in the case of critical buckling loads. For energy absorption the impact was significant and is possibly explained by amplification of the M_y bending component. However the effect of this parameter is unsurprising given the discussed frusta structures have increased energy absorption at higher semi-apical angles and many metamaterials in literature showed pronounced sensitivity to the beam tilt angle.

5.2.8. REALISTIC CROSS-SECTION

We have insofar concluded that the cross-sectional shape of the longeron has crucial impact on the mechanical response of the structure. To achieve highest values of $P_{critical}$, I_x and J_τ must be maximized. In this case we propose closed rectangular or ellipsoid section to satisfy both conditions.

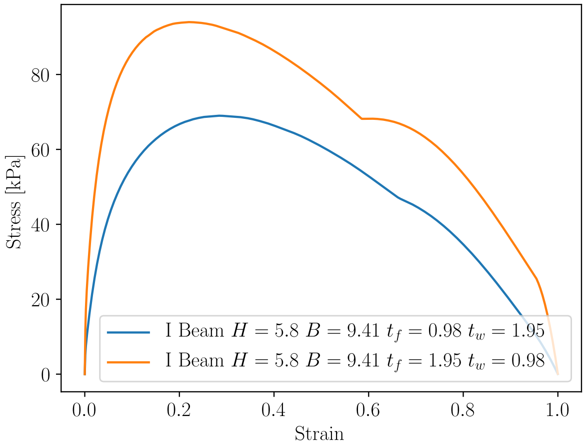

Figure 5.2: Comparison of stress strain curves for I-beams of differing flange and web thicknesses.

For energy absorption design, high bending and low torsion resistance are required. For this reason, open cross sections are suitable. Thus, we propose an I-beam cross section with differing thicknesses for the flanges and web, but equal flange widths. An equivalent I-beam cross-section has been simulated for the best design for energy absorbed. The reported energy absorption was 49 kJ/m^3. The shape of the stress-strain curve was identical with that presented previously in this work. The local elastic strains in the longerons reached 16%. We acknowledge that this is a high value in the elastic regime, however some materials exist that that do exhibit such high strains without yielding. By exchanging the values of thickness for the flange and web of the I-beam, the local strain was reduced to 10%, while I_y increased significantly and therefore the energy absorption increased as well, see Figure 5.2. The parameters of the new design are presented in Table 5.1.

Table 5.1: Design parameters of new design

	A [mm^2]	G/E	I_x [mm^4]	I_y [mm^4]	J_τ [mm^4]	P [mm]	D_R
I-beam	38.6	0.430	148.1	271.0	47.3	70	0.78

However, we have found that the values of E modulus and the longeron number are scaling factors for the design. If this is true, then it is possible to achieve significantly higher buckling loads and energy absorption by increasing the number of longerons and the elastic modulus. Carbon nanotubes reported in [112] have been selected as the substrate material, due to their ability to reach 12% linear elastic strain. The elastic modulus of the carbon nanotubes was $E = 944.2$ GPa, with Poisson ratio of 0.3.

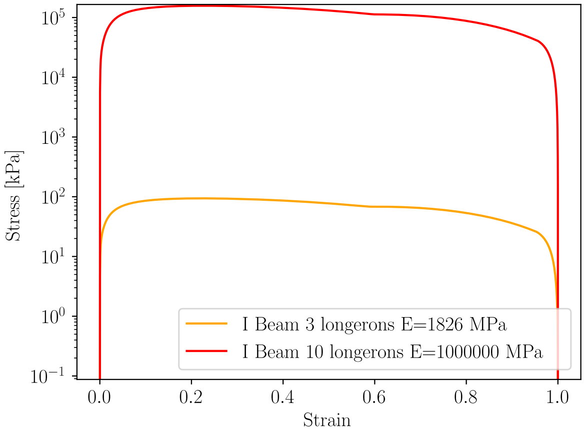

Figure 5.3: Comparison of new design with modified differing values of longerons and elastic modulus E.

The results are presented in Figure 5.3,the shape of the curve for the design depicted in Figure 5.2 changed due to logarithmic scale for vertical axis. The curve was shifted upward as expected, the shear modulus did not influence the post-buckling response as predicted by the analysis. The proposed design achieved energy absorption of 114497, 8 kJ/m^3. Moreover, the maximum local strained remained at 10%, yet the data is insufficient to conclude that globally the local strains are independent the substrate material properties. The renders of the new design are shown in Figure 5.4.

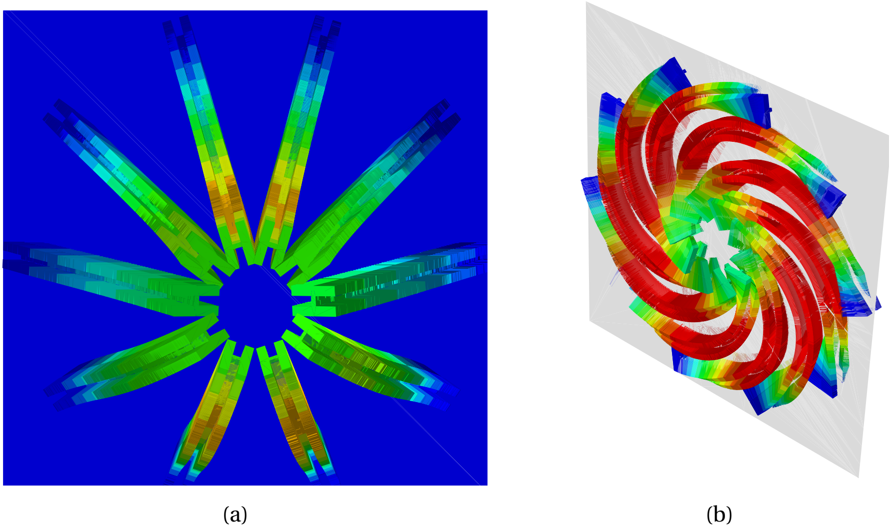

(a) (b)

Figure 5.4: Renders of the new design with I-beam cross section and ten longerons.

6

CONCLUSION AND RECOMMENDATIONS

This thesis has contributed to the design of a novel energy absorbing metamaterial by mapping the influence of design parameters on the mechanical response of the unit cell. The insights gained allowed to propose a new improved design for the metamaterial unit cell.

6.1. CONCLUSIONS

- It was confirmed that by tuning the design parameters, significantly different buckling and post-buckling behavior is possible.
- The sparse gaussian process machine learning model showed good predictability with the ability to map the influence of design parameters.
- We have demonstrated that the elastic modulus and longeron number are scaling factors for the quantities of interest.
- For a given E, the second moment of area around the longeron cross-section axis parallel to the radial direction of the unit cell axis of rotation and the torsion constant of the cross section have highest impact on critical buckling loads of the unit cell.
- For a given E, the magnitude of energy absorption was found to be most sensitive to moment of area around the longeron cross-section axis perpendicular to the radial direction of the unit cell axis of rotation and the ratio of ring diameters.
- The increased buckling load and energy absorption has been attributed to the resistance to bending components of the longerons.

- The introduction of first buckling eigenmode imperfections lead to lowered critical buckling load, however their impact was only marginal for the energy absorbtion capability.
- The interaction between the design parameters was non-trivial with significant deviations between the local and global sensitivities.

6.2. RECOMMENDATIONS

Despite the simplicity of the computational simulations, it was possible to develop deep understanding of how design parameters modify the mechanical response of the structure. The logical next step, as indicated by the framework, would be to perform optimization for energy absorption. Thus, the recommendations are:

1. Generate a new DoE for a selected longeron cross-sectional shape, we propose the I-beam shape, to obtain local strains in the structure.
2. Refine the simulation procedure by additional linear buckling simulation that would consider the imperfections seeded.
3. Consider and model other imperfection sources such as friction of the hinges and self-contact between the longerons at the expense of computation time.
4. Create new machine learning model with local strains as the third quantity of interest.
5. Perform multi objective optimization with the targets of maximizing the energy absorbed and minimizing the local strains in the unit cell.

The next or alternative step would be to validate the findings experimentally. Confirmation of behavior of the unit cell at nanoscale could be an interesting topic. Lastly the interaction of the unit cells arranged in a 3D matrix is to be conducted.

REFERENCES

[1] L. Puig, A. Barton, and N. Rando, *A review on large deployable structures for astrophysics missions,* Acta Astronautica **67**, 12 (2010).

[2] C. Wujun, L. Yaozhi, F. Gongyi, G. Jinghai, and D. Shilin, *Design Conception and Deployment Simulation for a Highly Synchronized Extendable/Retractable Space Mast,* International Journal of Space Structures **16**, 261 (2001).

[3] Z. Xu, Y. Guannan, H. Hai, and W. Xinsheng, *Deployment analysis and test of a coilable mast for buaa student micro-satellite,* in *2010 3rd International Symposium on Systems and Control in Aeronautics and Astronautics* (8-10 June 2010) pp. 1329–1332.

[4] *Nustar deployable mast,* `https://www.nustar.caltech.edu/page/mast`, accessed: 2018-03-19.

[5] O. Stohlman and S. Pellegrino, *Shape Accuracy of a Joint-Dominated Deployable Mast,* 51st AIAA/ASME/ASCE/AHS/ASC Structures, Structural Dynamics, and Materials Conference
 18th AIAA/ASME/AHS Adaptive Structures Conference
 12th (2010), 10.2514/6.2010-2605.

[6] X. Zhou, G. Yue, H. Huang, and X. Wang, *Deployment analysis and test of a coilable mast for BUAA student micro-satellite,* ISSCAA2010 - 3rd International Symposium on Systems and Control in Aeronautics and Astronautics , 1329 (2010).

[7] S. D. Guest, *Deployable Structures : Concepts and Analysis,* Corpus Christi College , 2010 (1994).

[8] M. Hillebrandt, M. Straubel, C. Huhne, and M. Wiedemann, *A New Deployable Truss for Gossamer Space Structures,* in *53rd AIAA/ASME/ASCE/AHS/ASC Structures, Structural Dynamics and Materials Conference* (2012).

[9] H. Q. Li, X. F. Liu, S. J. Guo, and G. P. Cai, *Deployment dynamics and control of large-scale flexible solar array system with deployable mast,* Advances in Space Research (2016), 10.1016/j.asr.2016.06.008.

[10] Z. You and S. Pellegrino, *Cable-stiffened pantographic deployable structures. I - Triangular mast,* AIAA Journal (1996), 10.2514/3.13144.

[11] H. Ma, H. Huang, J. Han, W. Zhang, and X. Wang, *Study on the criterion to determine the bottom deployment modes of a coilable mast,* Acta Astronautica **141**, 89 (2017).

[12] J. L. Ge, Y. Z. Wang, J. W. Hao, and G. L. Yang, *Finite Element Modeling and Modal Analysis of Bolted Joints,* Applied Mechanics and Materials **105-107**, 92 (2011).

[13] D. M. Murphy, T. W. Murphey, and P. A. Gierow, *Scalable Solar-Sail Subsystem Design Concept,* Journal of Spacecraft and Rockets **40**, 539 (2003).

[14] T. Kitamura, K. Okazaki, M. Natori, K. Miura, S. Sato, and A. Obata, *Development of a "hingeless mast" and its applications,* Acta Astronautica **17**, 341 (1988).

[15] M. EIDEN, O. BRUNNER, and C. STAVRINIDIS, *Deployment analysis of the Olympus Astromast and comparison with test measurements,* Journal of Spacecraft and Rockets **24**, 63 (1987).

[16] J. R. Greer, D. Jang, J. Y. Kim, M. J. Burek, and M. J. Burek, *Emergence of new mechanical functionality in materials via size reduction,* Advanced Functional Materials **19**, 2880 (2009).

[17] A. Boczkowska, *Composites* (Oficyna Wydawnicza Politechniki Warszawskiej, 2000) p. 180.

[18] K. Bertoldi, V. Vitelli, J. Christensen, and M. Van Hecke, *Flexible mechanical metamaterials,* Nature Reviews Materials **2** (2017), 10.1038/natrevmats.2017.66.

[19] S. Babaee, J. Shim, J. C. Weaver, E. R. Chen, N. Patel, and K. Bertoldi, *3D soft metamaterials with negative poisson's ratio,* Advanced Materials **25**, 5044 (2013).

[20] C. Coulais, C. Kettenis, and M. van Hecke, *A characteristic lengthscale causes anomalous size effects and boundary programmability in mechanical metamaterials,* **14** (2017), 10.1038/nphys4269, arXiv:1708.04643 .

[21] A. Rafsanjani and D. Pasini, *Bistable auxetic mechanical metamaterials inspired by ancient geometric motifs,* Extreme Mechanics Letters **9**, 291 (2016), arXiv:1612.05988 .

[22] D. Mousanezhad, S. Babaee, H. Ebrahimi, R. Ghosh, A. S. Hamouda, K. Bertoldi, and A. Vaziri, *Hierarchical honeycomb auxetic metamaterials,* Scientific Reports **5** (2015), 10.1038/srep18306.

[23] F. Göncü, S. Willshaw, J. Shim, J. Cusack, S. Luding, T. Mullin, and K. Bertoldi, *Deformation induced pattern transformation in a soft granular crystal,* Soft Matter **7**, 2321 (2011).

[24] L. Montemayor, V. Chernow, and J. R. Greer, *Materials by design: Using architecture in material design to reach new property spaces,* MRS Bulletin **40**, 1122 (2015).

[25] A. Rafsanjani, A. Akbarzadeh, and D. Pasini, *Snapping Mechanical Metamaterials under Tension,* Advanced Materials **27**, 5931 (2015), arXiv:1612.05987 .

[26] L. Dong and R. Lakes, *Advanced damper with high stiffness and high hysteresis damping based on negative structural stiffness,* International Journal of Solids and Structures (2013), 10.1016/j.ijsolstr.2013.03.018.

[27] M. Serra-Garcia, J. Lydon, and C. Daraio, *Extreme stiffness tunability through the excitation of nonlinear defect modes,* Physical Review E (2016), 10.1103/PhysRevE.93.010901, arXiv:1411.5242 .

[28] R. Gatt, R. Caruana-Gauci, and J. N. Grima, *Negative linear compressibility: Giant response,* Nature Materials (2013), 10.1038/nmat3584.

[29] Z. G. Nicolaou and A. E. Motter, *Mechanical metamaterials with negative compressibility transitions,* Nature Materials (2012), 10.1038/nmat3331, arXiv:1207.2185 .

[30] X. Shang, L. Liu, A. Rafsanjani, and D. Pasini, *Durable bistable auxetics made of rigid solids,* Journal of Materials Research , 1 (2017), arXiv:1711.09336 .

[31] D. Restrepo, N. D. Mankame, and P. D. Zavattieri, *Phase transforming cellular materials,* Extreme Mechanics Letters **4**, 52 (2015).

[32] C. Coulais, E. Teomy, K. De Reus, Y. Shokef, and M. Van Hecke, *Combinatorial design of textured mechanical metamaterials,* Nature **535**, 529 (2016), arXiv:1608.00625 .

[33] Y. Jiang and Q. Wang, *Highly-stretchable 3D-architected Mechanical Metamaterials,* Scientific Reports (2016), 10.1038/srep34147.

[34] T. Bückmann, M. Thiel, M. Kadic, R. Schittny, and M. Wegener, *An elasto-mechanical unfeelability cloak made of pentamode metamaterials,* Nature Communications (2014), 10.1038/ncomms5130.

[35] B. Florijn, C. Coulais, and M. Van Hecke, *Programmable mechanical metamaterials,* Physical Review Letters **113**, 8736 (2014), arXiv:1407.4273 .

[36] J. T. Overvelde, J. C. Weaver, C. Hoberman, and K. Bertoldi, *Rational design of reconfigurable prismatic architected materials,* Nature **541**, 347 (2017).

[37] L. R. Meza, A. J. Zelhofer, N. Clarke, A. J. Mateos, D. M. Kochmann, and J. R. Greer, *Resilient 3D hierarchical architected metamaterials,* Proceedings of the National Academy of Sciences **112**, 11502 (2015).

[38] K. Bertoldi, *Harnessing Instabilities to Design Tunable Architected Cellular Materials,* Annual Review of Materials Research **47**, 51 (2017).

[39] D. Kochmann and K. Bertoldi, *Exploiting microstructural instabilities in solids and structures: from metamaterials to structural transitions,* Applied Mechanics Reviews **69** (2017), 10.1115/1.4037966.

[40] M. Taylor, L. Francesconi, M. Gerendás, A. Shanian, C. Carson, and K. Bertoldi, *Low porosity metallic periodic structures with negative poisson's ratio,* Advanced Materials **26**, 2365 (2014).

[41] J. T. Overvelde, T. A. De Jong, Y. Shevchenko, S. A. Becerra, G. M. Whitesides, J. C. Weaver, C. Hoberman, and K. Bertoldi, *A three-dimensional actuated origami-inspired transformable metamaterial with multiple degrees of freedom,* Nature Communications **7,** 1 (2016), arXiv:arXiv:1011.1669v3 .

[42] J. T. Miller, T. Su, J. Pabon, N. Wicks, K. Bertoldi, and P. M. Reis, *Buckling of a thin elastic rod inside a horizontal cylindrical constraint,* Extreme Mechanics Letters **3,** 36 (2015).

[43] J. Shim, C. Perdigou, E. R. Chen, K. Bertoldi, and P. M. Reis, *Buckling-induced encapsulation of structured elastic shells under pressure,* Proceedings of the National Academy of Sciences **109,** 5978 (2012).

[44] C. Coulais, J. T. B. Overvelde, L. A. Lubbers, K. Bertoldi, and M. Van Hecke, *Discontinuous Buckling of Wide Beams and Metabeams,* Physical Review Letters **115,** 1 (2015), arXiv:1410.6016 .

[45] U. M. Microlattices, M. D. Lima, S. Fang, X. Lepró, C. Lewis, R. Ovalle-robles, J. Carretero-gonzález, E. Castillo-martínez, M. E. Kozlov, J. Oh, N. Rawat, C. S. Haines, M. H. Haque, V. Aare, S. Stoughton, A. A. Zakhidov, R. H. Baughman, and U. M. Microlattices, *Ultralight Metallic Microlattices SI,* **334,** 1 (2011).

[46] D. Jang, L. R. Meza, F. Greer, and J. R. Greer, *Fabrication and deformation of three-dimensional hollow ceramic nanostructures,* Nature Materials **12,** 893 (2013), arXiv:arXiv:1111.0651v1 .

[47] L. R. Meza and J. R. Greer, *Mechanical characterization of hollow ceramic nanolattices,* Journal of Materials Science **49,** 2496 (2014).

[48] L. R. Meza, S. Das, and J. R. Greer, *Strong , Lightweight and Recoverable Three - Dimensional Ceramic Nanolattices,* Science **345,** 1322 (2014).

[49] L. C. Montemayor and J. R. Greer, *Mechanical Response of Hollow Metallic Nanolattices: Combining Structural and Material Size Effects,* Journal of Applied Mechanics **82,** 071012 (2015).

[50] K. Bertoldi, *Harnessing Instabilities to Design Tunable Architected Cellular Materials,* Annual Review of Materials Research **47,** 51 (2017).

[51] S. Shan, S. H. Kang, J. R. Raney, P. Wang, L. Fang, F. Candido, J. A. Lewis, and K. Bertoldi, *Multistable Architected Materials for Trapping Elastic Strain Energy,* Advanced Materials **27,** 4296 (2015), arXiv:1207.1956 .

[52] A. A. Alghamdi, *Collapsible impact energy absorbers: An overview,* Thin-Walled Structures **39,** 189 (2001).

[53] B. T. A. Schaedler, C. J. Ro, A. E. Sorensen, Z. Eckel, S. S. Yang, W. B. Carter, and A. J. Jacobsen, *Designing Metallic Microlattices for Energy Absorber Applications **,* , 276 (2014).

[54] W. W. W. Johnson, *METALLIC ENERGY DISSIPATING SYSTEMS,* Applied Mechanics Reviews **31**, 277 (1978).

[55] A. G. Mamalis and W. Johnson, *The quasi-static crumpling of thin-walled circular cylinders and frusta under axial compression,* International Journal of Mechanical Sciences (1983), 10.1016/0020-7403(83)90078-4.

[56] S. Santosa and T. Wierzbicki, *Crash behavior of box columns filled with aluminum honeycomb or foam,* Computers and Structures **68**, 343 (1998).

[57] X. Zhang and G. Cheng, *A comparative study of energy absorption characteristics of foam-filled and multi-cell square columns,* International Journal of Impact Engineering **34**, 1739 (2007).

[58] H. A. Rt, L. Heerstra, and G. E-mail, *Deformation characteristics of metal foams,* **3** (1998).

[59] Z. Ahmad and D. P. Thambiratnam, *Dynamic computer simulation and energy absorption of foam-filled conical tubes under axial impact loading,* Computers and Structures **87**, 186 (2009).

[60] M. F. Ashby, *The mechanical properties of cellular solids,* Metallurgical Transactions A **14**, 1755 (1983).

[61] B. Haghpanah, L. Salari-Sharif, P. Pourrajab, J. Hopkins, and L. Valdevit, *Architected Materials: Multistable Shape-Reconfigurable Architected Materials (Adv. Mater. 36/2016),* Advanced Materials **28**, 8065 (2016).

[62] A. K. Jain, R. P. Duin, and J. Mao, *Statistical pattern recognition: A review,* IEEE Transactions on Pattern Analysis and Machine Intelligence (2000), 10.1109/34.824819.

[63] C. M. Bishop, *Journal of Organic Chemistry* (Springer, 2006) arXiv:arXiv:1011.1669v3 .

[64] S. Legg and M. Hutter, *Universal intelligence: A definition of machine intelligence,* Minds and Machines **17**, 391 (2007), arXiv:0712.3825 .

[65] I. H. Witten, *Data Mining* (Elsevier, 2011).

[66] A. H. Fielding, *Machine Learning Methods for Ecological Applications* (1999) pp. 1–35, arXiv:1702.00832 .

[67] V. N. Vapnik, *An Overview of Statistical Learning Theory,* Ieee Transactions on Neural Networks **10**, 988 (1999).

[68] J. Shendure and H. Ji, *Next-generation DNA sequencing,* (2008), arXiv:1111.6189v1 .

[69] J. P. Jiawei Han, Micheline Kamber, *Data Mining – Concepts & Techniques* (2011) pp. 1–744.

[70] J. Li, L. Deng, R. Haeb-Umbach, and Y. Gong, *Fundamentals of speech recognition,* in *Robust Automatic Speech Recognition* (2016) arXiv:1001.2267 .

[71] Y. Lecun, Y. Bengio, and G. Hinton, *Deep learning,* Nature **521**, 436 (2015), arXiv:arXiv:1312.6184v5 .

[72] B. Hinton, G., Deng, L., Yu, D., Dahl, G., Mohamed, A., Jaitly, N., … Kingsbury, *Deep Neural Networks for Acoustic Modeling in Speech Recognition.* IEEE Signal Processing Magazine (2012), 10.1109/MSP.2012.2205597, arXiv:1207.0580 .

[73] Y. Taigman, M. Yang, M. Ranzato, and L. Wolf, *DeepFace: Closing the gap to human-level performance in face verification,* in *Proceedings of the IEEE Computer Society Conference on Computer Vision and Pattern Recognition* (2014) arXiv:1501.05703 .

[74] A. Mian and N. Pears, *3D face recognition,* in *3D Imaging, Analysis and Applications* (2014) arXiv:arXiv:1011.1669v3 .

[75] S. Shalev-shwartz, C. Science, S. Ben-david, and C. Science, *Understanding Machine Learning*.

[76] M. A. Bessa, R. Bostanabad, Z. Liu, A. Hu, D. W. Apley, C. Brinson, W. Chen, and W. K. Liu, *A framework for data-driven analysis of materials under uncertainty: Countering the curse of dimensionality,* Computer Methods in Applied Mechanics and Engineering **320**, 633 (2017).

[77] J. Schmidhuber, *Deep Learning in neural networks: An overview,* Neural Networks **61**, 85 (2015), arXiv:1404.7828 .

[78] S. Russell and P. Norvig, *AI - A modern approach* (2009) pp. 1–1153, arXiv:arXiv:1011.1669v3 .

[79] T. M. Mitchell, *(Mcgraw-Hill International Edit) Thomas Mitchell-Machine learning-McGraw Hill Higher Education (1997)*, arXiv:0-387-31073-8 .

[80] C. E. R. &. C. K. I. Williams, *International Journal of Neural Systems* (2006) arXiv:026218253X .

[81] M. SEEGER, *GAUSSIAN PROCESSES FOR MACHINE LEARNING,* International Journal of Neural Systems (2004), 10.1142/S0129065704001899, arXiv:026218253X .

[82] K. Muller, S. Mika, G. Ratsch, K. Tsuda, and B. Scholkopf, *An {I}ntroduction to {K}ernel-{B}ased {L}earning {A}lgorithms,* {IEEE} {T}ransactions on {N}eural {N}etworks **12**, 181 (2001).

[83] H. Liu, Y.-S. Ong, X. Shen, and J. Cai, *When Gaussian Process Meets Big Data: A Review of Scalable GPs,* , 1 (2018), arXiv:1807.01065 .

[84] M. Bauer, M. V. D. Wilk, and C. E. Rasmussen, *Understanding Probabilistic Sparse Gaussian Process Approximations,* (2016), arXiv:arXiv:1606.04820v2 .

[85] A. G. D. G. Matthews, J. Hensman, R. E. Turner, and Z. Ghahramani, *On Sparse Variational Methods and the Kullback-Leibler Divergence between Stochastic Processes,* **41** (2016).

[86] M. Opper, *The Variational Gaussian Approximation Revisited The variational Gaussian approximation,* , 1 (2009).

[87] A. Graeme and D. G. Matthews, *Scalable Gaussian process inference using variational methods,* (2016).

[88] M. K. Titsias, *Variational Learning of Inducing Variables in Sparse Gaussian Processes,* **5**, 567 (2009).

[89] J. Qui, *A Unifying View of Sparse Approximate Gaussian Process Regression,* **6**, 1939 (2005).

[90] E. Snelson, *Sparse Gaussian Processes using Pseudo-inputs,* (2006).

[91] J. Kriwet and S. Klug, *A new Jurassic cow shark (Chondrichthyes, Hexanchiformes) with comments on Jurassic hexanchiform systematics,* Swiss Journal of Geosciences **104** (2011), 10.1007/s00015-011-0075-z.

[92] J. Hensman, U. Sheffield, N. Fusi, and N. N. D. Lawrence, *Gaussian Processes for Big Data,* Proceedings of UAI 29 (2013), 10.1162/089976699300016331, arXiv:1309.6835 .

[93] E. Snelson and Z. Ghahramani, *Variable noise and dimensionality reduction for sparse Gaussian processes,* (2012), 10.3923/rjet.2011.369.377, arXiv:1206.6873 .

[94] M. A. Bessa and S. Pellegrino, *International Journal of Solids and Structures Design of ultra-thin shell structures in the stochastic post-buckling range using Bayesian machine learning and optimization,* International Journal of Solids and Structures **139-140**, 174 (2018).

[95] The Mathworks Inc., *MATLAB - MathWorks,* (2017).

[96] T. W. Simpson, J. D. Peplinski, P. N. Koch, and J. K. Allen, *Metamodels for Computer-based Engineering Design : Survey and recommendations,* , 129 (2001).

[97] I. M. Sohoi, *KIRIYA, V. S. The motion of bodies in,* , 1332 (1976).

[98] M. S. Section and O. Ridge, *Exploratory designs for computational experiments,* **43** (2008).

[99] E. Riks, *AN INCREMENTAL APPROACH TO THE SOLUTION OF SNAPPING AND BUCKLING PROBLEMSt,* International Journal of Solids and Structures **15**, 529 (1979).

[100] Vasios Nikolaos, *Nonlinear Analysis of Structures - The arc-length method,* (2015), 10.7763/IJET.2015.V7.786.

[101] C. Bisagni, *Numerical analysis and experimental correlation of composite shell buckling and post-buckling,* **31** (2000).

[102] S. Marelli and B. Sudret, *UQLab: A Framework for Uncertainty Quantification in Matlab,* in *Vulnerability, Uncertainty, and Risk* (2014).

[103] M. Stein, *Large Sample Properties of Simulations Using Latin Hypercube Sampling,* Technometrics (1987), 10.2307/1269769.

[104] M. McKay, *Latin hypercube sampling as a tool in uncertainity analysis of computer models,* Proceedings of the 1992 Winter Simulation Conference (1992), 10.1145/167293.167637.

[105] B. Subjected and T. O. Torsion, *Beams subjected to bending and torsion,* , 1.

[106] W. Young and R. G. Budynas, *Roark's Formulas for Stress and Strain* (2002) pp. 553–688.

[107] F. N. Fritsch and R. E. Carlson, *Monotone Piecewise Cubic Interpolation,* SIAM Journal on Numerical Analysis (1980), 10.1137/0717021.

[108] C. W. Clenshaw and A. R. Curtis, *A method for numerical integration on an automatic computer,* Numerische Mathematik (1960), 10.1007/BF01386223.

[109] F. Campolongo, I. Azzini, S. Tarantola, M. Ratto, P. Annoni, and A. Saltelli, *Variance based sensitivity analysis of model output. Design and estimator for the total sensitivity index,* Computer Physics Communications **181**, 259 (2009).

[110] A. Saltelli, M. Ratto, T. Andres, F. Campolongo, J. Cariboni, D. Gatelli, M. Saisana, and S. Tarantola, *Global Sensitivity Analysis. The Primer* (2008) arXiv:arXiv:1011.1669v3 .

[111] J. Herman and W. Usher, *SALib: An open-source Python library for Sensitivity Analysis,* The Journal of Open Source Software (2017), 10.21105/joss.00097.

[112] J. M. Wernik and S. A. Meguid, *Atomistic-based continuum modeling of the nonlinear behavior of carbon nanotubes,* Acta Mechanica (2010), 10.1007/s00707-009-0246-4.

[113] G. W. Corder and D. I. Foreman, *Nonparametric Statistics for Non-Statisticians: A Step-by-Step Approach* (2011) arXiv:arXiv:1011.1669v3 .

[114] F. Pedregosa, A. Gramfort, V. Michel, B. Thirion, O. Grisel, M. Blondel, P. Prettenhofer, V. Dubourg, F. Pedregosa, A. Gramfort, V. Michel, B. Thirion, F. Pedregosa, and R. Weiss, *Scikit-learn : Machine Learning in Python To cite this version : Scikit-learn : Machine Learning in Python,* Journal of Machine Learning Research (2011), https://dl.acm.org/citation.cfm?id=2078195.

[115] A. G. De, G. Matthews, T. Nickson, K. Fujii, A. Boukouvalas, P. León-Villagrá, Z. Ghahramani, and J. Hensman, *GPflow: A Gaussian Process Library using TensorFlow Mark van der Wilk,* Journal of Machine Learning Research **18**, 1 (2017).

[116] Chollet François, *Keras: The Python Deep Learning library,* (2015).

[117] C. Zhu, R. H. Byrd, P. Lu, and J. Nocedal, *Algorithm 778: L-BFGS-B: Fortran subroutines for large-scale bound-constrained optimization,* ACM Transactions on Mathematical Software (1997), 10.1145/279232.279236.

[118] J. Hensman, A. Matthews, and Z. Ghahramani, *Scalable Variational Gaussian Process Classification,* **38** (2014), 10.1007/s10835-013-9196-4, arXiv:1411.2005 .

[119] H. Nickisch and C. E. Rasmussen, *Approximations for Binary Gaussian Process Classification,* Machine Learning Research (2008), http://dx.doi.org.ez.statsbiblioteket.dk:2048/10.1111/add.12082.

A

ESTIMATION OF UNCERTAINTY FOR THE QUANTITIES OF INTEREST

The generation of designs accounting for geometric imperfections allows to study the influence of these imperfections on the quantities of interest. The quantities of interest in this work are the critical buckling load $P_{critical}$ and the energy absorption $E_{absorbed}$ of the metamaterial. To perform this analysis 1024 simulations of a single design i.e. single DoE point, were conducted, each having a different amplitude value for the first buckling mode used to create the geometric imperfection of that design.

The procedure used to calculate $E_{absorbed}$ was simplified for the force-displacement curves:

(a) Generate a vector of 10000 evenly spaced values between 0.0 and the maximum design height;

(b) Generate an interpolator object based on the output vectors of force and displacement for a given curve from the response database;

(c) Use the interpolator object on the newly generated vector from point a) to obtain a vector of force values of same length;

(d) Apply Simpsons rule to calculate the area under the newly generated force curve;

(e) Append area for every design to a single list for all designs.

The distributions of quantities of interest were firstly visualized in the form of histogram for comparison between both $P_{critical}$ and $E_{absorbed}$ distributions. After obtaining both QoIs, a subsequent distribution fitting procedure was performed. An automated procedure fits every of the available distributions to the data and the goodness of fit is measured via two metrics, namely chi^2-test and the KS-test [113]. Before any distribution was fitted, the data was standardized, that is the mean of QoI population is subtracted from data points and the result is divided by the standard deviation of the population.

For the chi^2-test the standardized data is firstly binned into 50 bins (approximately 20 samples per bin). The observed amount of values in every bin is compared to the theoretical value for every checked distribution. The chi^2 metric may be expressed as relative square error per bin:

$$\chi^2 = \sum \frac{(\text{observed} - \text{theretical})^2}{\text{theoretical}} \tag{A.1}$$

where lower values obtained from the test represent a better fit.

The KS-test quantifies the distance between the observed cumulative distribution function and the theoretical distribution function to be fitted. As a result of the test a p-value is generated. A 0.05 significance level has been adopted, that is for p-values greater than 0.05 we assume that the theoretical fitted distribution function is not significantly different from the observed distribution function, i.e. the fitted distribution characterizes the observed data well enough. The top three distributions and the normal distribution were reported.

Table A.1: Mode-1 imperfections experimentally measured on prototypes.

	Imperfection
	1.47°
	1.79°
	1.47°
	0.75°
	3.25°
	3.56°
	2.21°
	1.24°
	1.97°
	0.92°
	3.67°
	2.16°
	2.43°
	0.65°
Mean	1.97°
Median	1.88°

The measurements of mode-1 imperfections of manufactured prototypes are presented in Table A.1. These values were used to assume a statistical distribution for the manufacturing imperfections. As the median value of the population is smaller than the mean, the assumed distribution shall be negatively skewed. Thus, the lognormal distribution was selected to seed the imperfections for RIKS analysis. As discussed 1024 imperfections from the lognormal distribution were seeded for a single design to estimate the uncertainty.

Figure A.1 represents the true probability density functions for the obtained values of critical buckling load and energy absorbed. Contrary to the seeded imperfections, the statistical distributions of the quantities of interest had a positive skew. The distribution of energy absorbed had regions of lowered probability, however the range of likelihood for these regions was narrow, therefore it was possible to assume that both quantities of interest have the same distribution. The loggamma distribution was determined by chi-squared and KS-tests as the best fit to the true probability density functions of the quantities of interest.

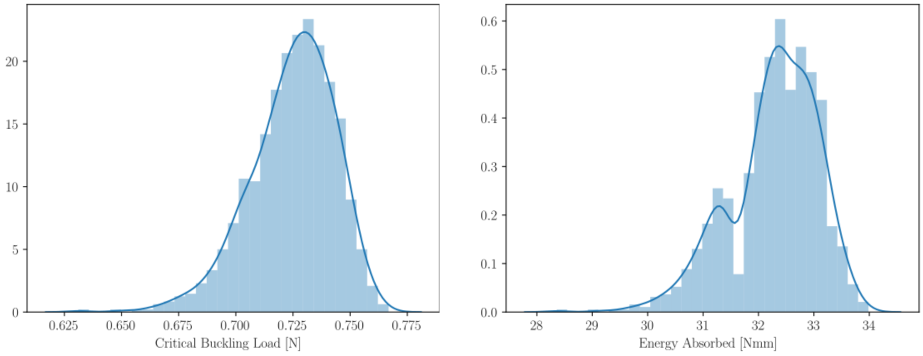

(a) $P_{critical}$ (b) $E_{absorbed}$

Figure A.1: True probability density functions for the qunatities of interest

Estimation of uncertainty for the quantities of interest may be achieved by predicting the response of a unit cell design for the various sampled imperfections. The number of sampling points required to estimate the uncertainty for each design was determined by variation of the mean and standard deviation of quantities of interest of the initial design of the unit cell. The mean and standard deviation computed in Figure A.2 were obtained for an increasing number of sampling points. Either metric converges to a constant value for enough sampling points. Observing Table A.2 and Figure A.2 estimating standard deviation requires more sampling points than estimating the mean of the distribution. To reach estimation error for standard deviation below 5%, 200 sampling points per DoE would be required Yet in the Gaussian Process framework the presence of other design points around each point locally improves the predictions of uncertainty at every point of the design space. Therefore 60 imperfections per design would provide a reasonable estimation of uncertainty. However, it was observed that the standard deviation was low relative to the mean.

With a tight distribution for the quantities of interest, it is probable that the modelling error for machine learning regression will be higher then the uncertainty for both $P_{critical}$ and $E_{absorbed}$. As the mean estimation error for 5 imperfections was low, it was decided

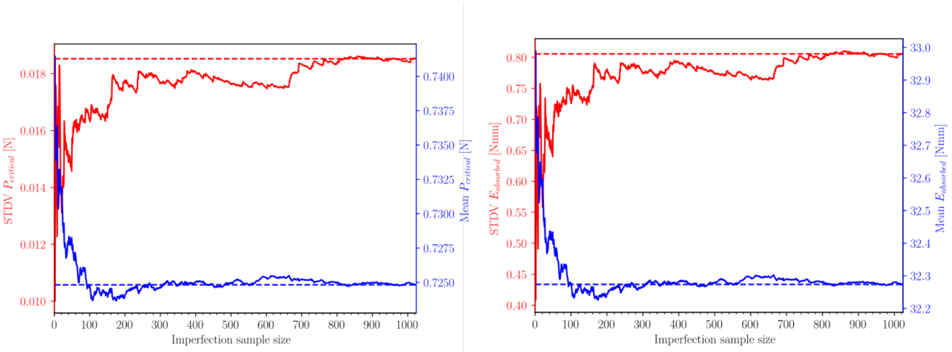

(a) $P_{critical}$ (b) $E_{absorbed}$

Figure A.2: Convergence of mean and standard deviation of the qunatities interest for loggamma distribution

to seed one imperfection per DoE point to obtain representative results.

Quantile-quantile (qq) and percentile-percentile (pp) plots for the Loggamma and Gaussian distributions were generated. Both plots are extensively used in statistical analysis with the difference being the percentile-percentile plots have higher resolution in the center of the distribution, closer to the median whereas the quantile-quantile plot are more accurate for the tails of a distribution. In both cases perfectly fitted data lies on the diagonal of the plot (red dashed line) in Figure A.3 and Figure A.4.

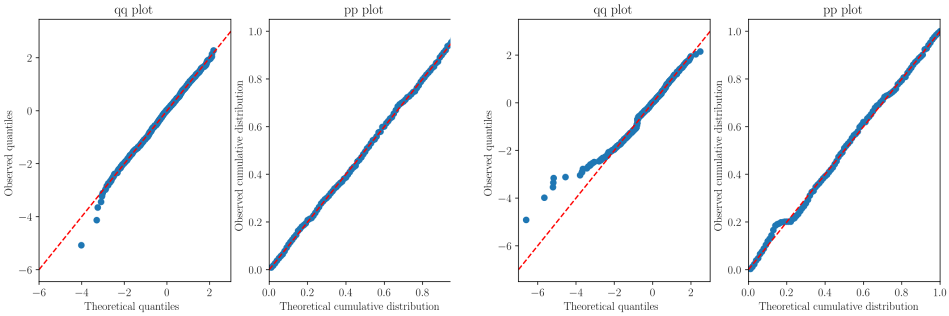

(a) $P_{critical}$ (b) $E_{absorbed}$

Figure A.3: Loggamma distribution qq and pp plots for critical buckling and energy absorption.

The loggamma distribution captures the center shape of the distributions well as indicated by the pp plots. The gaussian distribution is not an unreasonable fit, however it is evident from the pp-plot that the mean and median of the distribution do not coincide. Focusing on the qq-plots, greater deviations at the tails of the distributions are evident.

Table A.2: Relative error of the estimation of mean and standard deviation for the loggamma distribution.

Sampling Points	Mean Critical Buckling change	STDV Critical Buckling change	Mean Energy change	STDV Energy change
1024	0.00%	0.00%	0.00%	0.00%
500	0.01%	4.32%	0.01%	3.61%
200	0.12%	4.32%	0.11%	3.64%
100	0.00%	10.27%	0.01%	7.66%
80	0.14%	11.35%	0.15%	9.62%
60	0.28%	12.43%	0.29%	10.69%
40	0.32%	18.38%	0.35%	17.13%
20	1.06%	10.27%	1.06%	13.03%
15	0.76%	14.59%	0.77%	10.34%
10	1.37%	27.57%	1.38%	33.07%
5	1.61%	39.46%	1.58%	44.02%

While gaussian distribution can capture the mean of the distribution relatively well, the qq plot clearly indicates that the true distribution has a negative skew.The loggamma distribution models the right tail of the distribution well, but for maximum buckling values it assigns lighter left tail than the empirical distribution. On the contrary for the energy values, the loggamma distribution assigns heavier left tail than the empirical distribution. This contrast may be result of the discussed dip in the probability density function of the energy absorbed values shown in Figure A.1. As the normal distribution can capture the mean of the distributions of quantities of interest, it had been assumed for the machine learning models in this work.

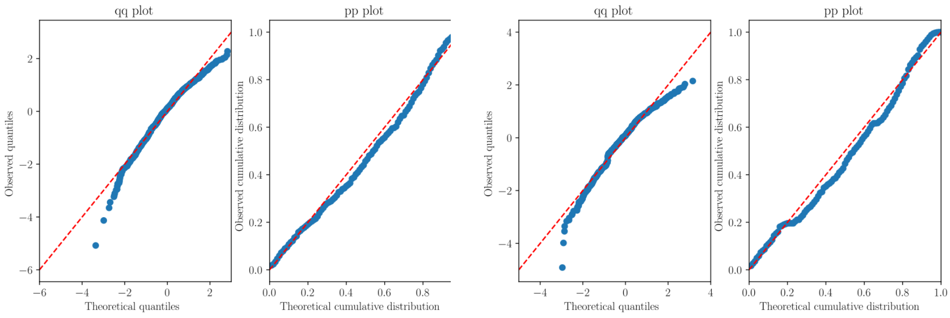

(a) $P_{critical}$ (b) $E_{absorbed}$

Figure A.4: Normal distribution qq and pp plots for critical buckling and energy absorption.

B

COMPARATIVE INVESTIGATION OF SPARSE GAUSSIAN PROCESSES

Bayesian machine learning is currently a very active research field because it allows learning a process and explaining the confidence of the prediction. In Chapter 2 we discussed the importance of Sparse Gaussian Processes in this field. Here, we assess the performance of different Sparse Gaussian Process methods within the context of our metamaterial analysis problem. Therefore, a dataset is created from static buckling analyses of the first 100,000 DoE points of the Sobol sequence and multiple state-of-the-art machine learning algorithms are used to classify and regress this dataset.

B.1. REGRESSION

The purpose of this dataset was to characterize the performance of Sparse GP approximations in comparison to conventional Gaussian Processes and a Neural Network regressor. Characterization has been performed for the critical buckling load $P_{critical}$.

As discussed in Section 2.4.1, an important issue when using Gaussian Processes is the computational expense incurred for large datasets. The number of training points that can be used herein already falls outside of the applicability of a full Gaussian Process. A careful investigation of the performance of different Gaussian Process formulations with emphasis on the Variational Free Energy approximation [88] is presented next. For all the Machine Learning activities in-house scripts were created that utilized different GP algorithms sourced from suitable Python Libraries. The libraries utilized throughout this study are the Scikit-learn [114], a general purpose machine learning toolbox, and GPflow [115], a recent project implementing novel Gaussian Process algorithms in the context of Google's Tensorflow environment for GPU computing and easy CPU parallelization. Additionally, Neural Networks models are created using the Keras library [116], similar to the model used previously in [76]. The models selected for regression are:

1. Conventional GP using Scikit-Learn implementation – Scikit;
2. Conventional GP using GPflow implementation – GPf Full;
3. Sparse FITC approximation using GPflow implementation – FITC;
4. Sparse VFE approximation using GPflow implementation – SGPR;
5. Modified VFE by Hensman et al. [115] using GPflow – SVGP;
6. Neural network using Keras – NN.

All GP models used a Matern 5-2 kernel as the covariance function to avoid excessive smoothening of the approximated function. The Matern class can be viewed as a generalization of the squared exponential kernel[1] parametrized by an extra parameter ν. A special case within the Matern class of kernels occurs when $\nu \rightarrow \inf$, since it leads to the mentioned squared exponential kernel with an infinitely differentiable approximated function [80]. Smaller ν implies less smooth approximation functions, as seen in Figure B.1. For $\nu = 2.5$, i.e. the Matern 5-2 kernel, the function becomes twice differentiable. This is relevant for optimization algorithms utilizing the Hessian.

$$\text{Matern 5-2 kernel} = \sigma_f^2 \left(1 + \frac{\sqrt{5}\left|x - x'\right|}{l} + \frac{5\left|x - x'\right|}{3l^2}\right) + \exp\left(\frac{\sqrt{5}\left|x - x'\right|}{l}\right) \tag{B.1}$$

To facilitate the learning process the considered Matern52 kernel included the Automatic Relevance Determination (ARD) [63, 80], so that each input had a separate length scale parameter l. ARD also provides a simplified analysis of the sensitivity of the quantities of interest, i.e. it estimates which inputs are critical for the learning process.

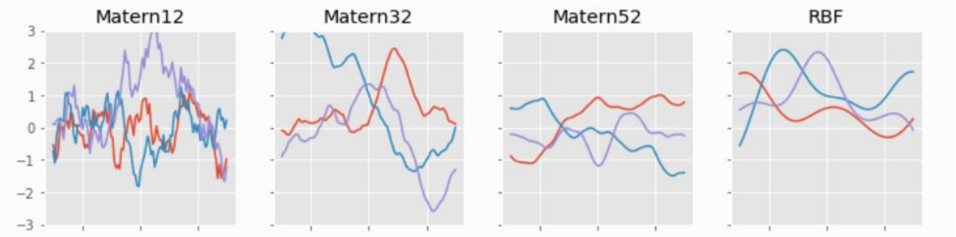

Figure B.1: Example prior functions for different smoothness of the Matern kernel.

The considered neural networks model consisted of 10 sequential layers of neurons, with 400 per layer. Relu activation function was used for each of the layers. Adam optimizer with step of 0.0001 was utilized for 1000 epochs.

The supervised-learning process starts by splitting the data into training and test sets that are subsequently standardized. The parameters supporting the model comparison are:

---

[1] Also called radial basis function (RBF) kernel.

- Set size – due to memory restrictions of the computer only subsets of the simulated sequence were checked (especially for full GPs);
- Training set size;
- Ratio of test set size to the full set size;
- Time – as the model becomes more complex, the time for training the model increases;
- Ratio of inducing points to training points – only relevant for sparse approximations.

The predictor's quality for different model parameters is determined by the mean squared error MSE and the $\mathscr{R}^2$. Both metrics are strongly correlated. $\mathscr{R}^2$ is the ratio of total variance explained by the model to the total variance [113]. For $\mathscr{R}^2 = 1.0$ the inputs and outputs are perfectly correlated.

$$\mathscr{R}^2 = 1 - \frac{\sum_{i=1}^{k}(Y_i - Y_i^p)^2}{\sum_{i=1}^{k}(Y_i - Y_i^m)^2} \quad \text{where } Y_i^m = E[Y_i] \tag{B.2}$$

The inducing points needed in the sparse approximations are selected as a subset of the first m points of the DoE.

Remark 2 *We noticed a significant improvement of accuracy of the sparse methods when initializing the location of the inducing points to coincide with the Sobol sequence used for the DoE. We suspect that the internal space-filling structure defined by the Sobol sequence is advantageous to the optimization process of finding the best location of the inducing points.*

The optimal hyperparameters of the model l_i and σ_f^2 are found by minimizing the negative log likelihood function. Throughout this work the optimization of hyperparameters is done using the Limited Broyden-Fletcher-Goldfarb-Shanno algorithm for Bound constraints (L-BFGS-B) [117] that was allowed to run for 1000 iterations or until convergence.

Figure B.2 summarizes all the regression models used in this comparative study. Note the scale of the vertical axis. Each marker represents a different machine learning model used with the number next to the marker representing the time required to train the model. The color of the marker illustrates the ratio of inducing points to the number of training points used in a sparse approximation, i.e. markers tending to the red color indicate that more inducing points were used when comparing to the total number of available training points while markers tending to the blue color mean fewer inducing points (less computational time required to train). Note that non-sparse models (GPf Full, NN, Scikit) do not use inducing points, so we represent them with open (unfilled) markers to distinguish them from the sparse methods. The marker's size represents the proportion of dataset points assigned as test points. The dashed line illustrates the average $\mathscr{R}^2$ value for all the executed training runs. A logarithmic trend line is seen in gray, for the quality of the fit expressed by R-squared of 0.6:

$$\mathscr{R}^2 = 0.007343 * \ln(\text{Full Dataset Size}) + 0.911 \tag{B.3}$$

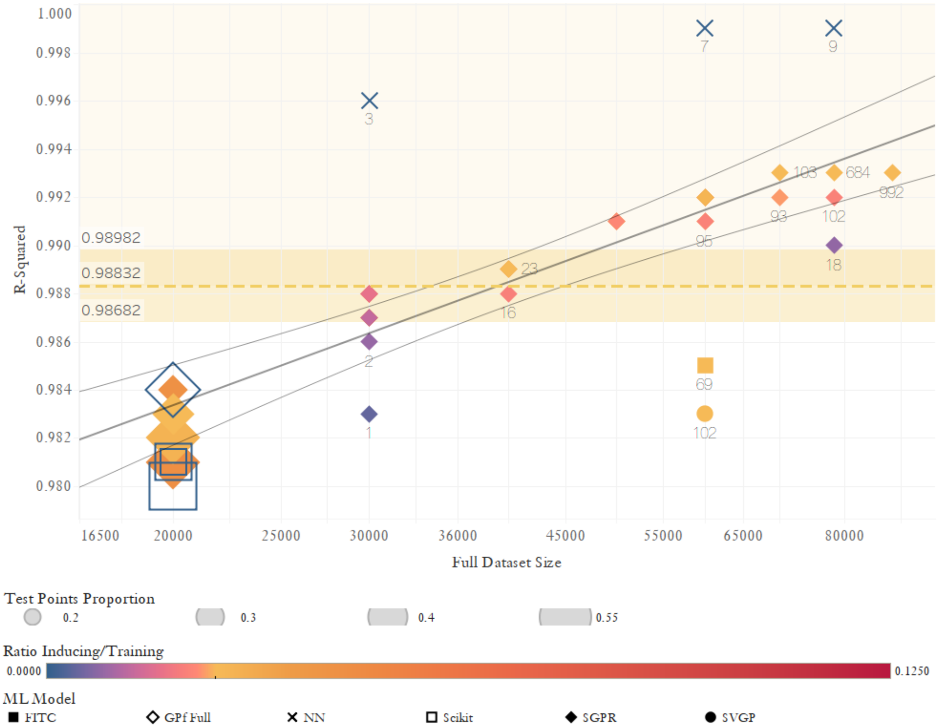

Figure B.2: $\mathscr{R}^2$ as a function of dataset size. The dashed yellow line represents the average $\mathscr{R}^2$ with 95% confidence intervals for all runs, the gray line for the logarithmic trendline, and the labels indicate the time (min) to train the model.

The general observation is that the performance of the regressor logarithmically increases as the dataset size increases. Thus, an increase in dataset size increases the performance of a given regressor until saturation is reached, at the expense of time required to train the model. For a given dataset size the $\mathscr{R}^2$ becomes higher as one increases the proportion of training points. This behavior is intuitive: as more data is available for training, thus improving the quality of the fit, there is lower probability of encountering a point in the test set that will not be described by the prediction rule.

The smallest dataset size seen in the figure has 20000 points. For this dataset the performance of conventional (full) GPs can be compared with SGPR. One may observe that the GPflow implementation of a full GP led to more accurate predictions than the ones obtained by the Scikit implementation regardless of the test set ratio. This can be explained by the fact that GPflow implementation used herein included the ARD method to assign a separate length scale hyperparameter for each input dimension, which facilitates learning. It is also worth noting, that for the same dataset size and kernel, the sparse algorithms can only match but not exceed the performance of conventional GP with full covariance inversion.

Considering the dataset of 30000 points, the influence of the number of inducing points can be analyzed. A model with 200 inducing points performs better than any of the models with 20000 training points, at a fraction of the time. As the ratio of inducing/training points increases, the performance of the regressor improves. The Neural Network algorithm achieved higher $\mathscr{R}^2$ than any GP implementation. A possible explation is the choice of kernel. The Matern 5-2 kernel generates relatively smooth functions whereas the Neural Network is characterized by an inherently noisy approximation provided by all the combinations of signals processed by the neurons. That is also why neural network models can lead to overfitting and tend to be fine interpolators yet are often poor in data extrapolation. Another drawback to using standard neural networks is that contrary to GPs they do not have an in-built uncertainty estimation mechanism.

Differing sparse algorithms are again compared for the subset of 60000 points. The SVGP approximation has inferior performance when compared to SGPR for the same parameters, due to the difference in the Evidence Lower Bound (ELBO) estimation. As discussed in Section 2.4.1, in Variational Free Energy approximation the inducing points in $q(\mathbf{f}_m|\mathbf{y})$ are treated as variational parameters. To obtain tight variational lower bound, the dependency of variational free energy on $q(\mathbf{f}_m|\mathbf{y})$ must be removed. As this term is factorized out more efficiently in the SGPR model, the ELBO is narrower than in the case of the more general SVGP model, resulting in higher $\mathscr{R}^2$ for this dataset.

The FITC approximation is a better predictor than SVGP, though not as accurate as the SGPR model. Whereas the SGPR approximation overestimates the noise variance, the FITC model severely underestimates the noise variance, sacrificing the accuracy of the predicted mean.

The worst model in the plot has $\mathscr{R}^2 = 0.98$ whereas the best sparse GP approximation overall has an $\mathscr{R}^2 = 0.993$. Converting the fraction of variance explained to percent of standard deviation explained, the values were respectively 86% and 92%. This means that for the best GP model considered the standard deviation of errors is 92% less than the standard deviation of a dependent variable, whereas for the worst model it is 86% less. In other words, the standard deviation of the best model errors is about 1/12 the size of the standard deviation of the errors that you would get with a constant-only model. Intuitively, this is a good result. Comparing this result with the worst model obtained accounts to 75% relative difference between the models. In other words, the confidence intervals generated from the best model are approximately 75% narrower than the confidence intervals produced by the worst model. To the best of the author's judgment this performance gain is substantial and worth the additional model complexity.

B.2. CLASSIFICATION

The performance of Gaussian Process Classifiers with different likelihood approximations is compared to determine the classification algorithm for the final model. Classification is important to determine the regions of the design space where the structure is coilable. The result of this binary classification may be used to visualize regions of the design space where the metamaterial coils and to conduct the nonlinear post buckling simulations only for DoE points that coil. This avoids wasting computational resources. The criterion for coilability of a given design is based on two conditions:

- The rotational displacement around the Z axis of the design is greater than 1.0E-4
- The displacement in the XY plane is not greater than 1.0E-4

The amplitude of the first buckling mode directly corresponds to the rotational displacement around the Z-axis of the design. The second criterion is required to eliminate designs that coil and bend at the same time i.e. where higher buckling eigenmodes are triggered along with the first bifurcation point. As in the case of the regression study, the data was split between training and test sets and subsequently standardized. The focal issue in Gaussian Process Classification is the need to approximate the posterior over function values $p(\mathbf{f}, \mathbf{y})$. This need arises as the likelihood function in the case of classification is non-Gaussian, thus the exact posterior is a non-Gaussian distribution as well. For conventional GPs the two most prominent approximations are the Laplace approximation and the Expectation Propagation (EP) approximation. The Laplace approximation is used despite its inferior accuracy as it is generally faster. For this approximation the mean of the true and approximate posterior coincides. The EP approximation tends to perform better as it assigns probability density to areas where this exists, at the expense of areas where there is none. However, there is a third approximation based on the discussed KL-divergence that avoids assigning density to areas where there is none, at the expense of areas where there is some. This is convenient as the KL-approximation lends itself to sparse Gaussian processes. For a detailed discussion of the different GP posterior approximations for GP classification the reader is referred to [80, 118, 119].

The goal of this investigation is to compare conventional GP classifiers that use either the Laplace or the EP approximation with a Sparse GP classifier that utilizes the KL-divergence. As a benchmark, the Support Vector Machine Classifier (SVC) [63] is included as well. The GP approximations were implemented with the Matern 5-2 kernel of the GPflow [115] library, whereas the SVC classifier was implemented using the Scikit-learn [114] library with squared exponential kernel and a default penalty value of 1.0.

Similarly to the regression study, all GP models utilized the Matern52 kernel with ARD. The parameters of the classification model under investigation are:

- Set size – due to memory restrictions of the computer, only subsets of the simulated sequence are investigated;
- Training set size;

- Ratio of test set size to the full set size;
- Time – as the model becomes more complex, the time for training the model increases;
- Ratio of inducing points to training points – only relevant for sparse approximations.

Each sparse GP classifier used the Bernoulli likelihood function to perform inference. The same hyperparameter optimization method was used as in the regression investigation: L-BFGS-B [117].

The quality of each classifier is judged based on the accuracy, precision and recall for the test set. All these metrics are derived from the so-called confusion matrix [69]. A schematic confusion matrix is presented in Table B.1.

Table B.1: Schematic representation of the confusion matrix for binary classification.

		Predicted Class	
		Non-Coilable	Coilable
Actual Class	Non-Coilable	True Negative	False Positive
	Coilable	False Negative	True Positive

The accuracy of the classifier is defined as the ratio of truly predicted points to all the predicted points, i.e. it tells how often the model is correct. Precision is the ratio of True Positives to all Positives, i.e. it is especially helpful if Type I error (False Positive) is highly penalized. Conversely, Recall is the ratio of True Positives to all the points that are coilable and penalizes the Type 2 error. As in the case of coilability classification both errors are equally penalized therefore a fourth metric, the F1-score has been calculated, with F1 defined as:

$$F1 = 2 \times \frac{\text{precision} \times \text{recall}}{\text{precision} + \text{recall}} \tag{B.4}$$

Performance of different classifiers was compared and summarized in Figure B.3. The meaning of the legend is consistent with the regression plot. Again, the reader is advised to be mindful of the scale of the vertical axis.

The average F1 score for all runs was 0.977. A high value of F1 score implies that recall and precision metrics are also relatively high, therefore type I and type II errors are balanced in the dataset. In terms of predictor performance, the lowest F1 score is approximately 0.935, this means that the classifier will correctly predict the class in over 9 out of 10 points. For comparison, if 60% of the designs are coilable in the dataset, then by randomly picking points from the design space one will achieve about 60% accuracy. The machine learning models perform significantly better than random point sampling. Comparing the best SVGP model from a subset of 20000 points with the overall best, respectively 1.5% and 1% of points are misclassified. For classification of a set of a million DoE points the difference is 5000 misclassified points. In this case the penalty

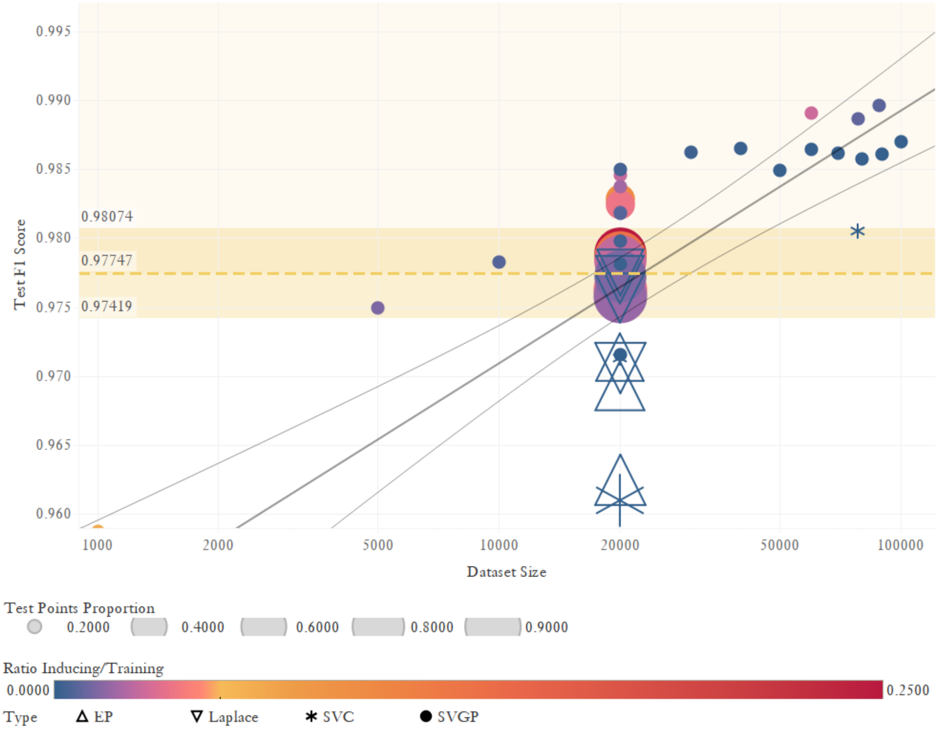

Figure B.3: F1 score as function of dataset size. The yellow line represents the average F1 score with 95% confidence intervals for all runs, and the gray line for the logarithmic trendline.

for misclassification is relatively low compared to the additional computational time required to generate additional simulations. A dataset of 20000 points provides a balance between performance and the computational expenditure to generate a classifier with suitable performance.

Several models were trained for a dataset size of 20000 points. The first observation is that the GP models achieved higher quality prediction rules than the benchmark SVC classifier. The EP approximation to the posterior results in lower accuracy than the Laplace approximation for the same model parameters. This result was not expected and indicates that the mean is a strong statistic for this dataset as in the Laplace approximation the mean of the true posterior and approximate posterior coincide. For the same dataset size, the Laplace approximation performed on the same level as the sparse approximation – SVGP. Interestingly, increasing the number of inducing points has a minor effect on the quality of the classification, and in some cases leads to lower performance.

Overall, the findings of this study are consistent with the regression study, sparse GP approximations enable to use more points of the dataset to perform inference, leading to a better prediction rule, as compared to conventional GPs with full covariance matrix inversion.

C

SUPPLEMENTARY CONTOUR PLOTS FOR MACHINE LEARNING

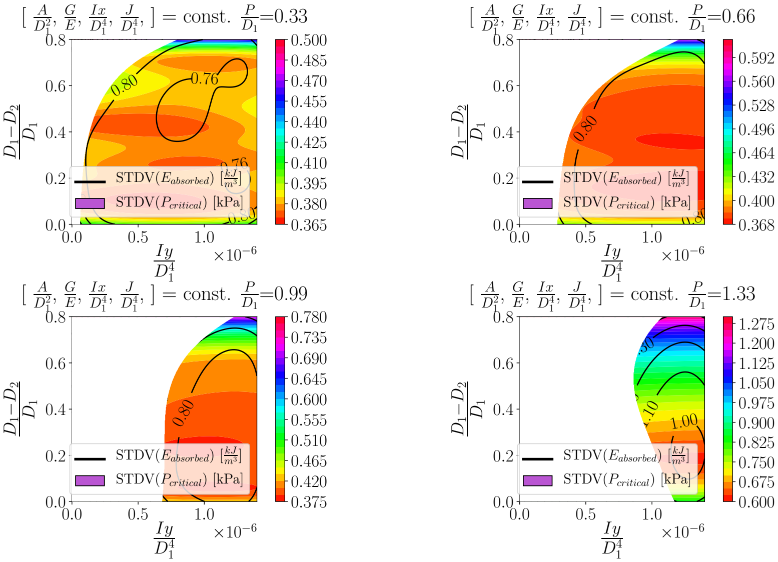

Figure C.1: Standard deviation of quantities of interest as function of I_y , D_R and P. The normalized parameters A=0.001, G/E=0.36, $I_x = 7.5 \times 10^{-7}$, and $J_\tau = 2.5 \times 10^{-6}$ remain constant.

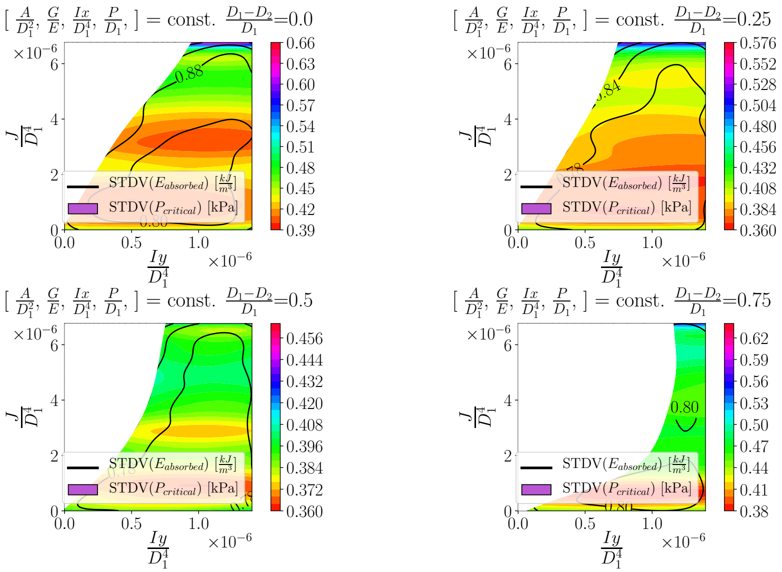

Figure C.2: Standard deviation of the quantities of interest as function of I_y, J_τ, and D_R. The normalized parameters A=0.001, G/E=0.36, $I_x = 7.5\times10^{-7}$, and P=0.66 remain constant.

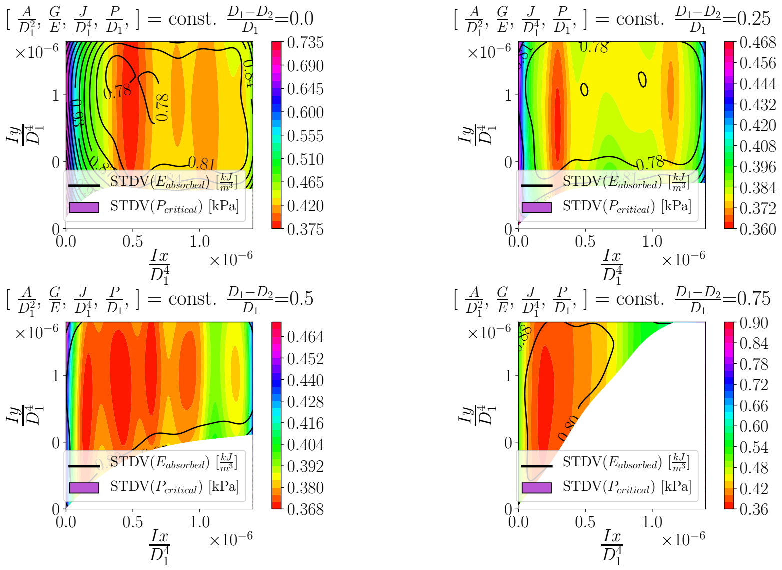

Figure C.3: Standard deviation of the quantities of interest as function of I_x, I_y and D_R. The normalized parameters A=0.001, G/E=0.36,$J_\tau = 2.5\times10^{-6}$ and P=0.66 remain constant.

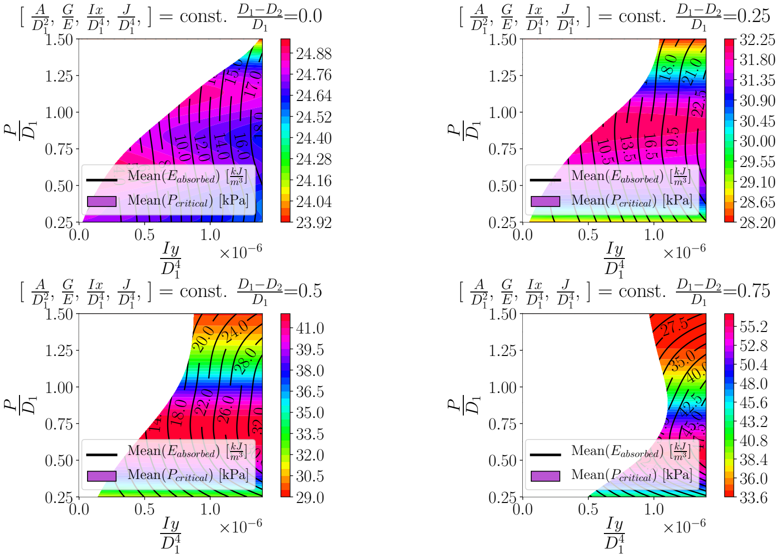

Figure C.4: Mean quantities of interest as function of I_y, P and D_R. The normalized parameters A=0.001, G/E=0.36, $I_x = 7.5 \times 10^{-7}$ and $J_\tau = 2.5 \times 10^{-6}$ remain constant.

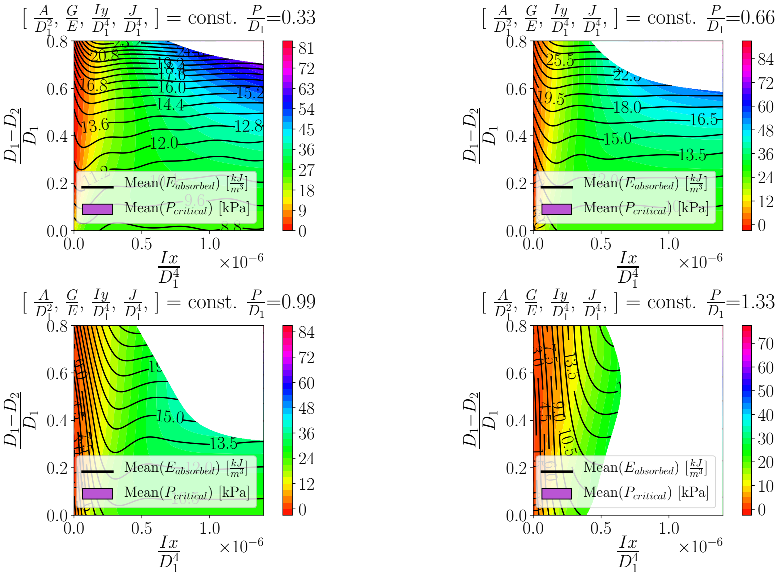

Figure C.5: Mean quantities of interest as function of I_x, D_R and P. The normalized parameters A=0.001, G/E=0.36, $I_y = 7.5 \times 10^{-7}$, and $J_\tau = 2.5 \times 10^{-6}$ remain constant.

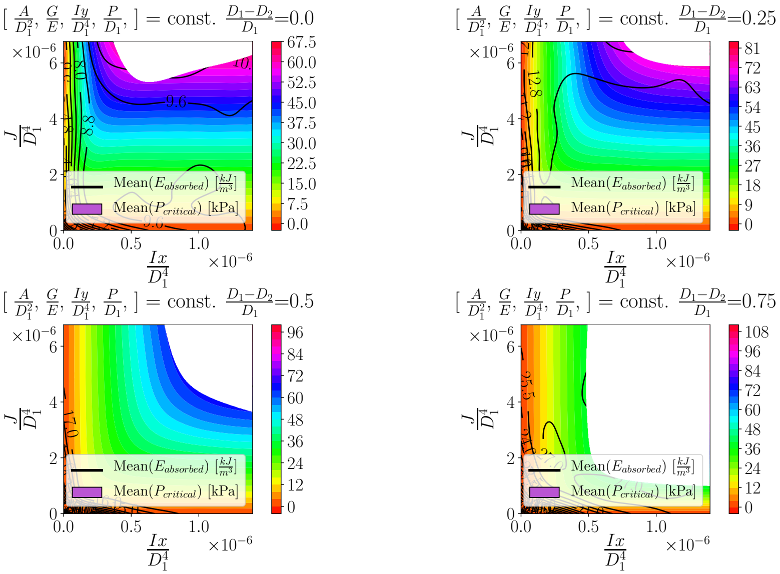

Figure C.6: Mean quantities of interest as function of I_x, J_τ and D_R.The normalized parameters A=0.001, G/E=0.36, $I_y = 7.5 \times 10^{-7}$, and P=0.66 remain constant.